ABSTRACT

Title of Document: SLOT FILM COOLING: A COMPREHENSIVE EXPERIMENTAL CHARACTERIZATION

Fernando Raffan, Doctor of Philosophy, 2016

Directed By: Dr. André Marshall, Department of Aerospace Engineering / Department of Fire Protection Engineering

When components of a propulsion system are exposed to elevated flow temperatures there is a risk for catastrophic failure if the components are not properly protected from the thermal loads. Among several strategies, slot film cooling is one of the most commonly used, yet poorly understood active cooling techniques. Tangential injection of a relatively cool fluid layer protects the surface(s) in question, but the turbulent mixing between the hot mainstream and cooler film along with the presence of the wall presents an inherently complex problem where kinematics, thermal transport and multimodal heat transfer are coupled. Furthermore, new propulsion designs rely heavily on CFD analysis to verify their viability. These CFD models require validation of their results, and the current literature does not provide a comprehensive data set for film cooling that meets all the demands for proper validation, namely a comprehensive (kinematic, thermal and boundary condition data) data set obtained over a wide range of conditions. This body of work aims at

solving the fundamental issue of validation by providing high quality comprehensive film cooling data (kinematics, thermal mixing, heat transfer). 3 distinct velocity ratios ($VR=u_c/u_\infty$) are examined corresponding to wall-wake (VR~0.5), min-shear (VR ~ 1.0), and wall-jet (VR~2.0) type flows at injection, while the temperature ratio $TR= T_\infty/T_c$ is approximately 1.5 for all cases. Turbulence intensities at injection are 2-4% for the mainstream ($u_{rms}/u_{\infty,}$ $v_{rms}/u_{\infty,}$), and on the order of 8-10% for the coolant ($u_{rms}/u_{c,}$ $v_{rms}/u_{c,}$).

A special emphasis is placed on inlet characterization, since inlet data in the literature is often incomplete or is of relatively low quality for CFD development. The data reveals that min-shear injection provides the best performance, followed by the wall-jet. The wall-wake case is comparably poor in performance. The comprehensive data suggests that this relative performance is due to the mixing strength of each case, as well as the location of regions of strong mixing with respect to the wall. Kinematic and thermal data show that strong mixing occurs in the wall-jet away from the wall ($y/s>1$), while strong mixing in the wall-wake occurs much closer to the wall ($y/s<1$). Min-shear cases exhibit noticeably weaker mixing confined to about $y/s=1$. Additionally to these general observations, the experimental data obtained in this work is analyzed to reveal scaling laws for the inlets, near-wall scaling, detecting and characterizing coherent structures in the flow as well as to provide data reduction strategies for comparison to CFD models (RANS and LES).

SLOT FILM COOLING: A COMPREHENSIVE EXPERIMENTAL CHARACTERIZATION

By

Fernando Raffan

Dissertation submitted to the Faculty of the Graduate School of the
University of Maryland, College Park, in partial fulfillment
of the requirements for the degree of
Doctor of Philosophy
2016

Advisory Committee:

Professor André Marshall	Chair
Professor Christopher Cadou	Co-advisor
Professor Kenneth Yu	
Professor James Baeder	
Professor Marino DiMarzo	(Dean's Representative)

Dedication

This work is the fruit of many sleepless nights, accompanied by sweat and tears of both joy and frustration. I would like to dedicate it to those close to my heart who were with me along the journey. To God, for putting me on this path and giving me the strength and courage to persevere; to my parents and siblings, for their love and support throughout all these years (this time apart has not been in vain). To my now departed grandmother Tita, for always being very proud of my accomplishments, I know you now watch over me from above. Finally, I want to dedicate this work to my wife, whom I met as I started my doctoral research and who has been at my side through highs and lows ever since: I love you.

Acknowledgments

This work was supported by NASA through its Constellation University Institutes Project (CUIP). Special thanks to Claudia Meyer as well as the various points of contact (Kevin Tucker, Doug Westra, Joe Ruff) for their support and invaluable feedback.

I would also like to acknowledge the unwavering support of my friends and colleagues throughout the years. This work would have been much more difficult without the initial guidance of Dr. Carlos Cruz who was not only a colleague during the beginning of my journey, but became a dear friend. Also to Dr. Andrew Voegele who shared the struggles and successes of our many hours in the laboratory. I would also like to thank my friends: Dr. John Alexis Guerra and his wife Mafe, Dr. Camilo Aguilera and Dr. Daniel Waters for their friendship over the years which made the experience of this doctorate much more enjoyable. Special thanks to Dr. Stas Stoliarov for financial support and mentoring during these last few years.

Finally, my eternal gratitude to my advisers Dr. Andre Marshall and Dr. Chris Cadou who are not only great professionals, but great human beings as well (a combination that is not as common as one would like to think). Their patience and guidance over the years has been more than one could ask for and certainly more than I deserve.

Table of Contents

List of Tables

List of Figures

Nomenclature

D	test section hydraulic diameter
d_{diff}	diffraction limited particle diameter
d_i	particle image size
d_p	physical particle diameter
d_w	thermocouple wire diameter
$f_{\#}$	f-stop of optical system
F_{ij}	radiation view factor between surface i and surface j
h_{tc}	turbulent channel convective coefficient
k_w	test plate thermal conductivity
l_w	test plate thickness
M	magnification of optical system
Nu	Nusselt number
q''_{cond}	conductive heat flux
q''_{conv}	convective heat flux
q''_{rad}	radiative heat flux
q''_{tc}	turbulent channel reference heat flux
Re_s	slot Reynolds number
s	slot height
T_∞	mainstream temperature
T_{aw}	adiabatic wall temperature
T_{bw}	backside wall temperature
T_c	coolant temperature
T_w	non-adiabatic wall temperature
u	axial velocity component
u'	axial velocity fluctuation
u^+	axial velocity in wall units
U_∞	mainstream velocity
U_c	coolant peak velocity
U_{conv}	convective velocity
u_{RMS}	root-mean-square of axial velocity component
u_τ	shear velocity
v	wall-normal velocity component
v'	wall normal velocity fluctuation
v_{RMS}	root-mean-square of wall normal velocity component
y^+	wall-normal location in wall units
ε_i	emissivity of surface i
η_{aw}	adiabatic wall effectiveness
η_g	non-dimensional gas temperature
η_{na}	non-adiabatic wall effectiveness
λ	wavelength of laser
τ_w	shear stress at the wall

Chapter 1: Introduction

When components of an aerospace propulsion system are exposed to hot flowpath gases, the extreme heat loads can lead to catastrophic failures if proper thermal protection is not implemented. An inevitable tradeoff arises between high performance (directly proportional to operating temperature) and material duration and survivability. It is thus imperative to implement a thermal protection technique that balances the tradeoff and allows the system to perform optimally.

One such technique is film cooling, which has been implemented successfully in both air breathing engines and rocket combustors and nozzles. The technique consists of injecting a thin layer (the film) of relatively cool fluid near the surface to be protected, thus reducing the heat transfer to the surface. However, as the film inevitably mixes with the mainstream fluid, its ability to thermally protect the surface in question will decay to the point where protection is no longer available.

Figure 1 a)-c) shows characteristic examples of slot film cooling as applied to air breathing engines and rockets. In an air breathing engine, bleed air is diverted through louvered slots around the combustor liner to protect it from the much hotter combustion core. Bleed air is also typically injected through holes in the turbine blades and through slots in the turbine blade trailing edges. In some rockets, film cooling is used in conjunction with regenerative cooling to improve the thermal protection of the combustion chamber and nozzle. In this case, exhaust gases from the turbomachinery used to pump the fuel and oxidizer is fed through a manifold into the engine. These exhaust gases are injected tangentially at an approximate temperature of 900K, in contrast with the > 2700 K typically observed in the combustion core.

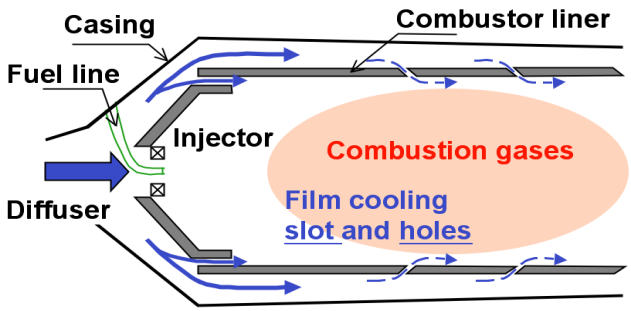

(a)

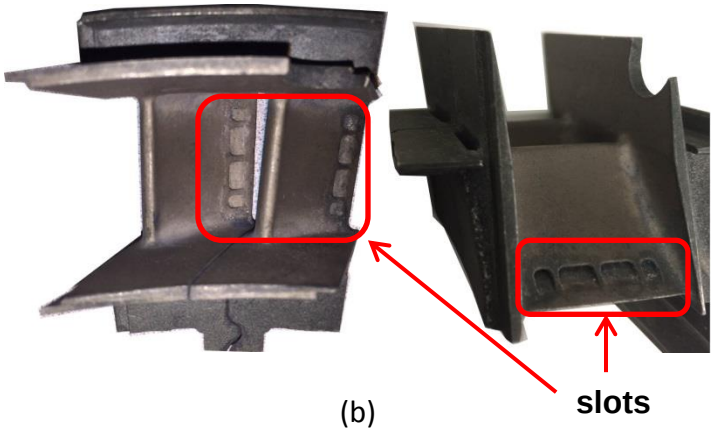

(b)

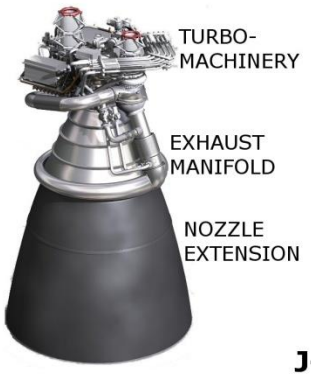

(c)

Figure 1. a) Film Cooling setup in gas turbine combustor (adapted from Cruz [1]). b) slots in trailing edge of turbine blades (courtesy of Dr. Ken Yu). c) J-2X engine concept drawing (courtesy of NASA)

Although similar in concept, film cooling in air breathing engines and rockets have noteworthy differences. In air breathing engines, both the mainstream and coolant are usually injected at subsonic speeds in a configuration where the coolant speed is typically higher than that of the mainstream. In rockets, at least the mainstream is usually supersonic, while the coolant can be injected at high subsonic or supersonic speeds, and the coolant velocity typically lags with respect to the mainstream velocity.

1.1 The Film Cooling Problem

In the simplest canonical 2-D form, the film cooling problem consists of a surface to be protected, a slot through which coolant is tangentially injected along said surface, and a hot mainstream. As the two streams mix due to shear, thermal and kinematic transport dictate how the surface is affected. Figure 2 shows this fundamental setup along with relevant inlet parameters, namely coolant velocity, U_c, coolant temperature, T_c, coolant density, ρ_c, mainstream velocity, U_∞, mainstream temperature, T_∞, mainstream density, ρ_∞, and slot height, s. Under adiabatic boundary conditions, the resulting wall temperature is commonly referred to in the literature as the adiabatic wall temperature, T_{aw}. Under non-adiabatic boundary conditions, the hot side wall temperature, T_w, and the backside wall temperature, T_{bw}, are also of relevance, as the gradient across the wall determines the conductive heat transfer. One can expect that the slot geometry, along with the injection conditions of the coolant and mainstream (velocity, temperature, density) should play a role on the subsequent mixing of the two streams, effectively determining the temperature of the surface downstream of injection (i.e. the behavior of T_{aw} vs. x). These injection parameters

and their ratios have indeed been shown in the literature to be relevant in determining film cooling performance.

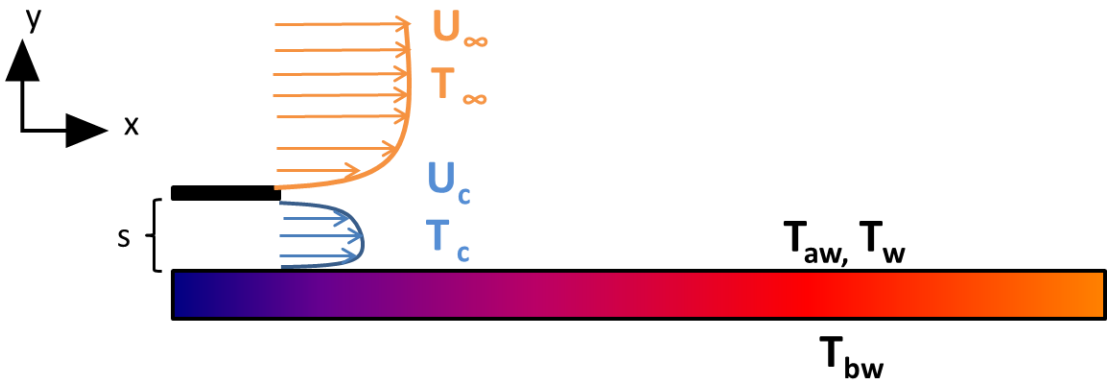

Figure 2. Canonical 2-D film cooling configuration and relevant paramenters.

1.2 Overview of the Literature

Identifying and understanding the effects of the governing parameters of film injection (velocity and temperature ratios, tangential vs. inclined injection, slot vs. hole injection, etc.) on film cooling performance has been a research topic of interest for the last 50 years. A significant portion of the research findings (particularly the earliest works) have focused on determining the influential parameters on film cooling performance, the length of protection of a particular film cooling setup and developing semi-empirical scaling laws for the behavior of the wall temperature based on these parameters.

Non-dimensionalizing the adiabatic wall effectiveness in terms of the injection temperatures leads to the adiabatic wall effectiveness, η_{aw}

$$\eta_{aw} = \frac{T_\infty - T_{aw}}{T_\infty - T_c}. \qquad (1)$$

This quantity is often used in the literature because it readily quantifies film cooling performance. For values close to unity, the wall temperature is close to the coolant temperature and the best protection is achieved. As the wall temperature approaches lower values, it is effectively approaching the mainstream temperature, revealing little to no protection from the film. Because of the importance of this paramenter, an important focus of the research community was aimed at identifying scaling laws for η_{aw} vs. x/s as a function of inlet parameters and geometry. Most of these scaling laws are very similar to one another and offer only incremental performance over the earliest work.

Later, as diagnostics evolved and they were applied to film cooling flows to gather global kinematic and thermal measurements, research focus shifted towards flowfield analysis, rather than looking at the protected surface only. Results from Laser Doppler Anemometry (LDA), Particle Image Velocimetry (PIV) and Infrared (IR) Thermography were used to gain further insight about film cooling, such as kinematic turbulence intensities and their effects, or convective heat transfer coefficient distributions on the test wall.

1.2.1 Scaling Laws

In 1946, Wieghardt [2] performed one of the first experimental investigations in a film cooling type of flow. Although his original application consisted of injecting warm air tangentially through a slot as a means for deicing, the underlying physics of this process are very similar to those governing film cooling. Wieghardt examined the entrainment of the film by the mainstream as a function of varying the blowing ratio, $m=(\rho U)_c/(\rho U)_\infty$ and injection angle. For isobaric flows, invoking the ideal gas law leads to $m = TR \text{x} VR$, where $TR=T_\infty/T_c$ and $VR=U_c/U_\infty$. Thus, the blowing ratio is a

function of the temperature ratio (TR) and the velocity ratio (VR), essentially depending on the thermal difference between streams, as well as the shear at injection.

Wieghardt then suggested a similarity expression for the flow temperature profiles

$$\frac{T_\infty - T}{T_\infty - T_{aw}} = \exp\left(- 0.768 \left(\frac{y}{\delta_T} \right)^{13/6} \right) \tag{2}$$

by normalizing the results based on the local adiabatic wall temperature, T_{aw}, and the local thermal boundary layer thickness, δ_T, where

$$\delta_T = \int_0^\infty \frac{T_\infty - T}{T_\infty - T_{aw}} dy \,. \tag{3}$$

Another semi-empirical relation presented by Wieghardt, related the local adiabatic wall temperature, T_{aw} to the slot geometry and flow parameters (velocities, temperatures and densities).

$$\frac{T - T_{ax}}{T - T_c} = 21.8 \left(\frac{x}{ms} \right)^{-0.8} \tag{4}$$

In 1953, Tribus and Klein [3] examined the boundary layers produced by jets of air discharged parallel to the surface. Their objective was to relate the adiabatic wall effectiveness to other relevant flow parameters. In general terms, the measure of merit lies in determining how η_{aw} behaves with downstream distance, x. These correlations can then be used to predict the lengthscale of protection for a given injection scenario.

Tribus and Klein derived an expression of the form

$$\eta_{aw} = C_1 \, \mathrm{Re}_s^{0.2} \left(\frac{x}{ms} \right)^{-0.8}, \qquad (5)$$

effectively relating the adiabatic wall effectiveness to the slot Reynolds number, $Re_s = U_c s / \nu_c$, the non-dimensional downstream distance, x/s, and the blowing ratio, m. When compared to the semi-empirical relationship derived earlier by Wieghardt, the authors reported that the main difference between the expressions was the $Re_s^{0.2}$ term, which Wieghardt seemed to have included directly in the calculation of the constant C_1. Tribus and Klein's result was one of the first to introduce the concept of the adiabatic wall effectiveness and the first to suggest that Re_s is an important governing parameter in this type of flow, along with the relevant velocities, temperatures and densities.

NASA's interest in film cooling led to a detailed parametric analysis of the technique, which resulted in several publications (Lewis, Papell, Trout) [4-6]. One of the first works revealed that the film cooling effectiveness was highly sensitive to the blowing ratio, the temperature ratio and the absolute coolant temperature. However, an absolute correlation could not be obtained, and instead 4 correlations were presented based on a range of values of the parameters of interest. The same research group expanded their work to derive an analytical model to predict the adiabatic wall temperature in a film cooled environment [5]. To do so, they assumed the film exists as a discrete thin layer, where there is no mixing between the coolant and the flow. Based on this rather gross assumption, the authors arrived to a general function relating the adiabatic effectiveness, η_{aw}, to the slot width, L, the downstream location, x, the length of constant adiabatic wall temperature near the injection, x', the

convective heat transfer coefficient, *h*, the coolant massflow, $\dot{m}_c$, and the coolant specific heat, $c_{p,c}$. The final form of this correlation

$$\eta_{aw} = \exp\left(-\frac{hL(x-x')}{\dot{m}_c c_{p,c}}\right) \tag{6}$$

was obtained by fitting this function to readily available data obtained both at NASA and General Electric.

Papell [6] extended the analysis from this model to angled slots and normal holes as injection methods for the coolant, effectively introducing a new parameter into the correlation. For angled slots, the new parameter was the effective slot injection angle, given as the angle of the fluid exiting the slot relative to the mainstream direction. For hole injection, an effective slot height, *s'*, obtained by relating the massflow through an actual slot to that through the holes, was used. The data showed that deviations from tangential injection usually result in decreased effectiveness. This result can be explained by the increased mixing due to the angularity between the streams inducing a higher level of mixing, which tends to "destroy" the film much sooner than in the tangential injection case. Although the parametric analysis from this group was important, the work was mostly engineering oriented, resulting in a wide number of correlations with very little insight into the actual physics of film cooling.

Hartnett et al. [7] built on Wieghardt's and Tribus and Klein's work by performing velocity measurements in addition to obtaining thermal and heat transfer characteristics in a film cooling scenario. This is perhaps one of the few comprehensive analyses found in the literature, albeit being restricted to a single slot

size, and a single blowing ratio. The authors replicated Wieghardt's slot configuration, and added a heat transfer plate, which was machined and instrumented with an array of heaters to actively control the boundary conditions. Velocity profiles were obtained with small pitot style probes, while thermal profiles were obtained with thermocouple probes. Two distinct experiments were performed to characterize the test section in general, and 2 other experiments dealt directly with film cooling. First, a solid flat plate experiment was run to obtain boundary layer velocity profiles in the wind tunnel. Once turbulent boundary layer profiles were obtained, the authors were then able to obtain the virtual origin of the boundary layer. In this same experiment, heat transfer to a plate with unheated starting length was also investigated and compared to theory, validating the use of the heat transfer plate for future studies. Next, an isothermal experiment with film injection was run to investigate the modified boundary layer profiles and to characterize the velocity profile inside the slot. Then, the authors performed adiabatic wall experiments with heated air injection. When compared to isothermal flow results, no significant effect from the heated film injection was found on the velocity profiles. As for the temperature profiles, these showed an expected variation in slope with downstream position. Similarly, when non-dimensionalized using Wieghardt's original analysis, the profiles were shown to collapse. However, plots of η_{aw} vs. x/ms, and comparison with previous data from other authors showed a 40% scatter of the data for which the authors did not have a concrete explanation. Finally, the constant heat input experiments allowed for the determination of Stanton number, $St(x)$, and comparison to the prediction from solid flat plate theory showed good agreement. Thus, at least for this configuration, the heat

transfer coefficient may be determined directly from a Stanton number correlation, or calculated directly from the known local values of q'', T_w *and* T_{aw} in the experiment.

In 1961, Seban and Back [8] performed an analysis on a wall jet scenario, where the coolant injection velocity is much greater than that of the mainstream. The authors obtained velocity profiles experimentally, and proceeded to compare them with classical wall jet theory, with good agreement. Turbulent boundary layer theory was also used to obtain shear coefficients from the law of the wall. For temperature profiles, the agreement is relatively good, but dependent on a modification of the eddy viscosity term in the theoretical expression. Finally, heat transfer was also obtained experimentally and compared to theory via the Colburn analogy, which relates the Stanton number to the Prandtl number and the friction coefficients. This comparison showed about 10% underprediction of heat transfer to the wall.

Later on, Stollery and El-Ehwany [9,10] derived a correlation for film cooling, based on a boundary-layer model, offering only incremental performance compared tothat of Tibus and Klein. The authors described that film cooling type flows can be broken down into 3 separate regions (as a function of downstream distance), namely a potential core where the wall temperature is very close to that of the coolant, a second region resembling a wall jet (in the case $U_c > U_\infty$) otherwise, this region does not exist, and finally a third region where the flow resembles a turbulent boundary layer. Their approach in this work was to re-derive an analytical expression for the wall temperature in the boundary layer zone. Following Wieghardt's initial analysis, as well as building on the work by Hartnett et al.. and Tribus and Klein, they arrived at the same correlation for the effectiveness. An alternate approach, which made use of

an enthalpy balance, led the authors to a very similar expression. However, the steps used in this alternative derivation allow for an easy extension to the cases of foreign gas injection and very large density ratios. Comparing this new expression to those of previous researchers, the authors realized that they all have the same general form except for the value of the leading coefficient C_1 which seemed to vary. They attributed these differences to the assumed form of the velocity profile in the derivation, since each author seemed to prefer a different form for it (exponential, 1/7 power law, etc). Finally, the authors compared their expression to some experimental data, and suggested that the scatter in Eckert et al..'s data, which was rather large, could be explained by including the effect of Re_s, much like Tribus and Klein did in their work. By doing so, the scatter was reduced, and data from Tribus and Klein, Wieghardt and Eckert all seemed to collapse very well. Recalling the definition of the velocity ratio, *VR*, the authors concluded that their expression is valid only for $VR < 1.5$, otherwise the flow can no longer be modeled with a boundary layer approach and a wall jet treatment should be used instead.

Goldstein [11] performed a comprehensive review of available film cooling literature up to 1971. His analysis dealt with both slot and hole injection film cooling, a summary of theoretical approaches, and a summary of experimental results. The author showed the evolution of film cooling research in time, as well as the different approaches taken to develop proper scaling laws. Since most models are semi-empirical in nature, Goldstein pointed out that they should be used carefully, and that, in general, they are only valid far away from the injection point. A very useful summary of the reviewed geometries and parameter ranges was also presented.

In 1973, Ballal and Lefebvre [12] expanded the analysis by Stollery and El-Ehwany to improve its accuracy in the near slot region. Obtaining skin friction coefficients in this region, and substituting them into Stollery and El-Ehwany's analysis provided a new expression

$$\eta_{aw} = 0.6\left(\frac{x}{ms}\right)^{-0.3}\left(\mathrm{Re}_s \frac{m\mu_c}{\mu_\infty}\right)^{0.15} \tag{7}$$

which was shown to agree within 5% of all of the data reviewed by Goldstein. It was valid for $0 < x/s < 150$, which made it clearly useful in the near slot region. However, it was not valid for large blowing ratios due to the assumptions in the velocity profile. To extend the analysis to other blowing ratios, the authors employed a wall jet model to derive a new expression for the effectiveness. The result was a piecewise correlation that presents discontinuities at the overlap region and thus, is assumed to capture film cooling decay only as an approximation (unlike the good agreement of the correlation for lower blowing ratios).

1.2.2 Influence of Turbulence Intensity

In 1986, Simon [13] at NASA built on the findings by Marek and Tacina [14] who suggested that turbulence intensities in the flow were also important parameters. Since film cooling is a mixing dominated flow, the turbulence intensities will have a significant effect on controlling the mixing strength, thus affecting the performance of the film cooling system. Using Marek and Tacina's data, and combining it with classic wall jet theory by Abramovich [15], Simon developed a semi-empirical model to include the effects of wall normal turbulence intensities in both the freestream and the slot, $I_{v,\infty}$ and $I_{v,s}$ respectively. This model was later used by Cruz and Marshall [16] as a basis for comparison to their data, with good agreement in the near slot

region. These models were some of the first deviations from correlation-based approaches, and emphasized the notion that turbulence at the inlet plays an important role on subsequent film cooling performance, even for similar mean inlet conditions.

Bons. et al.. [17] also investigated the effects of high freestream turbulence in film cooling. The geometry was that of a single row of holes, and freestream turbulence was generated by jets in crossflow. The idea was to replicate turbulent structures commonly found at the exit of gas turbine combustors. An elaborate experimental setup was used, instrumented to obtain temperature and velocity profiles. It was shown that for hole film cooling, the effects of freestream turbulence are dependent on hole arrangement geometry and blowing ratio. It is important, then, to adequately keep track of the turbulence intensities in the freestream when performing film cooling experiments.

1.2.3 Geometry effects

A quite comprehensive film cooling investigation was performed at Imperial College by Kacker and Whitelaw's group [18-21]. The authors systematically approached the film cooling problem by gradually investigating the kinematics and mass mixing of the two streams. As such, they presented an extensive body of work with kinematics and impervious wall effectiveness measurements for a wide range of velocity ratios covering wall wakes and wall jets, for a wide variety of lip thickness to slot height ratios. As opposed to realistic film cooling flows, their setup consisted of isothermal and iso-density flows, where one of the streams was contaminated with trace amounts of Helium. Wall probes connected to a spectroscopic analyzer would then determine the concentration of the contaminant. Invoking the heat-mass transfer

analogy, with the Lewis number close to unity, the authors then claimed that a mass based effectiveness was analogous to the adiabatic wall effectiveness.

Kinematics were obtained via hot wire measurements, with only the x-component of velocity being reported. Among their key findings was the fact that thick slots degrade the effectiveness due to the large mixing induced by the lip wake. The authors also noticed that for thin lips where this is not an issue, minimum shear type flows with VR ~ 1.0 exhibit the best effectiveness. Some drawbacks to their experimental undertaking were the lack of correlation among measurements, since kinematic and impervious wall effectiveness data was not obtained during the same experimental run. Kinematic data was also obtained at discrete *x/s* and *y/s* locations, only one velocity component was reported, and there wss no temporal correlation in the data due to its discrete, one point measurement nature.

1.2.4 Diagnostics

As discussed earlier, most kinematic data available early on was obtained through the use of hot wires. While these measurements offer an excellent temporal resolution, they are single point measurements in nature and thus, it is virtually impossible to obtain more than a few simultaneous velocity measurements. The intrusive nature of hot wire probes becomes even more so if simultaneous probes are introduced.

A workaround these issues can be obtained through minimally intrusive, global velocity measurement techniques such as Particle Image Velocimetry [22]. With this technique, a 2-D or 3-D velocity vector field can be obtained with minimal flow intrusion (it is an optical laser based measurement that requires flow seeding),

with all of the vectors being simultaneously obtained. This provides more data with less measurement times, with a relatively high spatial resolution.

As minimally intrusive diagnostics became easier to implement, it was only a matter of time for them to be used in film cooling type flows. Gogineni et al.. [23] used PIV to investigate turbulence intensity effects on film cooling. Using the same experimental facility of Bons, et al.., the implementation of PIV allowed the researchers to get accurate measurements of the 2-D velocity flowfield, as well as turbulence intensities. A qualitative analysis of the results obtained from a seeded coolant jet only showed that for blowing ratios $m < 1.0$, increasing the turbulence intensities significantly increases the spread of the coolant jet emanating from the holes. Sousa et al.. [24] performed a visualization study of near-wall flows with a PIV system (not film cooling type flows, ut rather boundary layers). They successfully obtained velocity profiles and turbulence statistics that closely agree with the classical law of the wall results from turbulent boundary layer theory and Direct Numerical Simulations from Spalart [25]. The authors suggested sampling a large number of images over a statistically significant amount of time (i.e, larger than the timescales of the flow), in order to improve the accuracy of the turbulence statistics. Fukushima et al. [26] also used PIV and Planar Induced Fluorescence (PLIF) to investigate the mixing process in an axysimmetric turbulent jet. Their results were in very good agreement with DNS investigations.

Peterson [27] also used the PIV technique to obtain structural features of jets in crossflow for film cooling applications. This detailed study showed the enormous potential of PIV as a useful tool for characterizing film cooling flows. Peterson was

able to obtain instantaneous flow structures inside a single film cooling hole and track their evolution downstream of the injection point. Polanka et al. [28] used stereoscopic PIV to obtain the 3 velocity components near the stagnation region of a turbine blade with film cooling. Such a complex flow was adequately characterized by PIV and the authors emphasized that the results can be of great value to CFD model development. More recently, Chen and Eaton [29] have also used the PIV technique in a water tunnel to measure the kinematics of film slot injection in an airfoil trailing edge. For a more detailed explanation of the PIV technique and its direct application to turbulent mixing flow measurements, the reader is referred to Kaehler [30].

Thermocouples have been used in a few film cooling studies, although most of those available in the literature are isothermal flows. Microthermocouples have been used in the investigation of high temperature turbulent flows due to their ability to resolve fast timescales (kHz range) with minimal radiation contamination due to the bead's small surface area. Marshall [31] used microthermocouples to investigate swirling flame temperatures and Cruz and Marshall [16] used them in film cooling research. Kunugi and Jinno's [32] approach for compensation of thermocouple measurements was adapted by Marshall for flame measurements, slightly modified by Cruz [1] for film cooling and was further refined in this work and is explained in further detail in the investigative methodology section.

1.2.5 CFD Model development and validation

With the advent of modern computational techniques, CFD modelers soon turned their attention to the film cooling problem. RANS and LES models have been developed for different configurations, using diverse experimental results for

validation. The most common issue that arises when trying to validate a CFD model is the lack of comprehensive data. Most of the studies available in the literature are somewhat incomplete (i.e. thermal data is available, but not kinematic data, boundary conditions are not truly adiabatic, etc.). This lack of a complete and comprehensive data set restricts the development of a model. Jansson et al. [33] used some available data within their research group to compare a two-layer algebraic stress model with measurements. The data consisted of kinematic and thermal mixing for 2 velocity ratios (VR =1.0, 1.5). Kinematic data was obtained from a single component hot wire and could not be decomposed into the more useful tangential and wall normal directions to analyze the 2-D nature of the problem in more detail. The thermal data exhibited a very weak temperature ratio between the two streams, and the authors also acknowledged repeatability issues. As expected, the model compares favorably with the kinematic data, but not at all with the thermal data.

Kacker and Whitelaw [19] also used their wide body of data to test a finite difference model they developed. Because their data was available as separate sets, they compared kinematics to one data set, mass mixing to a second set and impervious wall effectiveness to a third set. The overall agreement was good under certain conditions, but both the model and the data were only good for flows with no density gradients (i.e. isothermal, iso-density flows).

A more recent attempt at validating RANS and LES with experimental data was done by Cruz [1] and Dellimore [34] at the University of Maryland. Cruz used kinematic, thermal mixing, adiabatic and heat transfer data obtained in a hot wind tunnel to validate an in-house developed RANS and LES code with relatively

satisfactory results. The experimental and modeling campaigns were developed simultaneously with constant feedback between experimentalists and modelers, such that the experimental data was of the optimum quality for its use in CFD models. As such, kinematic data was 2-D global, thermal mixing and adiabatic wall measurements were taken during the same experimental run as the velocity measurements, and a second set of thermal data with non-adiabatic boundary conditions was also obtained. This was performed for 3 velocity ratios covering wall-wake, min-shear and wall-jet scenarios. Both RANS and LES models were constant density codes, whereas the data was not obtained at such conditions. Furthermore, the experimental data exhibited some entrainment due to a minor leak in the test section. While the overall agreement was good, the discrepancies between CFD and data could be explained by these factors. Dellimore used the same data as Cruz to compare experimental measurements to a semi-empirical model he developed as well as to results from a NASA based CFD code called LOCI-CHEM. Dellimore's results were similar to those of Cruz, although the performance in the RANS code was relatively inferior.

Voegele [35] recently built on the findings of Cruz and Dellimore and used improved data obtained by Raffan [36] to test a variety of inlet treatments in a RANS model. Voegele's results showed an improvement in the CFD vs. experimental agreement, particularly for the cases in which the inlet plane for the simulations was moved upstream of the film injection plane. Voegele's work has also shown the importance of correctly prescribing inlet turbulence in order to adequately capture film cooling performance.

1.3 Objectives of the current research

While there is a breadth of work with regards to film cooling in the open literature, there still remains a fundamental need for a comprehensive and complete experimental database for model development and validation, particularly with regards to realistic film cooling flows (non-isothermal, backside cooled) over a wide range of blowing ratios. Based on this need, this work addresses those requirements and presents a comprehensive experimental database in a canonical slot geometry (2-D, thin lip, low mainstream turbulent intensity) covering a set of velocity ratios that correspond to three fundamentally distinct initial shear configurations (under subsonic flow conditions).

The comprehensive nature of the measurements covers kinematic, thermal mixing, wall surface temperatures and heat transfer measurements, thus obtaining mean and turbulent information about all of the relevant flow behavior (mixing & transport, as well as near wall interactions) and the intrinsic kinematic-thermal coupling. Special attention is placed on the inlets and near-injection region such that the entire domain only extends up to x/s = 40-50. Capturing this region is of great importance because the near injection region is where the initial mixing conditions that determine film cooling performance are established. It is also worth noting that, based on material properties and operating conditions in actual propulsion systems, an Inconel nozzle will reach its melting point at η_{aw} = 0.70-0.75, values which have been observed relatively close to the injection location in previous studies.

With that in mind, the general objectives of this work are:

- Obtain a unique experimental database of slot film cooling under canonical conditions (heated mainstream, 3 shear scenarios, adiabatic-non adiabatic boundary conditions).
- Develop a comprehensive approach to characterize slot film cooling (detailed inlet information including turbulent data, mean and turbulent kinematics and thermal mixing information in the flowfield, wall temperatures and heat transfer).
- Adapt and implement advanced diagnostics and data analysis methods to characterize film cooling transport processes.

It is worth pointing out that obtaining a similar database was attempted earlier in our research group [37]. However, the quality of the obtained data was compromised by a faulty test section (an improperly sealed window provided a leakpath for cold air entrainment). Furthermore, the signal to noise ratio of the kinematic measurements near the wall was too high, compromising the near-wall resolution and affecting the accuracy of wall location. These detrimental effects have been corrected and the quality of the data for this dissertation has vastly improved compared to that first attempt.

Chapter 2: Investigative Methodology

One of the major contributions of this work is the design and execution of a comprehensive experimental approach to characterize film cooling flows with unique data under a wide range of relevant conditions. The uniqueness of the experimental facility, the rationalization behind the choice of diagnostics and the careful thought that went into the overall approach are presented in this chapter with the aim of allowing the reader to understand and appreciate the inherent value of the experimental campaign in addition to the results extracted from it.

2.1 Experimental Facility Design

The fundamental experimental facility used in this experimental investigation is a unique hot wind tunnel built by Cruz and Marshall [16] to perform film cooling experiments. It consists of a centrifugal fan to drive the flow, an inline methane burner to raise the freestream temperature to approximately 473K, a turning elbow with guiding vanes, a settling chamber with ceramic saddles and screens to homogenize the flow thermally and kinematically (essentially reducing the presence of large scale turbulence), a contraction section to accelerate the flow, a test section and a diffuser and exhaust system. The fact that the mainstream can be heated well above the coolant temperature makes this facility unique as it is able to simulate similar physical film cooling conditions, albeit at a reduced thermal scale. Figure 3 shows the details of the wind tunnel, while Table 1 summarizes the main flow parameters achievable in the wind tunnel. Unlike many of the works available in the literature, the wind tunnel provides realistic conditions (hot flow with a significant

temperature ratio) albeit scaled from those observed in real applications. For more detailed information on the wind tunnel, the reader is referred to Cruz and Marshall [1,16].

2.1.1 Test Section

Because the wind tunnel was originally built for adiabatic experiments and thermal measurements only, a new test section was designed and built to accommodate the objectives of this work. Since both adiabatic and non-adiabatic conditions were of interest, the new test plate had to be of relatively low thermal conductivity to provide a credible adiabatic condition while providing large (> 10 K) measurable temperature differences across a relatively small thickness (~1/4 inch) in the non-adiabatic cases.

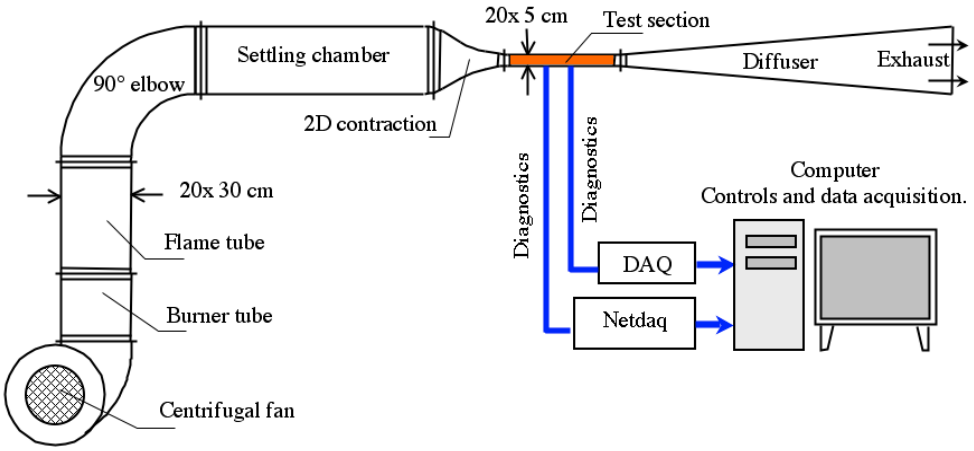

Figure 3. UMD Hot Wind Tunnel (adapted from Cruz and Marshall [16])

Table 1. UMD hot wind tunnel operating conditions

	Quantities	Experimental Values	Remarks
Operating Conditions	U_∞ U_c T_∞ T_c T_{bw}	up to 40 m/s up to 50 m/s 300 - 500 K ≈ 300K ≈ 285K	Mainstream velocity Cooling film velocity Mainstream temperature Cooling film temperature Backside cooling temperature
Dimensionless Parameters	Re_s VR TR m	2000 – 8000 0 - 3 1 - 2 0 - 6	Turbulent film flow $VR = U_c/ U_\infty$ $TR = T_\infty/T_c$ $m \approx VR \; x \; TR$

After an extensive material search, UDEL®, a high temperature thermoplastic was chosen as the wall material. The original test section casing was modified to incorporate large windows for PIV. The overall dimensions of the test section are 5.1 cm x 20.3 cm inches x 50.8 cm, while the windows are 4.4 cm x 30.5 cm. The test plate is 8.1 cm thick.

Previous work by Cruz [1] and Raffan [37] revealed defective window seals which led to entrainment of external air into the test section. Experimental evidence suggests that this entrainment compromised the far stream behavior of the flow and it is reasonable to suspect that it may have also compromised the near wall flow. Despite this entrainment not being of a completely destructive nature, the pressure gradients associated with the phenomena may have moved the parameter space into a non-canonical configuration where pressure gradients are of importance, but were not accurately measured. For the purpose of this work, these issues have been completely

resolved and the parameter space is once again in a canonical configuration with no pressure gradient effects (constant area test section).

A canonical test configuration is an essential resource for a model developer since one could reasonably expect that if a model fails to compare favorably to a canonical configuration, it will undoubtedly fail under a far more complex one. With this in mind, the test section was designed as a canonical 2-D slot, while retaining some features from realistic slot configurations. The film cooling slot consisted of a stainless steel louver attached to the test plate. The slot height, s, was fixed at 4 mm, while the louver thickness, t, was 0.76 mm. This resulted in a lip thickness to slot height ratio, $t/s < 0.4$, which minimizes lip thickness effects as suggested by Goldstein [11]. During experimental runs, heat loads to the louver resulted in observed thermal expansion leading to increases in the slot heights. Because different blowing ratios led to different heating rates of the louver plate, there were 3 distinct louver heights corresponding to each of the cases ranging from 5.3 to 6.1 mm. For the non-adiabatic cases, the slot was rebuilt to address the thermal expansion issue and the slot was kept nominally at $s = 4$ mm. Despite the variation in adiabatic cases, the criteria of $t/s < 40$ was satisfied among all cases.

The film was generated using a plenum attached to the back of the test plate. A small row of holes was used to feed air from the plenum into the slot. As the jets impinged, mixed, and flowed downstream, the film flow was established. This film generation setup was implemented as it closely resembles real life implementations in both gas turbines and rockets while retaining the more canonical configuration of a single slot with no internal structures and a relatively simple flowfield inside the slot,

as opposed to internal ribs and pylons and S shaped flows prior to injection as observed in some gas turbine designs (Hill and Peterson [38]).

For non-adiabatic experiments, a water jacket was attached to the backside of the test plate. Water was pre-chilled using a NesLabs 500-700 Watt chiller and an insulated reservoir tank. A sump pump was used to drive the cold water from the tank to the water jacket and back in an open loop configuration while running the chiller in parallel. Four surface thermocouples were installed on the back of the test plate to monitor the wall temperature distribution on the water cooled side. For the adiabatic cases, the water jacket was removed, and an insulating board was attached to the backside of the test plate to further minimize heat loss. Figure 4 shows a picture of the assembled test section, while Figure 5 shows a 2-D schematic of the test section.

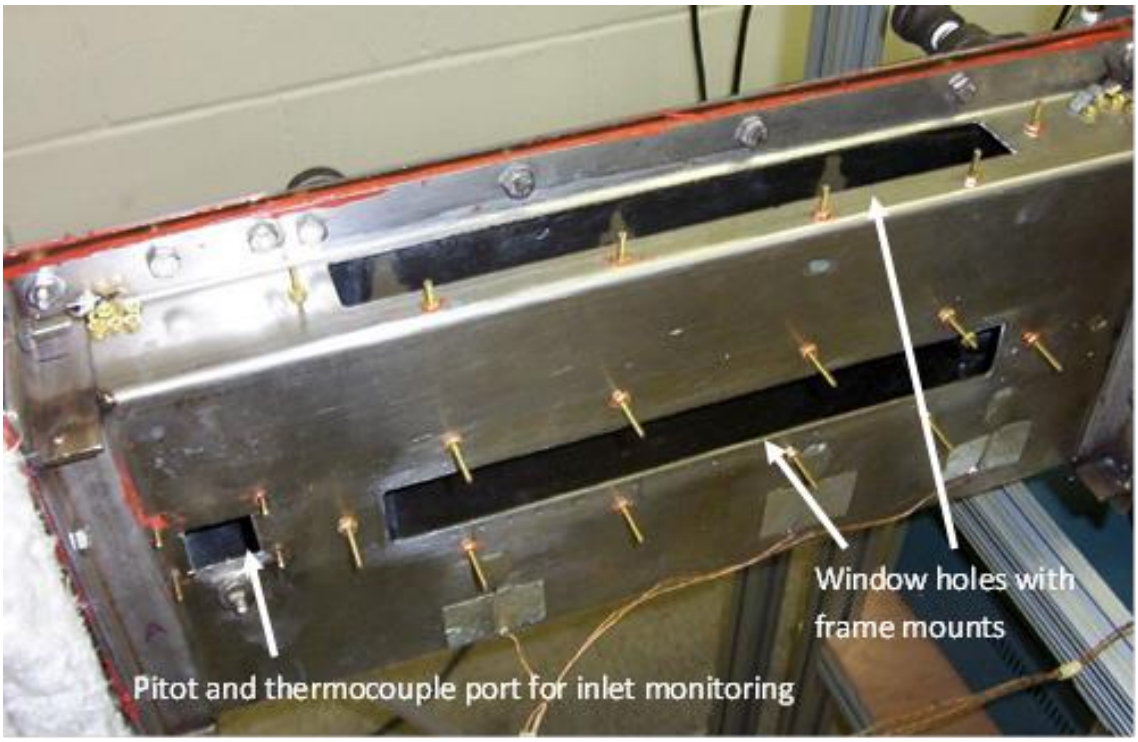

Figure 4. Assembled test section

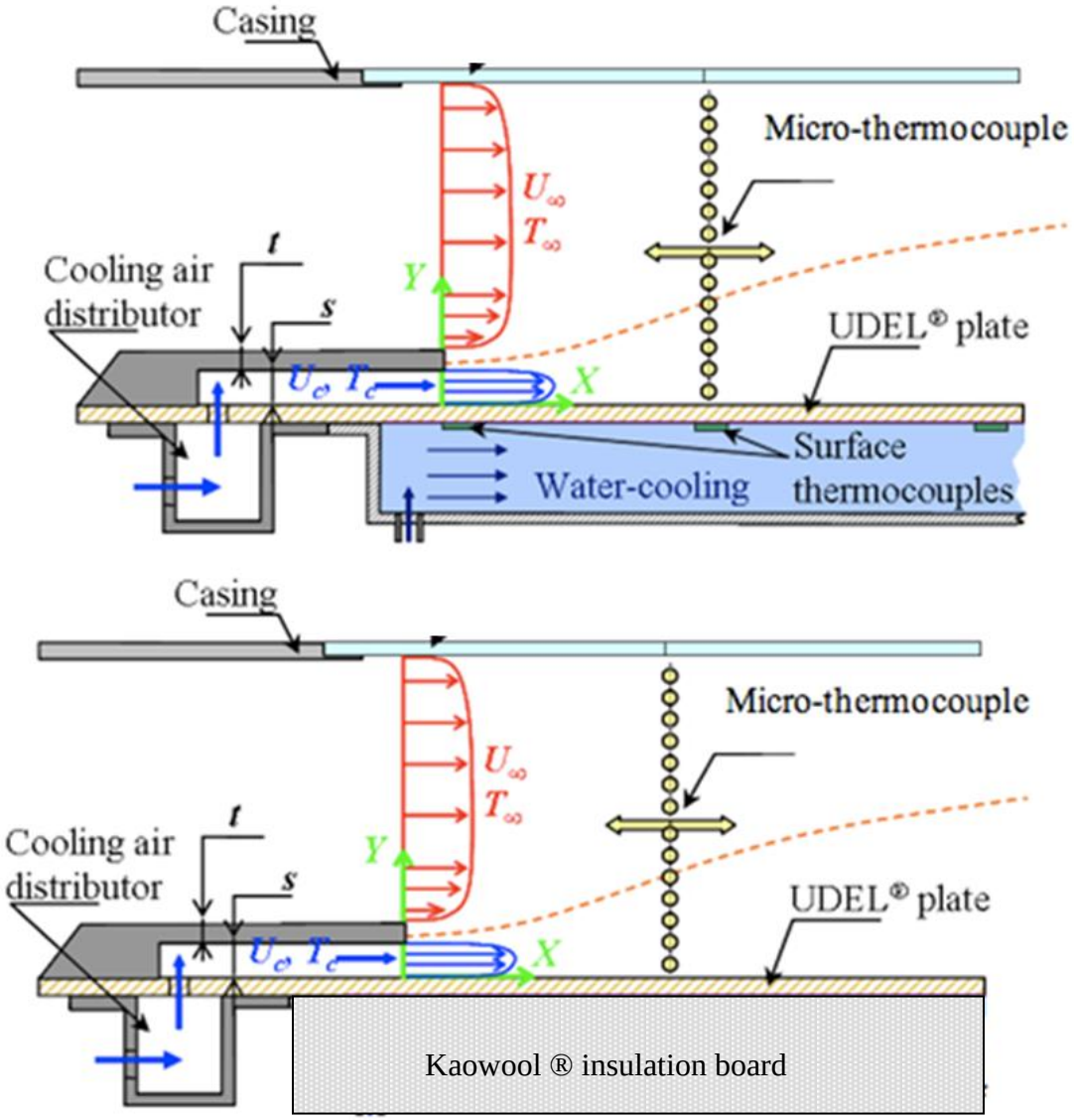

Figure 5. Adiabatic and Non-adiabatic test section and diagnostics

2.2 Diagnostics and data analysis

The advanced diagnostics (PIV, microthermocouples) used to perform the measurements in this work were chosen due to their minimally intrusive nature in order to minimize flow disturbances. Each diagnostic tool has also been chosen for its unique advantages and suitability for the challenging flow setup in question.

Particle Image Velocimetry (PIV) was chosen for kinematic measurements due to its 2-D global nature. This allowed for the measurement of the entire 2-D velocity field, with each point in the instantaneous velocity field being acquired simultaneously. PIV data can be time averaged to provide mean and fluctuating kinematic data everywhere in the flow. Additionally, its global nature allows for the quantitative and qualitative visualization of coherent structures. All of these features provide spatially resolved inlet and flowfield kinematic data with enough fidelity for subsequent use by modelers.

Fast response microthermocouple probes were used to obtain streamwise flow temperature profiles as well as wall temperatures with the microthermocouple in contact with the wall. Unlike PIV, these thermocouples do not provide global data, but are rather point measurements. However, their fast response (in the kHz range), provides important temporal information about the turbulence. Time averaging thermocouple data and sampling enough points in space also allows for a quasi-global 2-D interpretation of the mean thermal data. Fluctuating temperature data can be used to characterize thermal mixing.

In addition to these main diagnostics, backside surface thermocouples were used to monitor the water cooled wall temperatures in the non-adiabatic cases and the temperature information was used to calculate heat transfer across the plate.

2.2.1 Particle Image Velocimetry (PIV)

PIV is a widely used technique for measuring the 2-D velocity flowfield in a plane; by extension one can also measure the out of plane velocity component with stereoscopic imaging. A typical PIV system consists of a pulsed laser, a camera, and a particle seeding system. The seeding system introduces particles into the flow whose

sizes are carefully tailored to both follow the flow faithfully and scatter enough light to be detected by the camera [22]. The particles are illuminated by a planar laser sheet produced with a cylindrical lens.

The pulsed laser and the camera are synchronized such that two consecutive images are acquired. This effectively "freezes" a planar slice of the flow at two instants separated by the gate time, Δt. A cross-correlation algorithm is applied to obtain the net displacement vector of the particles at different points in the imaging area. The local velocities are then obtained by dividing the calculated 2-D displacement by the known gate time. Figure 6 shows a schematic diagram of a typical PIV setup and operation.

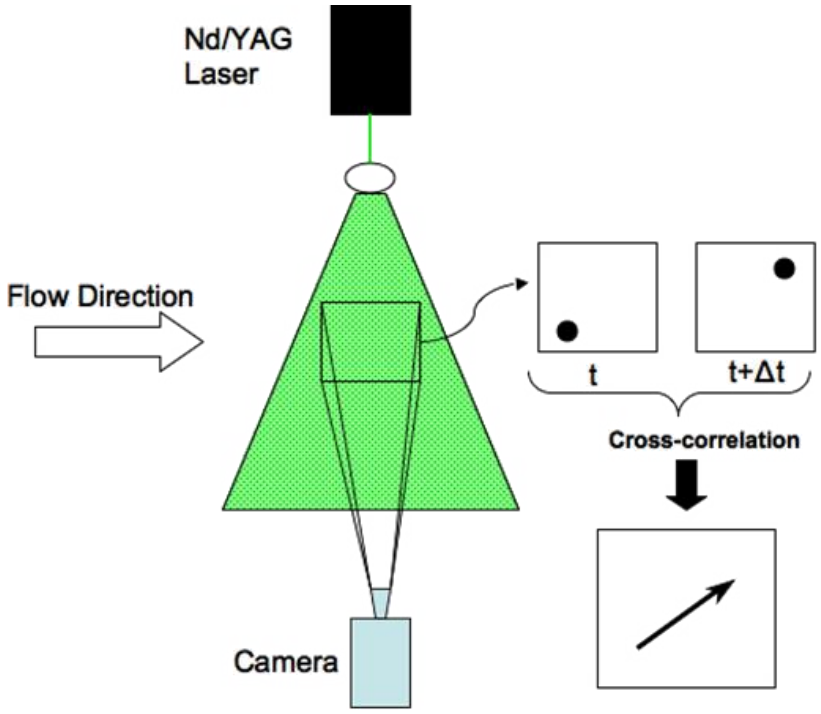

Figure 6. Typical PIV system components and operation (adapted from Raffel [22]).

2.2.1.1 PIV imaging

To obtain reliable results, a particle's image on the camera sensor must be greater than a single pixel. In general, the diameter of a particle's image on a CCD chip is given by:

$$d_i = \sqrt{(Md_p)^2 + d_{diff}{}^2} \tag{8}$$

where d_p is the physical diameter of the particle, M is the magnification of the optical system and d_{diff} is the so called diffraction limited image diameter given by:

$$d_{diff} = 2.44 f_{\#}(M+1)\lambda \tag{9}$$

where $f_{\#}$ is the f-number of the lens system, and λ is the wavelength of the incident light on the particle. From these equations, it is evident that the image diameter of a particle differs from its physical diameter not only due to magnification, but also due to the scattered light's wavelength and lens setup. This allows for some control of the optimum particle image diameter without necessarily compromising the field of view, although tradeoffs are inevitable.

Raffel [22] showed that PIV errors were minimized when the seeding distribution is high (> 4 particles per interrogation window), pixel displacement is on the order of ¼ of an interrogation window, and particle image diameter d_i = 2 pixels. Recalling equations 8 and 9, the green laser used in PIV corresponds to λ = 532 nm, and seeding particles have a nominal physical diameter of 0.3-1.0 μm. Based on this, a field of view of 3.5 cm x 3.5 cm, with a resulting magnification M = 0.43 was chosen. The f-number of the lens was $f_{\#}$ = 8, and average particle image diameters d_i were on the order of 15 μm, or ~ 2 pixels given the sensor pixel size of 7.4 μm, satisfying the requirement to minimize PIV errors.

2.2.1.2 PIV seeding

Titanium dioxide (TiO_2) in powder form was chosen as the seeding particle for the mainstream, since it is one of the few substances that can be introduced upstream of the in-line combustor without compromising its composition or physical state (as opposed to liquid droplets that may evaporate or burn). Previous work showed that the TiO_2 particles tended to deposit on surfaces, easily obstructing the film holes. This required tedious cleanups after every test which included disassembling the entire test section. To work around this, the film flow was seeded with Diethylhexyl Sebacate (DEHS) oil droplets generated upstream of the plenum by a liquid droplet generator. These particles do not obstruct the flowpath and residue tends to evaporate over time. Also, since these particles are never exposed to the burner temperatures, they will not burn or evaporate as the flow temperature in the test section is well below the boiling temperature of the DEH particles (250 °C).

The question of whether or not these particles can faithfully follow the flow in question is addressed by Stokes drag analysis. An approximation to the lag velocity of a small particle with respect to the local fluid velocity is given by Raffel [22] as

$$\vec{U}_p - \vec{U} = \frac{d_p^2(\rho_p - \rho)}{18\mu}\vec{a} \qquad (10)$$

where U is the local fluid velocity, U_p is the particle velocity, ρ is the fluid density, ρ_p is the particle density, μ is the dynamic viscosity of the fluid and $\boldsymbol{a}$ is the local acceleration. One can readily see that for a given acceleration, this lag is minimized in the limit of infinitely small particles ($d_p \rightarrow 0$) or if the particle and fluid density are matched ($\rho = \rho_p$). In the cases of gaseous flows, matching the density of the fluid and

particles is nearly impossible. However, the fluid density is negligible with respect to that of the particle and the relationship reduces to

$$\vec{U}_p - \vec{U} = \frac{d_p^2 \rho_p}{18\mu} \vec{a} \tag{11}$$

From this relationship we can interpret the term

$$\tau_p = \frac{d_p^2 \rho_p}{18\mu} \tag{12}$$

as the characteristic response time of a particle to a step change in fluid velocity, and as expected, this response time is minimized by reducing the particle size.

Samimy et al. [39] suggest that for a given turbulent timescale τ_T, the particle will follow the flow within 2% error if

$$\frac{\tau_p}{\tau_T} \leq 0.2 \tag{13}$$

while Scarano [40] suggests that up to 1% error is acceptable (corresponding to $\tau_p/\tau_T = 0.1$). In general, Samimy et al. showed that the % error in particle lag scales directly with τ_p/τ_T as

$$\%error = 10\frac{\tau_p}{\tau_T} \tag{14}$$

up to 10% error for $\tau_p/\tau_T = 1$.

Given that turbulent timescales are bounded by the integral timescale (largest) and Kolmogorov timescale (smallest) (Pope [41]), we can compare these characteristic timescales to the response times of our seeding particle choices to determine whether or not the choice is satisfactory. The integral timescale τ_0 is related

to the integral lengtscale, L_0 and the largest estimated turbulent fluctuation velocity U_0 by

$$\tau_0 = \frac{L_0}{U_0} \tag{15}$$

The integral timescale can then be related to the Kolmogorov scale τ_K by invoking the energy cascade (Pope [41]), yielding

$$\tau_K \cong \tau_0 Re_0^{-1/2} \tag{16}$$

where Re_0 is the Reynolds number based on L_0 and U_0. Based on the capabilities of the experimental facility, a good conservative estimate of the characteristic timescales in the experiments can be derived.

Assuming a mean flow velocity of 20 m/s with an RMS of 15% (a conservative estimate based on a priori observations), and assuming the integral lengthscale to be on the order of the slot height, then $L_0 = s$, U_0 = 20 x 0.15 = 3 m/s. Assuming nominal particle sizes of 0.3-1.0 microns for TiO_2 and 1 micron for DEHS, Table 2 summarizes the timescales and response times of the seeding particles of interest. Both TiO_2 and DEHS particles follow the flow faithfully to within 0.5 - 2% error. Thus, both seeding choices are valid. Once again, this is a conservative estimate, and it is very likely that particles follow the flow well below 1% error.

The mainstream seeder was built using a fluidized bed design consisting of PVC pipe and a brass sintered plate. High pressure air entered the seeder from the bottom, passed vertically upwards through the sintered plates and mixed with the loosely packed TiO_2. This agitates the particles creating a mixture of air and particles that is then forced through a ¼" tube by the air pressure. The tube exits at the top of

Table 2. Particle relaxation times and Stokes numbers for the current study.

Particle relaxation times (s)		τ_p, s (TiO_2, 0.3 µm)	1.1×10^{-6}
		τ_p, s (TiO_2, 1 µm)	1.2×10^{-5}
		τ_p, s (DEHS, 1 µm)	2.5×10^{-6}
	Wall Wake	**Min Shear**	**Wall Jet**
L_0, mm	6.1	5.7	5.3
Re_0	1200	1100	1000
τ_0, s	2.1×10^{-3}	1.9×10^{-3}	1.8×10^{-3}
τ_k, s	6.0×10^{-5}	5.8×10^{-5}	5.6×10^{-5}
τ_p / τ_k (TiO_2, 0.3 µm)	1.8×10^{-2}	1.9×10^{-2}	1.9×10^{-2}
τ_p / τ_k (TiO_2, 1 µm)	2.0×10^{-1}	2.1×10^{-1}	2.1×10^{-1}
τ_p / τ_k (DEHS, 1 micron)	4.2×10^{-2}	4.4×10^{-2}	4.5×10^{-2}

the assembly and the seeding can then be directed to the point of injection as required as seen in Figure 7 a).

The film seeder is a commercially available design consisting of a set of Laskin nozzles submerged in the DEHS oil. High pressure air is fed through the 1 mm diameter nozzle which generates the droplets. The droplets mix with the air and are filtered by a thin impactor plate such that only the thinnest droplets can exit the seeder, while larger particles coalesce and drop back into the reservoir, as shown in Figure 6 b). Mainstream seeding was introduced directly upstream of the combustor, while film seeding was injected upstream of the plenum. This injection setup was designed to maximize the residence time of the particles in the flow so that any disturbances arising from the seeding injection are smoothed out by the time the

particles reach the test section.

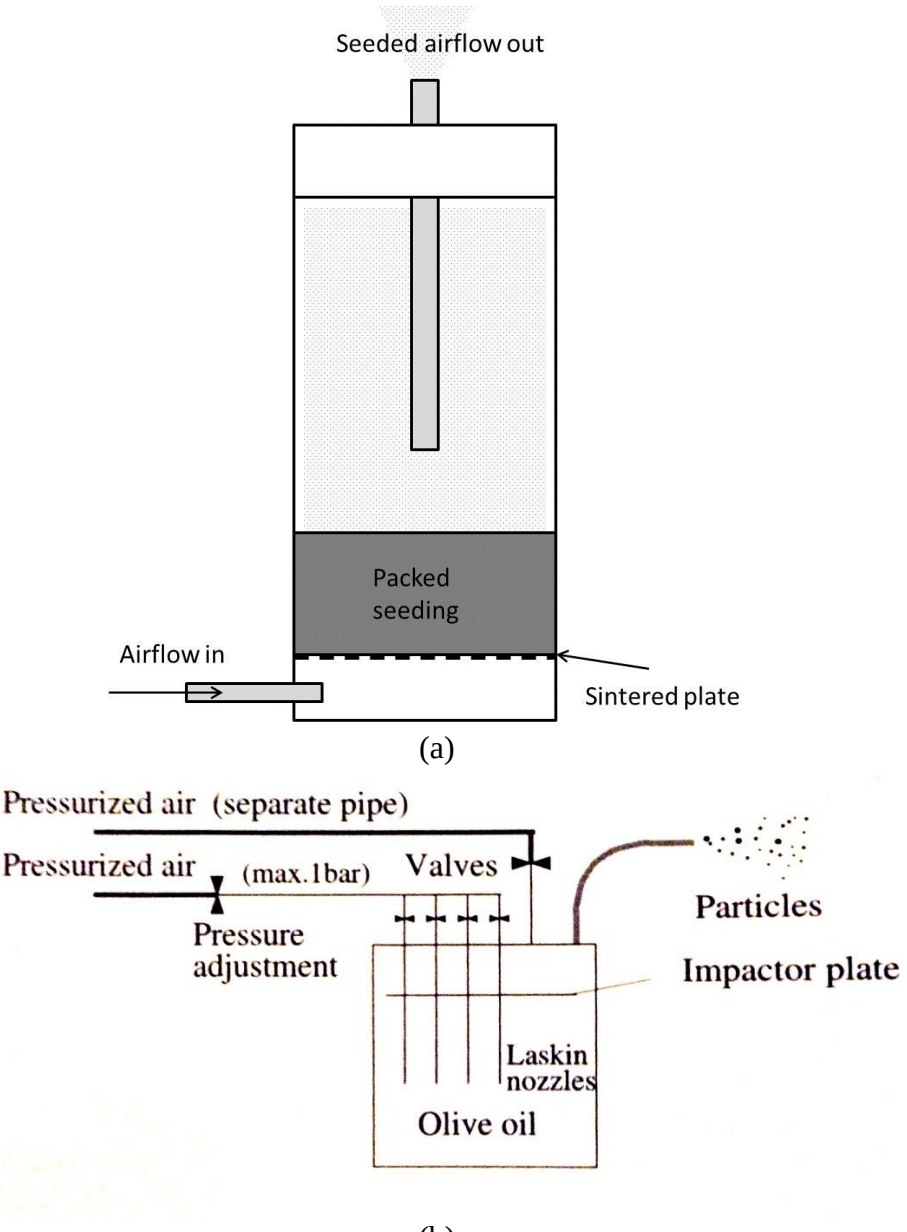

Figure 7. a) Solid particle seeder for mainstream. b) Liquid droplet generator for film. Adapted from Raffel [22]

2.2.1.3 PIV algorithm

In its simplest form, a PIV algorithm will first divide the images into interrogation windows of a predetermined size and match identical interrogation windows from one image to the other. One can then easily see that particles close to

the edges of an interrogation region in the first image may be absent in the matching interrogation region of the second image. This is known as in-plane loss of particles. Furthermore, if the gate time is too large, then one may lose all of the particles from one interrogation region to the next. In general, the displacement should be on the order of ¼ of the interrogation window size to minimize these effects. However, since the gate time is a global parameter that applies to the entire image, minimizing loss of in-plane particles for a certain region of the flow with velocity U_1 may lead to barely detectable displacements in regions of the flow with lower velocities $U_2 < U_1$.

Westerweel et al. [42, 43] devised a workaround to address this issue by using multiple passes in the displacement calculation algorithm. The algorithm starts by dividing the image into relatively large windows and proceeds to obtain a coarse displacement field. On the next pass, the algorithm uses this displacement information to match *displaced windows* (i.e. the interrogation window from image A is matched to an interrogation window in image B that has been shifted in space by the displacement calculated in the previous pass). This method extends the dynamic range of the calculation, allowing the user to tailor the gate time for the lower range of velocities while the multiple passes counteract the in-plane loss of particles due to higher velocity motion. In an experiment it is wise to get an estimate for the gate time assuming the smallest window size and the lowest velocity value between U_c and U_∞. Test images are acquired and the algorithm is tested. This usually requires some minor iteration until the optimum gate time is obtained such that the entire flowfield is well resolved. For this work, the resulting gate time was $\Delta t = 8\mu s$ and the multiple pass algorithm started with a 32 x 32 pixel window down to 16 x 16 pixels with a

50% overlap. This spatial overlap increases the spatial resolution and is particularly useful in regions where velocity gradients are important, such as near the wall and in the mixing layer. Figure 8 shows a schematic on how the algorithm operates.

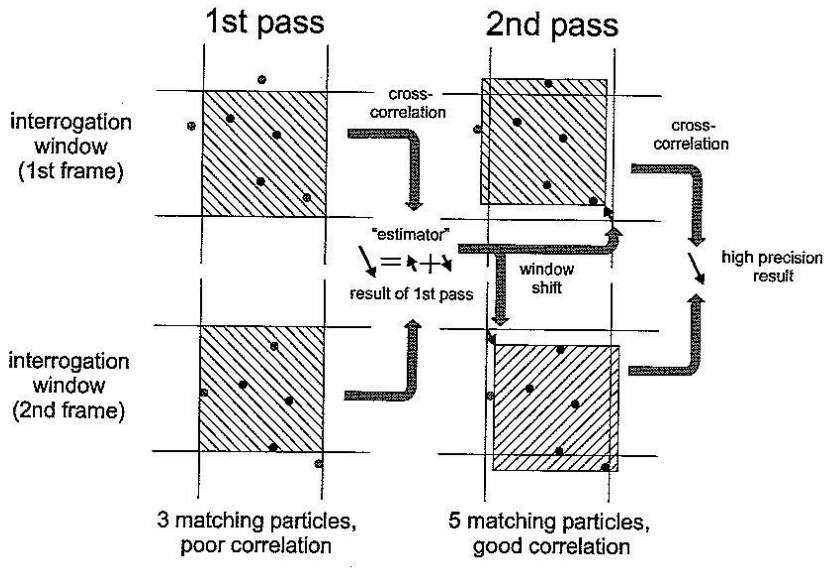

Figure 8. Multiple pass PIV algorithm. Adapted from LaVision Manual [44] Based on the theory of Westerweel et al.[43]

The wall was treated with black spray acrylic paint in order to minimize wall reflections and improve the signal to noise ratio in this region. A single camera Lavision PIV system was used in this work. It consisted of a 4 megapixel Imager ProX camera, a New Wave Research SoloPIV double cavity pulsed Nd/YAG laser with up to 100 mJ per pulse and a processing computer. Early PIV recordings with hot and cold flow in the wind tunnel showed that convergence of the mean statistics was achieved with ~ 200 images, while convergence of RMS statistics required ~ 250-350 images (Figure 9). Per the suggestions of Sousa et al. [24] a total of 500 image pairs were obtained at each downstream station in order to obtain statistically significant turbulence measurements. Six measurement stations were necessary to

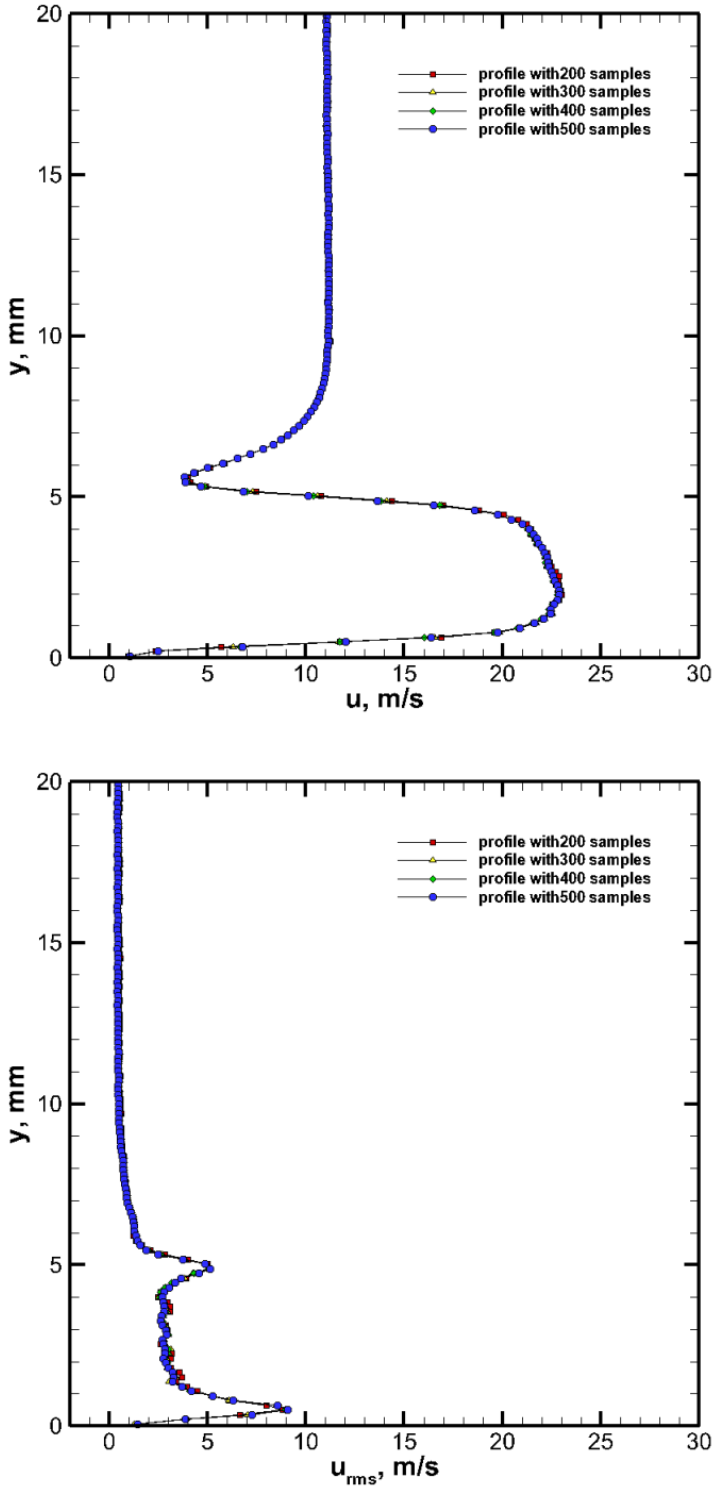

Figure 9. Convergence of mean and RMS statistics for PIV measurements

cover the entire length of the test plate resulting in a total of 3000 image pairs per experimental case. The images were post processed with the multiple pass, reducing window size approach. LaVision's Davis software was used to obtain the instantaneous velocity vector fields. Images of a seeded mainstream alone were also taken to provide flow visualization of mixing structures. Further post-processing of the data was done in house to obtain higher order statistics. Figure 10 shows a picture of the PIV system setup in the wind tunnel. Works by Raffel [22], Westerweel et al. [42,43] and Adrian [45] were used as guidelines for the setup and implementation of the PIV system in this work.

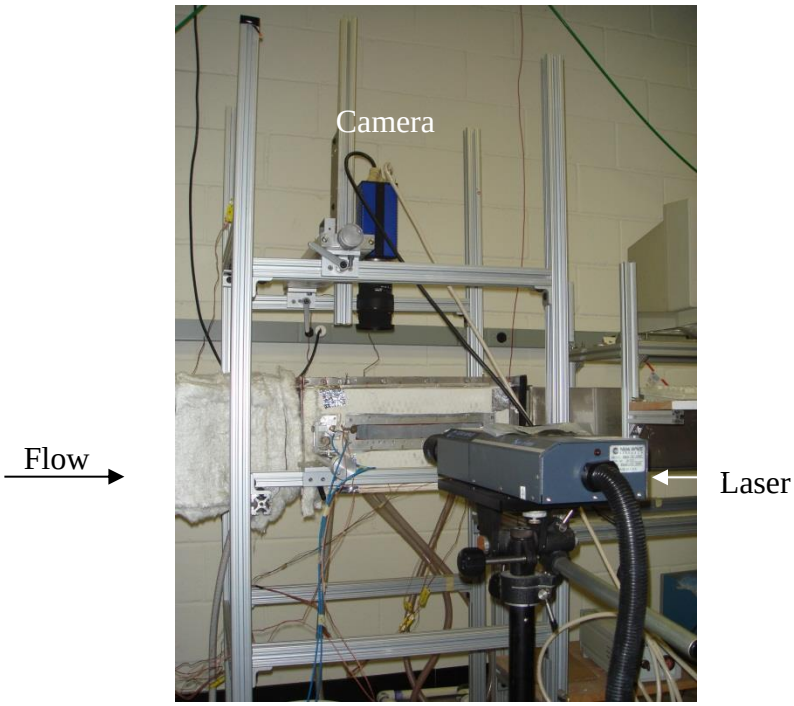

Figure 10. PIV setup in UMD Hot Wind Tunnel

2.2.2 Wall location and data truncation

Resolving data as close as possible to the wall is very important as wall temperatures and heat transfer are governed by gradients at the wall. Additionally, modelers often have to employ very fine grids at the wall in order to capture flow

physics faithfully. This grid refinement is associated with higher computational costs. Experimental data that can be used to develop wall models and forego wall refinement can be of great value to the research community. However, obtaining this type of near-wall data is very challenging for a variety of reasons.

One of the largest uncertainties in near-wall PIV is accurately determining the wall location. While careful calibration helps to minimize this uncertainty, several factors contribute to an observable difference between the wall location during calibration and during actual PIV recordings. Due to the fact that the laser sheet has a finite thickness (on the order of 1 mm) and that the camera is sensitive to perspective effects, the laser sheet interaction with the wall is actually observed as a thin strip of high intensity data. Figure 11 shows the 3-D laser sheet interaction with the wall as well as the resulting 2-D recording. Essentially, while both the front and back faces of the laser sheet volume are effectively interacting with the wall and both have a real y-location y = 0, the 2-D image shows an ~ 8 pixel thick strip as if the front and back of the laser sheet had 2 different y-coordinates.

Since this region is noise dominated and any seeding particles present will not be detected, one can assume that an effective wall-location corresponds to the *top* of the 2-D laser strip (corresponding to the back face of the laser sheet). Fixing this as y = 0 provides a good estimate of the actual y-location for the PIV results, since any signal obtained below this location will not contribute to any valid data.

Due to the image processing algorithm, the initial window size in the near wall region will encompass both particles and wall noise, and the wall noise will largely dominate. As a result, cross correlation results in this region are not valid, but

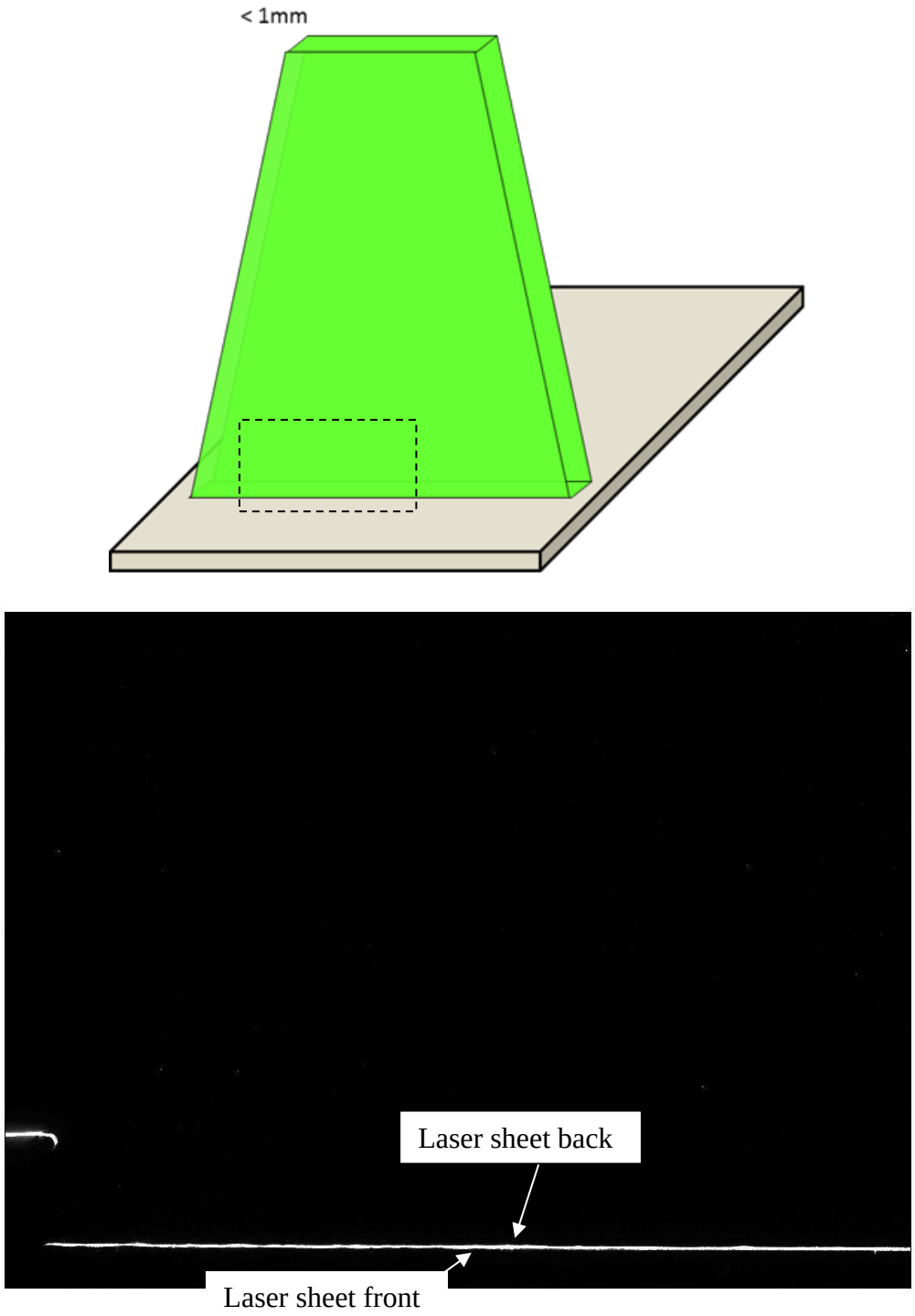

Figure 11 . Perspective effect on laser sheet/wall interaction

determining the extent of this region is not trivial. One can, however, look at the nature of the correlations in this region, particularly the correlation distribution, and realize that in noise dominated regions, the displacement-velocity obtained by the

algorithm has a distinct distribution shape, whereas regions without wall influence have a considerably different distribution. This information can then be used to remove invalid data points from the data set.

In noise dominated regions, the velocity distribution is very narrow, centered at a value of 0, and has characteristically less realizations (that is, the PIV algorithm itself has been able to determine that the correlation has indeed failed and has thus filtered out the result). In this region it is often found that only 100-200 out of the total 500 images provide a detectable although invalid particle displacement. As one moves away from the wall, one notices that the distribution spreads, the characteristic peak at u = 0 m/s decreases, and more realizations are detected. There is an overlap region where, although the distribution has a new shape, it still retains a small peak near u = 0 m/s (bimodal distribution). In this region, one can indeed expect valid realizations around this value, but it is impossible to discern which are valid and which are still artifacts of near-wall contamination. Thus, the first valid data point is chosen to be that one which exhibits a significantly different shape from that of the points below it, has no bimodal distribution, and has > 50% realizations. Figure 12 shows a series of distributions and their features starting with a wall dominated distribution, followed by an overlap region and finally the distribution corresponding to the first valid data point. While variable, most first valid data points were determined to be located at approximately 0.5 mm from the wall. This analysis was applied to all the velocity profiles reported in this work, and can easily be extended to any other profiles extracted from our data set. Furthermore, it can readily be applied to any near wall PIV data set as long as it meets statistical criteria similar to that

under which it was derived (namely that the data set is statistically large to observe mean and RMS convergence).

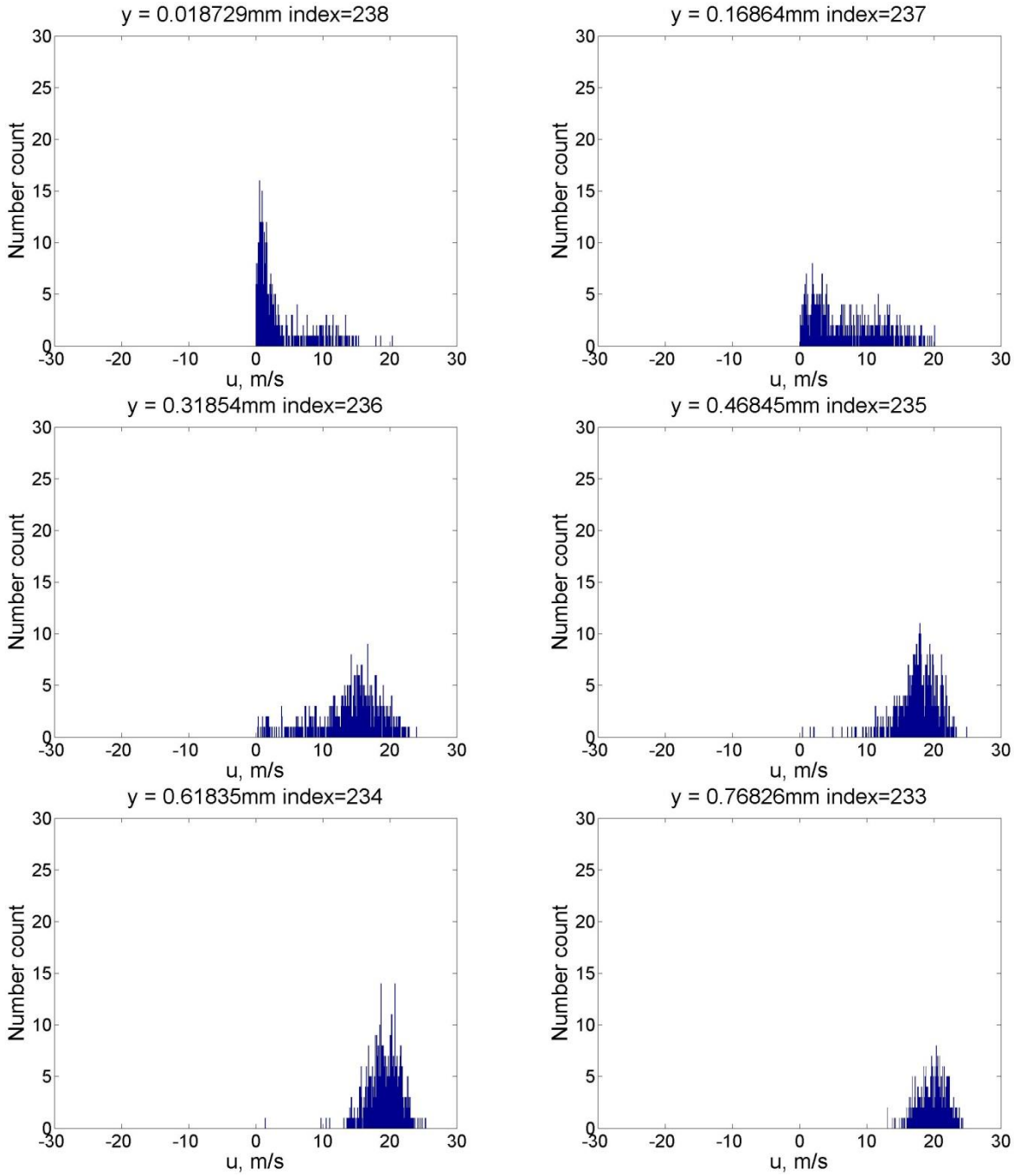

Figure 12. PDF of PIV realizations as a function of distance from the wall.

2.2.3 Reynolds decomposition

Given that all of the calculated vector fields exhibit mean and RMS convergence, one can apply Reynolds decomposition as a first order analysis to identify coherent flow structures in the flow. These structures are relevant, as they are responsible for the large scale mixing of the two streams, and their behavior determines how the film will eventually decay. Traditionally, Reynolds decomposition has been the de facto standard for turbulent flow decomposition (Adrian et al. [46]). The procedure consists in taking a time average of any turbulent flow property (in this case, the velocity components). The sampling time should be such that convergence in the mean is achieved. The time average is defined as

$$\overline{U} = \frac{1}{T}\int_0^T U dt \tag{17}$$

Subsequently, the time averaged value is subtracted from the instantaneous realizations to obtain the so called turbulent fluctuations. In the case of 2-D velocity components, this is expressed as

$$\begin{aligned} u' &= U - \overline{U} \\ v' &= V - \overline{V} \end{aligned}, \tag{18}$$

where U,V are the instantaneous velocity components at any given location, $\overline{U},\overline{V}$ are the time averages of said components and u',v' are the instantaneous turbulent fluctuations (Pope [41]). Figure 13 shows a sample velocity signal from a turbulent film cooling flow. The mean velocity is highlighted and the deviations from the mean are the instantaneous fluctuations.

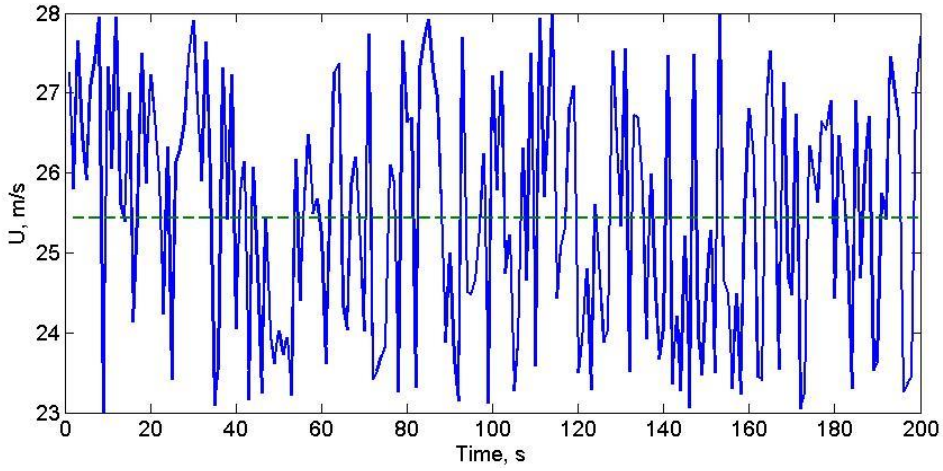

Figure 13 . Turbulent velocity signal and resulting time average (---)

Reynolds decomposition is very important in CFD modeling, as it is the basis of one of the most used methods in the community: RANS modeling. In this approach, the Navier-Stokes equations are time averaged such that each instantaneous flow quantity (velocity, temperature, density, etc) is effectively separated into its time average and a turbulent fluctuation. It can be shown (Kays and Crawford [46]) and is a common fluid mechanics coursework exercise that the resulting momentum RANS equations after decomposition are (in tensor notation)

$$\frac{\partial}{\partial x_j}\left(\rho \bar{u}_i \bar{u}_j\right) = -\frac{\partial P}{\partial x_i} + \frac{\partial}{\partial x_j}\left(\bar{\tau}_{ji} - \rho \overline{u_i' u_j'}\right) \tag{19}$$

where the term $\left(\rho \overline{u_i' u_j'}\right)$ is commonly known as the Reynolds stress tensor.

RANS simulations work by using a model for the Reynolds stress terms (many models exist) while solving for the remaining variables explicitly (Kays and Crawford [47]). As such, any RANS model development will benefit from having experimental information related to the Reynolds stresses either as an input to verify the stress model or for validation of the results. Because of its importance in the CFD

community (and current modeling work at NASA directly related to this dissertation is essentially RANS based), Reynolds decomposition of the velocity data was performed to obtain additional information of interest to the CFD developers involved in the project, particularly profiles of u_{rms}, v_{rms} and $\left(\overline{u'v'}\right)$.

Reynolds decomposition is not only useful for CFD development. Adrian et al. [46] have shown that Reynolds decomposition is a useful approach to revealing coherent structures in turbulent flows. The authors suggest that Reynolds decomposed fields tend to reveal more vortices than Galilean decompositions, and as such Reynolds decomposition is the more traditional approach. Additionally, Reynolds decomposition tends to reveal more of the small scale vortices than other approaches. A downside of the approach is that large scales may be lost as these are typically associated with the mean flow which is subtracted.

Nevertheless, Reynolds decomposition allows for the qualitative and quantitative visualization of coherent structures in the flow. Vortices can be visually identified based on the sign of the fluctuations. Since vortices are characteristically regions of rotation, they will show as regions of alternating fluctuations (i.e. $v' > 0$ next to a region of $v' < 0$). The preferred rotation direction of these structures can also be observed.

Yet another use of Reynolds decomposition is to use the resulting fluctuations to calculate the so called correlation coefficient as a measure of coherence in the flow. Given a fixed reference location in the 2-D field $\vec{x} = x_0\hat{i} + y_0\hat{j}$ one can define a correlation coefficient R_{ij} as (Wallace and Bernard [48])

$$R_{ij} = \frac{\overline{u'_i(\vec{x},t)u'_j(\vec{x}+\vec{r},t)}}{\overline{u'_i(\vec{x},t)u'_j(\vec{x},t)}} \tag{20}$$

In this case, the subscripts *i, j* denote the velocity component in question with *u, v, w* corresponding to 1,2,3. For example, R_{12} becomes

$$R_{12} = \frac{\overline{u'_1(\vec{x},t)u'_2(\vec{x}+\vec{r},t)}}{\overline{u'_1(\vec{x},t)u'_2(\vec{x},t)}} = \frac{\overline{u'(\vec{x},t)v'(\vec{x}+\vec{r},t)}}{\overline{u'(\vec{x},t)v'(\vec{x},t)}} \tag{21}$$

The value of these correlations lies in providing some insight about the integral lengthscales of the flow as well as revealing some interesting features about the structures. One can define a coherent lengthscale as the integral of the correlation along a fixed direction. For example, if one measures the correlation only along the x-axis (aligned in the direction of unit vector $\hat{i}$), such that

$$R_{ij} = \frac{\overline{u'_i(\vec{x},t)u'_j(\vec{x}+a\hat{i},t)}}{\overline{u'_i(\vec{x},t)u'_j(\vec{x},t)}} \tag{22}$$

then one can define an integral coherent lengthscale as

$$L_{ij},x = \int_0^\infty R_{ij}\,dx \tag{23}$$

There is no reason why the coherent lengthscale has to be aligned with either the axial or wall-normal directions or for the lengthscales to even be the same, i.e. $L_{11,x} \neq L_{22,x} \neq L_{22,y}$ (Bradshaw [49]). An elliptical correlation for example can have $L_{ij,x} > L_{ij,y}$, while an inclined structure can essentially have a lengthscale that does not correspond to either $L_{ij,x}$ *or* $L_{ij,y}$. Figure 13 shows an example of R_{22} measured along the x axis in a turbulent boundary layer.

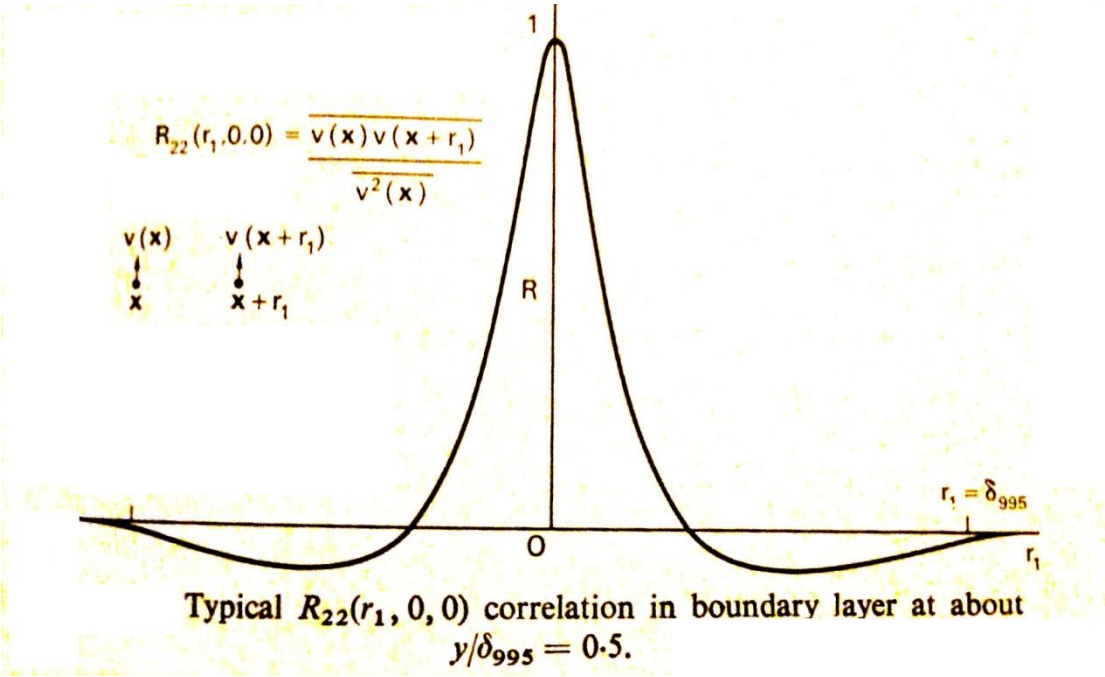

Figure 14. Representative correlation plot ($R_{22,x}$) for a turbulent boundary layer [49].

Traditionally, these correlations gave very limited information due to the nature of the measurements. One probe had to be fixed at the desired reference location while another probe was moved either in the x or y direction while capturing the data. In effect, this reduced the correlation to treat $\vec{r}$ as a 1-D vector in either x or y. Very few points could be obtained, and the correlation essentially became a 1-D profile that could only reveal information along one axis, either $L_{ij,x}$ *or* $L_{ij,y}$, and so some information could be missed, particularly regarding the possible inclination of the correlation (Bradshaw [49]). Taking advantage of the global characteristics of PIV, the correlation coefficient can be truly calculated as 2-D contours and virtually any point in the velocity field can be used as the reference after capturing the data. This provides us with the capability of performing any correlation R_{ij} for any reference coordinate (x_0,y_0) and obtain the true 2-D shape of the correlation with good

spatial resolution. Furthermore, since the correlation relies on a time average of the products of the fluctuations, the same approach can be applied to time resolved CFD simulations such as LES. This provides another layer of comparison that can be of use to model developers.

For the purpose of this work, several locations were used as reference points (x_0,y_0). x-locations were chosen to match the location of the thermal measurements and extracted velocity profiles, while y locations were chosen as y/s = 0.5, 1.0 and 2.0 corresponding to locations in the slot (close to the wall), at the lip and in the mixing layer (far from the wall). While one could theoretically correlate each reference with each remaining point in the vector field, this would be an intense computational effort. A priori runs determined that correlating the reference point at the center with its 48 x 48 neighboring points in the grid provided enough information. For each case, all possible correlations were calculated although the most important ones are the *u'u'* and *v'v'* (R_{11} and R_{22}) as these are the ones that are most suited for estimates of the x and y direction integral lengthscales (L_x, L_y). The results showed that, in general $L_{11,x} > L_{11,y}$ while $L_{22,x} < L_{22,y.}$ $L_{11,x}$ was on the order of half of a slot height near-injection, growing downstream for all cases. Figure 15 shows the R_{22} results of this exercise for a wall-wake type flow, where one can observe how $L_{22,x}$ grows downstream, while $L_{22,y}$ grows away from the wall.

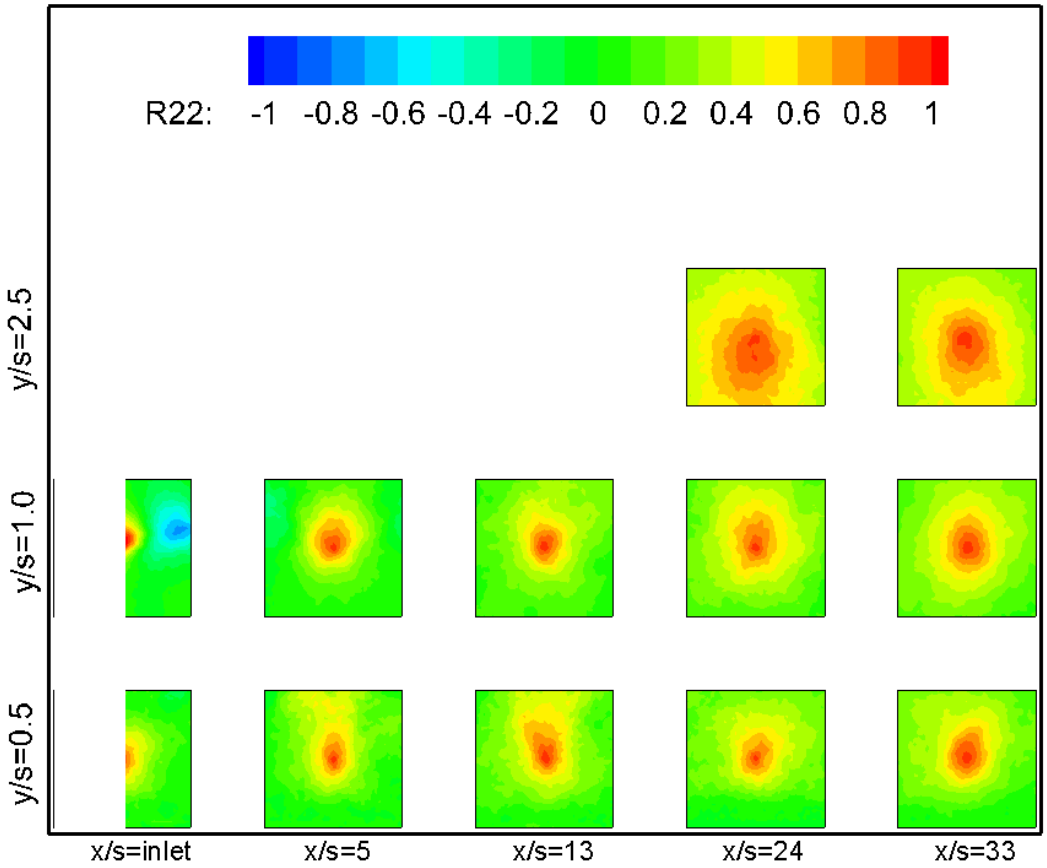

Figure 15 . Contours of R_{22} for the wall-wake case. At the inlet and at the louver (y/s =1.0) a very strong negative correlation suggests the constant presence of roller type structures. Downstream, the overall coherence length grows with downstream distance as well as with wall-normal distance.

2.2.4 Coherent structure detection

One of the characteristics of turbulent flows, particularly those associated with shear layers is the presence of so called coherent structures (eddies or vortices). These structures can provide important information about the flow if one can quantify them (location, size, strength). Additionally, comparing experimentally detected coherent structures to those from numerical simulations (such as those from Large Eddy Simulations (LES) or Direct Numerical Simulations (DNS)) provides an important layer of comparison that goes beyond mean and first order turbulence data.

Comparing the location, size and strength of these eddies can provide a modeler with important spatial information that cannot be obtained by comparing profiles alone.

Adrian et al. [46] have provided a good summary of various methods which can be applied to a velocity field in order to characterize such structures. One of the common challenges encountered with identifying coherent structures is the lack of a widely accepted definition regarding what constitutes a vortex. Despite the varying definitions of a vortex in the literature (Chong et al. [50], Jeong and Hussain [51], among many others), any choice of detection method is valid as long as it can provide meaningful results. In the context of the present work, the method of choice should be readily applicable to PIV data as well as to time resolved CFD (LES or DNS) in order to provide a direct comparison between experiments and modelling.

Gradient based detection methods have been described in the literature (Chakraborty et al. [52]) where vortex cores are defined as functions of the velocity gradient tensor. Among these methods, the Q-criterion [53] and the λ_2-criterion [51] are some of the most commonly used. Given a 3-D velocity field, with Cartesian components (u, v, w) the velocity gradient tensor is defined as

$$\nabla \vec{V} = \begin{bmatrix} \frac{\partial u}{\partial x} & \frac{\partial u}{\partial y} & \frac{\partial u}{\partial z} \\ \frac{\partial v}{\partial x} & \frac{\partial v}{\partial y} & \frac{\partial v}{\partial z} \\ \frac{\partial w}{\partial x} & \frac{\partial w}{\partial y} & \frac{\partial w}{\partial z} \end{bmatrix} \tag{24}$$

Furthermore, the tensor can be separated into the symmetric and antisymmetric parts S_{ij} and Ω_{ij} respectively. S_{ij} is typically known as the rate of strain tensor, while Ω_{ij} is known as the rate of rotation tensor. A scalar quantity Q can be defined as

$$Q = \frac{1}{2}\left(\left\|\Omega_{ij}\right\|^2 - \left\|S_{ij}\right\|^2\right) \tag{25}$$

The Q-criterion then establishes that a vortex core will exist in regions where vorticity is greater than strain, therefore Q > 0 inside a vortex core.

The λ_2 method looks for the eigenvalues of the tensor $S_{ij}^2 + \Omega_{ij}^2$. Ordered in increasing value such that $\lambda_1 < \lambda_2 < \lambda_3$, a vortex core will exist if $\lambda_2 < 0$. These methods have been defined for 3-D velocity fields as well as for incompressible flows. Extensions to compressible flows or variable density flows can be made, but the methods may fail under certain circumstances or these effects must be accounted for, increasing the complexity of implementing the method. Similarly, lack of information for one of the velocity components (as is the case with 2-D PIV) requires the use of a modified 2-D method which may also yield unrealistic results. Because of their reliance on velocity gradients, these methods usually require good spatial resolution in order to accurately calculate the velocity gradients. Additionally, methods such as the Q-criterion may be sensitive to vorticity type (Burgers [54] vs. Rankine [55]) and the relationship between vorticity magnitude and vortex size. For example, it has been shown that for Burgers type vortices, if the vortex Reynolds number falls below a certain threshold then Q < 0 everywhere inside the vortex core and the method will fail to detect a vortex [52].

While these methods can be applied to PIV data, it is expected that typical PIV spatial resolution may not be adequate enough to calculate velocity gradients accurately or that the vorticity encountered may be such that the Q-criterion will fail to identify vortex cores. The Q-criterion may also be affected by variable density, as

this slightly changes the definition of the rate of strain tensor and requires a more complicated evaluation of the criterion, as explained earlier.

To explore the usefulness of one such method, an artificial vortex of user-defined dimensions, strength and vorticity type has been generated using a commonly available Matlab toolbox (PIVMat). A 2-D vortex with 'Rankine' type vorticity (the vortex exhibits solid body rotation type vorticity), diameter = 6 mm (on the order of a slot height of the flow), and a spatial resolution of ~7vectors/mm was superimposed on a constant 2-D velocity field (u = 15 m/s, v = 1 m/s) to simulate an instantaneous PIV measurement on the order of those obtained for the current work. Additionally, the spatial resolution was reduced by a factor of 2 down to ~0.25 vectors/mm to explore the sensitivity of the method to spatial resolution.

The Q-criterion was applied to these identical vortices (other than their spatial resolution) and the results are plotted in Figure 16. The vortex core has been analyzed with Matlab in order to characterize the diameter of the detected structure. As one can see, under ideal conditions, the Q-criterion works reasonably well, detecting the vortex in every iteration and the detected structure size matches the prescribed size very well for resolutions > 3 vectors/mm. A noticeable impact on vortex size calculation is observed at low spatial resolutions. It is expected that vortices in the current work may be found on a varying range of sizes, and the vorticity distribution may not be as well defined as in the test case. Application of the Q-criterion method to actual PIV data from this work is shown in Figure 17. While one can see that the method is able to detect regions where Q > 0, the vortex cores seem unreasonably small (on the order of 0.2 mm or 1/30 of a slot height).

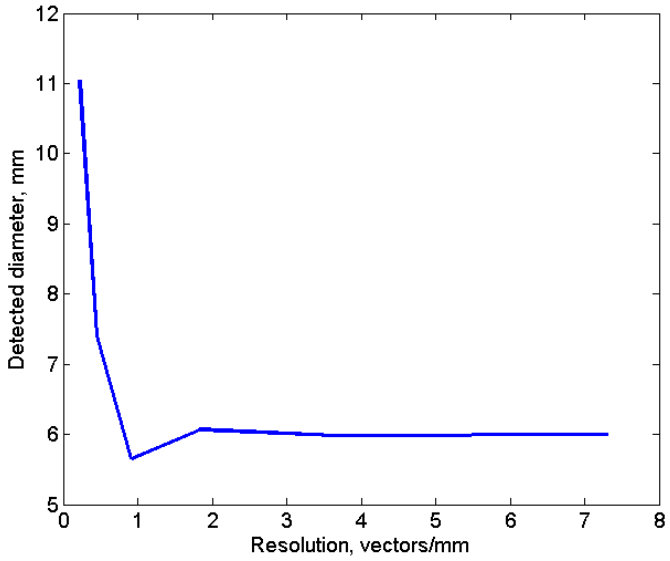

Figure 16. Impact of spatial resolution of velocity field on diameter of detected structure using Q-criterion.

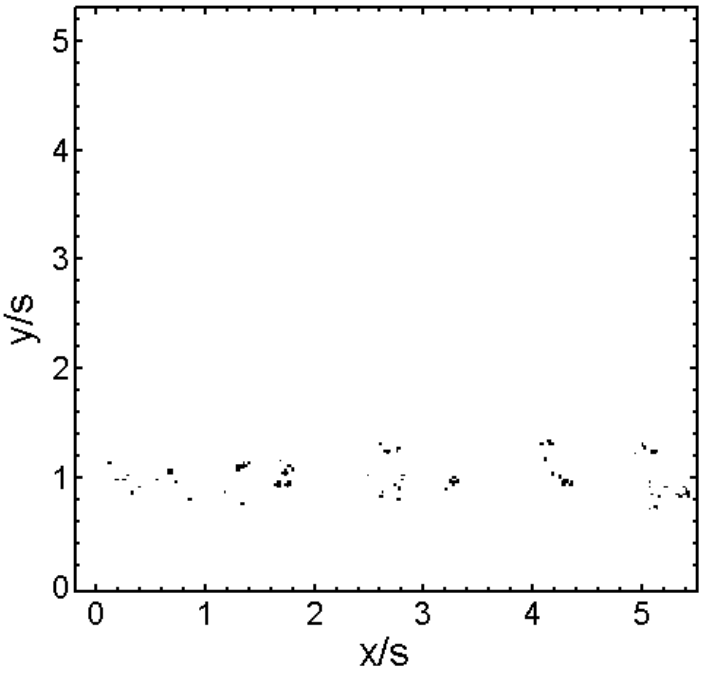

Figure 17. Q-criterion applied to an actual PIV data field from the current work.

An alternative method based on vortex topology (not gradient based) has been proposed by Graftieaux et al. [54]. In this method, a vortex core is defined as a region

where motion closely resembles that of solid body rotation about a central point. For any point P in the velocity field, one can measure how the velocity vectors behave around said point and compare their behavior to those of ideal solid body rotation. Let S be an arbitrary area around P. Let M be any point inside S other than P. Let **U** be the 2-D velocity vector at point M. Let θ_M be the angle between the direction vector defined by PM and **U** (see Figure 18). A vortex identification function can be defined as

$$\Gamma_{ID}(P) = \frac{1}{S}\int_S \sin(\theta_M)\,dS \tag{26}$$

and said function can be calculated at every point P in the velocity field. The sign of the function identifies the direction of rotation, while the magnitude identifies the similarity between the observation and true solid body rotation. If the velocity vectors behave as an ideal vortex (perfect solid body rotation), then Γ_{ID} = +/-1 at the vortex center, with positive values indicating counter-clockwise rotation, and negative values indicating clockwise rotation. According to the work of Graftieaux et al. [54] for $|\Gamma_{ID}| \geq 0.6$ the existence of a vortex core can be claimed. Deviations from ideal solid body rotation will typically result in regions where $|\Gamma_{ID}| \geq 0.6$, but never equal to unity.

For velocity fields where coherent structures are "hidden" by the dominating convection of the flow (as is the case of the current work), the vortices must first be obtained by spatial averaging. This averaging requires the a priori identification of the spatial scale that must be used for the averaging procedure. Once an averaging scale $L_{average}$ has been chosen, a window of size $L_{average}$ x $L_{average,}$ is drawn around every

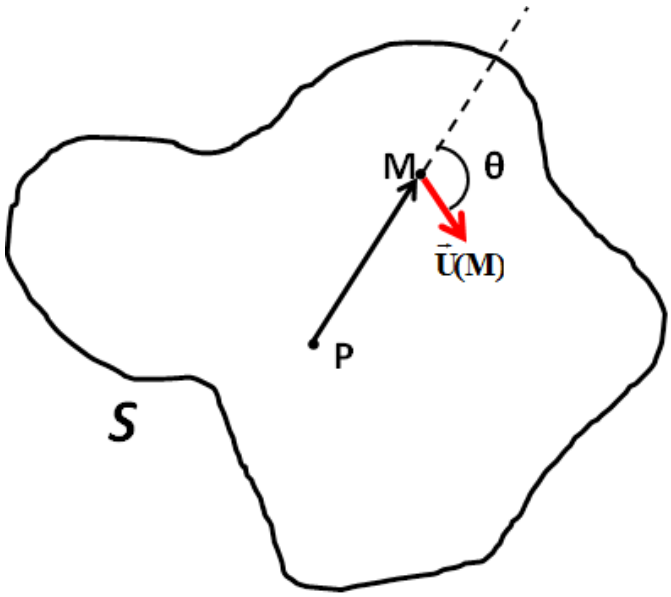

Figure 18. Geometry for the calculation of the vortex ID function of Grafiteaux et al. [54].

point in the original PIV field except for those points where the corresponding window would lie outside the original domain (around the edges of the PIV field). For every window, the spatial average of the velocity, $<\vec{U}(x,y)>$ within the window is obtained and assigned to the corresponding point P_{center} (the use of < > denotes spatial averaging in this instance). The field is then decomposed as

$$\vec{U}(x,y) = <\vec{U}(x,y)> + \vec{u}''(x,y) \tag{27}$$

which is similar to Reynolds decomposition except that the average velocity field has been obtained by spatial averaging over the window of choice and not in time at a specific (x,y) location.

The resulting fluctuation field $\vec{u}''(x,y)$ is used in the definition of θ_M, where θ_M now represents the angle between the direction vector PM and $\vec{u}''$ at point M. In this case, the region *S* is effectively the window around $P_{center.}$ Coherent structures are

determined as regions where $|\Gamma_{ID}| \geq 0.6$. Using image recognition functions from Matlab's image processing toolbox, these regions can be easily identified. Vortex centroids are identified as regions of local maxima of $|\Gamma_{ID}|$ and further information about identified structures can be quantified, such as rotation direction, area, perimeter, and equivalent diameter (the diameter of a structure of equal area with perfectly circular shape). For each detected structure, this information can be further used to obtain the velocity at the centroid, $< \vec{U}(x_{centroid}, y_{centroid}) >$, which is effectively the convective velocity of said structure. Using the fluctuating x and y-components of velocity, u'' and v'' a 2-D turbulent kinetic energy parameter defined as $(u''^2+v''^2)$ can be calculated at each point inside the identified structure. The strength of the structure can be quantified as the mean energy enclosed by the entire structure (i.e. averaged over the region). The calculated strength can also be normalized by the area of the structure to provide another level of comparison.

For every velocity field, all of this information is stored in a database such that statistics about the total number of structures can be calculated. In the context of this work, only the 500 PIV velocity fields corresponding to the near-inlet location were used for all cases. The database can be filtered by any search parameter in order to reveal different aspects of the data for insight. A Matlab code based on the work of Lind and Jones [57] was used to apply the method to the PIV data and obtain the coherent structures, while a fully customized code was written for the calculation of relevant data (centroid, strength, etc.) as well as for querying the database based on user prescribed filters.

Another advantage of this method is that it can be readily applicable to LES simulations. As long as the same spatial scale is used to average the experimental and simulated velocity fields, the comparison can be performed without introducing unwanted errors. While the method is somewhat sensitive to the choice of $L_{average}$, the current work will assume an averaging scale of one slot height for all the fields investigated based on the coherent lengthscales identified by Reynolds decomposition. Figure 19 shows the result of applying this method to a representative PIV data field from the current work (same data used in Figure 17.)

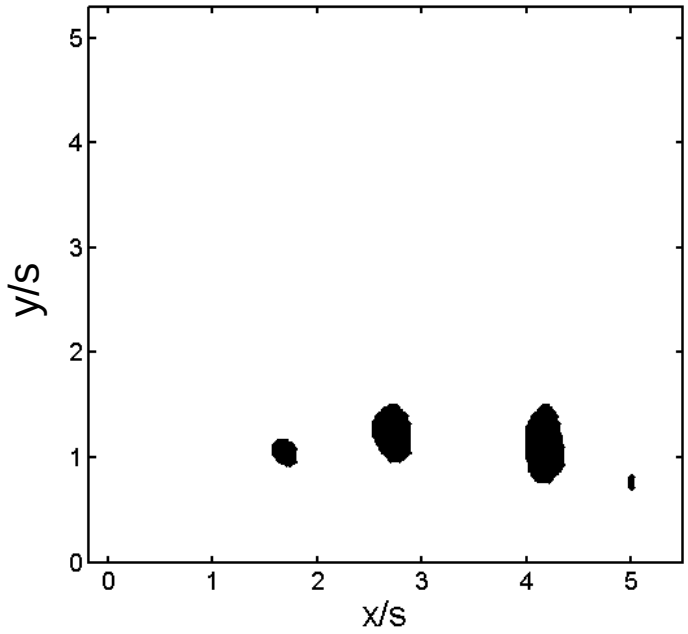

Figure 19. Vortex ID method applied to same PIV data field as in Figure 17. Black regions correspond to identified vortex cores.

2.2.5 Law of the Wall analysis

As discussed earlier, identifying near-wall models from experimental data can be of great value for modelers in order to relax the fine grid requirements of CFD simulations near the wall. In the classical turbulent flow literature, it is widely accepted that turbulent boundary layers (external and internal) follow the so called

law of the wall, first proposed by von Kármán [58]. This law states that any turbulent boundary layer exhibits the same characteristic velocity profile after a particular normalization of flow parameters. At any location along the wall, the local shear stress at the wall is denoted τ_w. One can define a shear velocity as

$$u_\tau = \sqrt{\frac{\tau_w}{\rho}} \tag{28}$$

The flow velocities can then be normalized by the shear velocity

$$\begin{aligned} u^+ &= u / u_\tau \\ v^+ &= v / u_\tau \end{aligned} \tag{29}$$

The geometric coordinates can also be normalized by the shear velocity into so called wall units defined as

$$\begin{aligned} x^+ &= \frac{x u_\tau}{\nu} \\ y^+ &= \frac{y u_\tau}{\nu} \end{aligned} \tag{30}$$

The law of the wall describes the behavior of u^+ as a function of y^+. Very close to the wall, there is a viscous sub-layer where viscous effects are dominant and as a result, the velocity profile is perfectly linear such that $u^+ = y^+$. Following this region, there is a characteristic transition region in which the velocity profile abandons this linearity to approach a logarithmic behavior. In this logarithmic region, the relationship is of the form

$$u^+ = \frac{1}{k_1} \ln y^+ + k_2 \tag{31}$$

Far enough from the wall, the velocity profile departs from the logarithmic region in the so called wake region. It has been shown that while the law of the wall does not

provide universal collapse for all possible turbulent velocity profiles, any turbulent velocity profile will exhibit this general behavior. Differences that may arise among turbulent boundary layers are typically the relative lengths of each region in y^+ space as well as the y^+ location of the final departure from the logarithmic region. For example, accelerating and decelerating layers have been shown to diverge from the logarithmic region in opposite directions, while the relative lengths of the layers have been shown to have a Reynolds number dependence. Regardless of these differences, it is widely accepted that all turbulent boundary layers of the same family follow the same logarithmic behavior (i.e the constants k_1 and k_2 are well known). Furthermore, turbulent boundary layers will always follow a linear-log law behavior whereas it is impossible for a laminar layer to do so. Figure 20 shows the law of the wall for a turbulent external boundary layer.

In film cooling, however, it is not trivial to determine whether or not the law of the wall applies, and if so, which form will it follow (external vs. internal, accelerating vs. decelerating freestream), for it is not a classical turbulent boundary layer. For example, the fact that there is a mixing layer above the wall makes it somewhat difficult to determine what the freestream velocity of choice should be. One may see from the wall variables that this functional form is not required a priori as long as one can directly measure the shear stress at the wall. In doing so, one can readily calculate the shear velocity and obtain u^+ and y^+ allowing one to plot the velocity profile accordingly and proceed with the analysis. However, measuring the shear stress at the wall is quite a challenging task that few researchers have been able to obtain without sacrificing something in the process. In the case of this work, the

only possible way of obtaining the shear stress at the wall is by calculating the velocity gradient, *du/dy*, at the wall. This requires not only having valid data points very close to the wall, but also a very fine near-wall resolution since this gradient must be determined by a finite difference scheme.

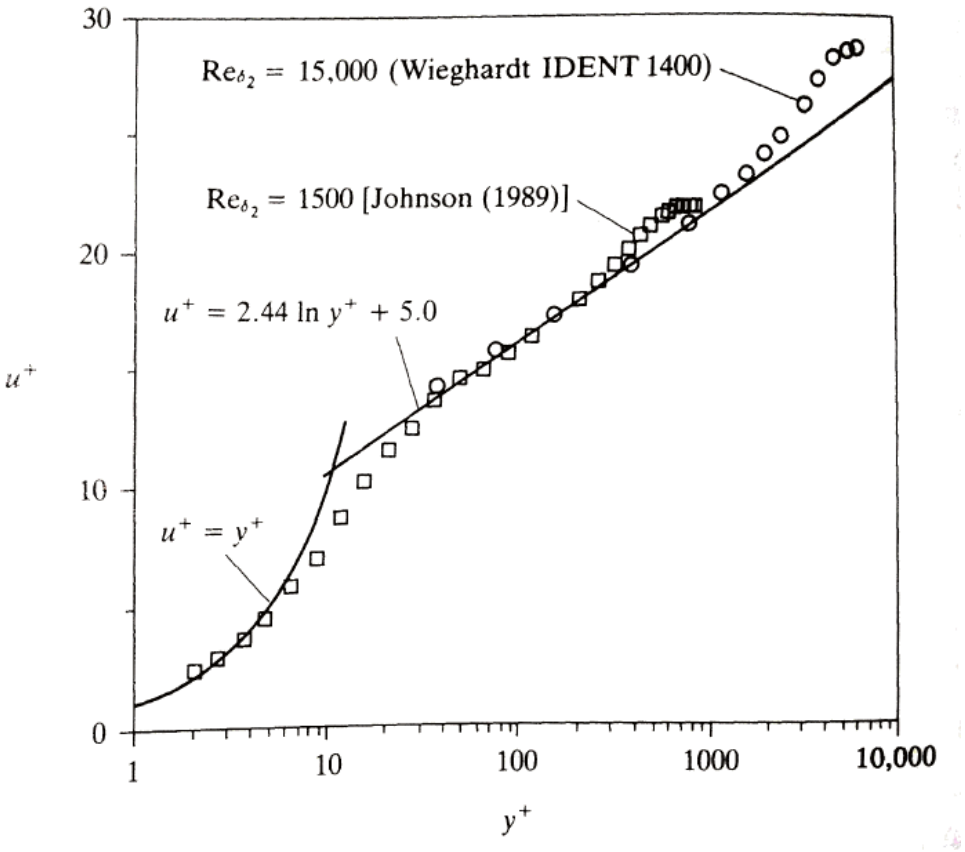

Figure 20 . Law of the wall and experimental data (Kays and Crawford [47])

Unfortunately, while the first valid near wall points obtained from PIV are relatively close to the wall, they are not close enough to allow for direct measurement of the gradient. In order to do so, the slot height must have to be significantly larger (effectively stretching the velocity profile in the y-direction), which is a compromise that was not affordable.

A workaround to address this issue was suggested by Clauser [59] which works on the principle that turbulent boundary layers follow a log-law sufficiently away from the wall (essentially, invoking the law of the wall). Instead of measuring or estimating the shear velocity to plot u^+ vs. y^+ and obtaining the characteristics of the logarithmic region, one can choose the functional form of this logarithmic region *a priori*, extrapolate the existing data onto this functional form as a data fit and then obtain the shear velocity. It is an elegant solution that, however, relies heavily on the chosen form of the log-linear region. If one chooses erroneously, then one will adequately fit the data to the wrong function and the resulting shear velocity will be undoubtedly wrong.

Film cooling data was first analyzed using artificial values of the shear velocity to calculate u^+ and y^+. These were subsequently plotted as a family of curves, all of which exhibited a linear-log region. With the obtained data, the strongest claim one can make without further assumptions is that, regardless of the choice of shear velocity, the data does indeed exhibit a log-law behavior. This provides a certain degree of confidence that the Clauser method may be applied to the data to further investigate it.

Given that data showed linear-log behavior, the Clauser method was attempted on the experimental data. The approach was first tested on film cooling RANS simulations performed by Voegele [35] in order to identify how well the method could capture the shear velocity in film cooling flows. The test criteria was as follows:

1. Obtain a ***film cooling*** simulation of acceptable performance in capturing the kinematics (i.e. compare the simulation results to the experimental mean and RMS velocity profiles. Results should match qualitatively in capturing the overall profile shapes, and quantitatively within 15%)
2. Investigate the near wall resolution of said simulation to verify that it is better than that of the experiments.
3. Measure the velocity gradient *du/dy* at the wall directly using simulation data, calculate the shear velocity and the wall variables and obtain a plot of u^+ vs. y^+. Compare to the known law of the wall.
4. In parallel, apply the Clauser method to the simulation velocity data assuming a known function for the law of the wall. Plot this data and recover the value of the shear velocity that fits the experimental data to the law of the wall.
5. Compare the shear velocity from step 3 to that of step 4.

The results of this test are summarized in Table 3 which shows that the Clauser method can provide a very good estimate of the shear velocity, and thus the shear stress at the wall. For experimental data analysis, a classical law of the wall over a flat plate was used as the log-linear function for all cases (equation 31) with $k_1 = 0.41$, $k_2 = 5.0$. However, it should be noted that the law of the wall for flow over a backward facing step has been shown to be of a different form, particularly very close to the step (Le, Moin, Kim, Armaly [60-62]). Given that the wall-wake is very similar to this type of flow, the wall-wake data was tested against the law of the wall for backward facing steps as well.

Table 3. Comparison of shear velocity calculations on CFD data by Voegele [35] by direct gradient and Clauser method.

Wall Jet			
x/s	**Uτ direct gradient CFD (m/s)**	**Uτ Clauser CFD (m/s)**	**% Difference**
0.49	1.18	1.25	5.93
5.28	1.16	1.20	3.45
13.65	1.11	1.13	1.80
25.62	1.02	1.03	0.98
35.27	0.96	0.97	1.04
Min Shear			
0.46	1.05	1.13	7.62
4.89	1.08	1.09	0.93
12.67	1.04	1.05	0.96
23.81	0.99	1.02	3.03
32.74	0.96	0.96	0.00
Wall Wake			
0.47	0.61	0.74	21.31
4.64	0.69	0.70	1.45
11.98	0.67	0.67	0.00
22.46	0.69	0.68	1.45
30.85	0.85	0.77	9.41

Overall, this test provides some confidence that the Clauser method (with the appropriate and non-trivial log-linear function choice) can indeed be applied to the experimental data not only to provide insight but also as yet another important layer of comparison between CFD and experimental data to validate the simulation results. Ultimately, film cooling is a complex phenomenon designed to alter the heat transfer to a surface, effectively reducing its temperature. Since heat transfer is dominated by wall gradients it is paramount that both the experimental velocity and thermal gradients are well captured by CFD simulations. In the absence of very near-wall resolved measurements, the Clauser method provides a 1st order approach to validating kinematic gradients between experiments and CFD. Additionally, it

suggests that near-wall models based on the law of the wall are worth exploring in order to obtain film cooling relevant wall models for use in CFD models in lieu of fine grids.

2.2.6 Microthermocouples

In addition to kinematic measurements, it was of equal importance to adequately capture the thermal behavior of the flows in question to fully address the film cooling physics under realistic conditions. In order to obtain flow temperature profiles, it was necessary to obtain a fast response measurement with negligible contamination from radiation or other sources of error. It was also ideal to use a probe that would disturb the flow as little as possible.

Like PIV, a few techniques allow for the global measurement of flow temperatures (Planar Laser Induced Fluorescence, for example). However, most of these techniques are complicated to implement and do not provide enough temporal information. While sacrificing the global aspect of the measurement in exchange for high temporal resolution and low radiation contamination, microthermocouples were chosen.

2.2.6.1 Microthermocouple probe characteristics and measurement criteria

Probes were built using small diameter stainless steel tubes, a ceramic insert and a 13 μm diameter wire K-type thermocouple with the bead protruding on one end. Figure 21 shows a detailed sketch of the probe.

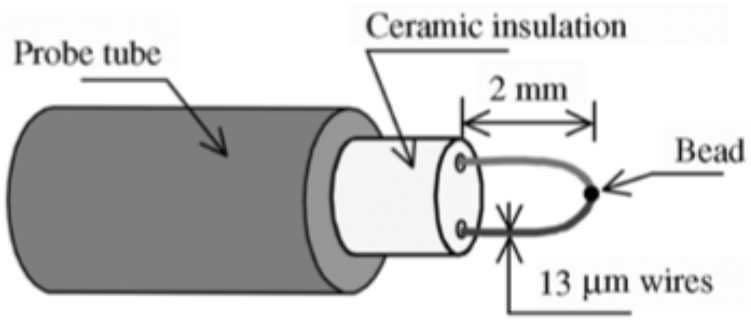

Figure 21. Microthermocouple probe (adapted from Cruz and Marshall [16])

These probes were calibrated and connected to a National Instruments digital signal processing box. Labview® software was used to sample data at 10-20 kHz for 15 seconds. The high frequency ensures that the expected range of turbulent fluctuations is well captured, as the Nyquist sampling theorem allows one to resolve fluctuations up to 5-10 kHz. The sampling time is significantly longer than the characteristic residence time of the flow, estimated as the time required by an eddy of characteristic lengthscale $l = s$ to move through space at the convective velocity $U_{conv}=0.5(U_{\infty}+U_c)$ such that

$$t_{res} = \frac{s}{U_{conv}} \tag{32}$$

shows the residence times, t_{res} and associated frequencies, f_{res}, for each case, which are clearly smaller than the sampling time by 5 orders of magnitude. These calculations show that the temperature signal can be effectively thought of as the temperature history of a statistically large number of eddies passing through a fixed point in space.

Measurements were taken at 5 distinct spatial locations along the flow direction. While these locations were exactly the same for all cases, non-dimensionally they correspond to slightly different locations due to the variation in slot heights. The same locations were also used in the non-adiabatic cases. 15-25 data points were used for each profile, with a variable wall normal resolution. Near-wall resolution was on the order of 0.25 mm-0.5 mm and a similar resolution was used through the near injection mixing layer where sharp gradients were expected. As the shear layer grows downstream of injection and the gradients become less steep, the resolution was relaxed slightly. Nevertheless, special care was taken to ensure that the main features of the temperature profile were captured.

Table 4. Residence times of eddies of characteristic lengthscale $l = s$.

	Wall Jet	**Min Shear**	**Wall Wake**
U_{conv}, m/s	17.5	20.9	16.8
s, mm	5.3	5.7	6.1
t_{res}, s	3.0×10^{-4}	2.7×10^{-4}	3.6×10^{-4}
f_{res}, Hz	3330	3700	2780

2.2.6.2 Temperature data compensation

Data obtained using these microthermocouples had to be compensated for the thermal inertia of the bead. An energy balance on the bead shows that

$$\dot{E}_{storage} = \dot{E}_{convection} + \dot{E}_{conduction} + \dot{E}_{radiation} \tag{33}$$

Due to the small wire diameter, thermal insulation on the probe and the length of the exposed wire (2 mm) compared to the bead size (25 microns), the conduction term can be ignored as suggested by Blevins et al [63]. Assuming steady state (no storage), radiation is balanced by convection

$$h(T_g - T_b)A = \varepsilon_b \sigma (T_b^{\,4} - T_{surr}^4)A\,, \tag{34}$$

where h is the convective heat transfer coefficient, T_g is the gas temperature of the flow over the bead, T_b is the bead temperature, T_{sur} is the temperature of the surroundings (casing and windows), ε_b is the bead's emmisivity, σ = 5.6704×10^{-8} W/(m^{2}K^4) is the Steffan-Boltzmann constant, and A is the surface area of the bead. Solving for the temperature difference between gas and bead yields

$$(T_g - T_b) = \frac{\varepsilon_b \sigma}{h}(T_b{}^4 - T_{surr}^4). \tag{35}$$

Knowing the bead and casing temperatures from measurements, along with the bead emissivity (from knowledge of material properties) and heat transfer coefficient (from correlations based on flow velocities and temperatures) results in an estimated error ~ 0.25 K which is on the order of the inherent thermocouple error. Thus, radiation contamination on the thermocouple can be ignored [64].

With conduction and radiation shown to be negligible, the energy balance including unsteady effects reduces to $\dot{E}_{storage} = \dot{E}_{convection}$. The "storage" term is the net time rate of gain or loss of energy by the bead

$$\dot{E}_{storage} = mC_p \frac{dTb}{dt} \tag{36}$$

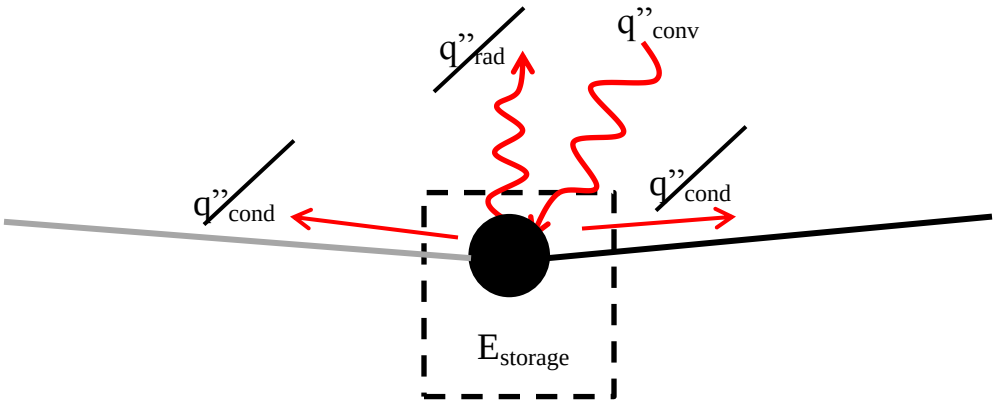

Figure 22. Energy balance on thermocouple bead

where m is the mass of the bead, C_p is the specific heat capacity of the bead, and dT_b/dt is the instantaneous time rate of change of the bead temperature, while the convection term can be expressed in the classical sense as

$$\dot{E}_{convection} = h(T_g - T_b)A \tag{37}$$

Because thermocouple measurements are actually bead temperatures, if one must recover the gas temperature, then one can rewrite the energy balance to solve for T_g, namely

$$mC_p \frac{dT_b}{dt} = h(T_g - T_b)A \tag{38}$$

and solving for T_g

$$T_g = T_b + \frac{mC_p}{hA}\frac{dT_b}{dt} \tag{39}$$

Equation 39 has been widely used in the open literature as a 1st order characterization of unsteady heat transfer in thermocouple compensation [65].

One can readily observe that this relationship is a first order differential equation of the form

$$\tau \frac{dy}{dt} + y(t) = f(t) \tag{40}$$

and thus, $\tau = (mC_p)/(hA)$. In this form, the equation resembles that of a linear time invariant system (Lipták [66]) where $y(t)$ is the output response to a forcing function input $f(t)$ and characterized by the time constant, τ. The homogenous solution of this differential equation is an exponential function

$$y_h(t) = Ae^{-t/\tau}. \tag{41}$$

Here, τ is physically interpreted as the time required for the system (thermocouple bead) to decay by a factor of *1/e* from its initial temperature value to its final value after a step change in temperature driven by a change in the gas temperature (forcing function). Figure 23 shows the time response of thermocouples of several diameters.

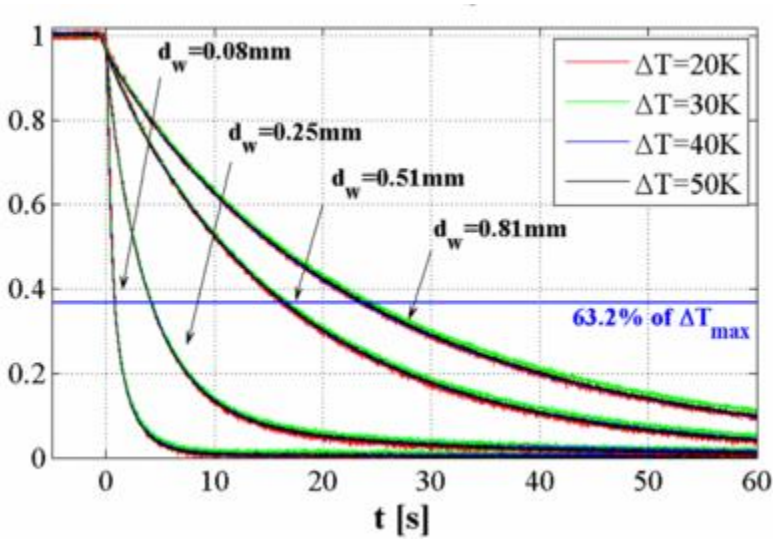

Figure 23. Thermocouple response for different wire diameters (Terzis et al. [67])

One can clearly see that thermocouple response times are a strong function of the wire diameter (which correlates directly to the bead size, hence determining the bead mass, surface area, and convective coefficient).

Calculation of the time constant depends on bead geometry (area, volume), material properties (density, heat capacity) and flow properties over the bead (convective heat transfer coefficient). Of these, perhaps the convective heat transfer coefficient is the most difficult to obtain since it can't be measured directly, whereas bead geometry and material properties are readily available. An approximation to obtaining the time constant relies on assuming the bead as a sphere of diameter $D = 2.5D_w$ where D_w is the wire diameter (D_w = 13 microns) (Omega). Material properties are assumed to be constant and the bead is assumed to be 50% Alumel and

50% Chromel by volume. The bead volume is then,

$$V = \frac{\pi D^3}{6} \tag{42}$$

The mass and thermal properties are then obtained as

$$m_b = 0.5V\left(\rho_{Alumel} + \rho_{Chromel}\right) \tag{43}$$

$$C_{p_b} = \frac{\rho_{Alumel} C_{p\,Alumel} + \rho_{Chromel} C_{p\,Chromel}}{\left(\rho_{Alumel} + \rho_{Chromel}\right)} \tag{44}$$

for the bead based on the individual material properties listed in Table 5([68]).

Table 5. Material properties of K-type thermocouple components

	Alumel	**Chromel**
ρ, kg/m^3	8610	8730
C_p, kJ/(kgK)	0.523	0.448

An alternative and perhaps more accurate method, albeit challenging to implement consists on directly measuring the thermocouple response to a step heating input at the actual measurement location in the test section under test conditions. The time required to achieve 63% of the decay in temperature is defined as the thermocouple time constant. To achieve good accuracy, it is important that the ΔT applied to the bead is on the order of the ΔT observed by the bead during measurement. For example, if the thermocouple signal exhibits an RMS of 3 degrees, one should apply a ΔT of ~ 3RMS or 9 degrees. A very large ΔT may alter the material properties such that they can no longer be assumed constant or alter the flow conditions over the bead, while a very small ΔT will not be representative of the actual response during measurement. Based on the highest observed RMS in the flow, a ΔT of 20 K was attempted.

In order to locally achieve this temperature increase, a special thermocouple circuit was designed, based on the one described in Ghodoussi [69] and in Marshall [70]. The circuit consists of 2 loops sharing the thermocouple and governed by reed relays of opposing behavior (one SPST normally open and another SPST normally closed). A single TTL signal controls both switches. In loop A, a 5 V TTL signal closes the normally open relay switch and current flows through the thermocouple, with the bead acting as a resistor. Joule heating then raises the thermocouple temperature at a rate proportional to the power input given by $P=VI$ where V is the voltage and I is the current flowing in the loop. Simultaneously, the 5 V TTL signal opens the normally closed relay switch in loop B and no signal is transmitted to the DAQ (Figure 24 a).). Once the thermocouple has been heated to the desired temperature, the TTL signal drops to 0 V, and the switch in loop A opens such that no current flows through the thermocouple anymore. Simultaneously, the switch in loop B closes and the temperature signal is acquired by the DAQ (Figure 24 (b)). This procedure is repeated 100 times to obtain a statistically significant sample, and the pulse width is controlled to govern the temperature rise (longer pulses sustain the current for a longer time, thus allowing for higher thermocouple temperatures). Data is sampled at 10 kHz and the last 10% of the thermocouple signal (per pulse) is assumed to be the steady state temperature. The time to reach 63% of the ΔT decay is obtained for each of the 100 pulses and subsequently averaged to obtain the final time constant. Unfortunately, after repeated attempts at controlling noise in the circuit and providing enough power to the circuit to raise the temperature to the prescribed $\Delta T = 20$ K in a hot mainstream, the results were not satisfactory. The power demand to achieve the

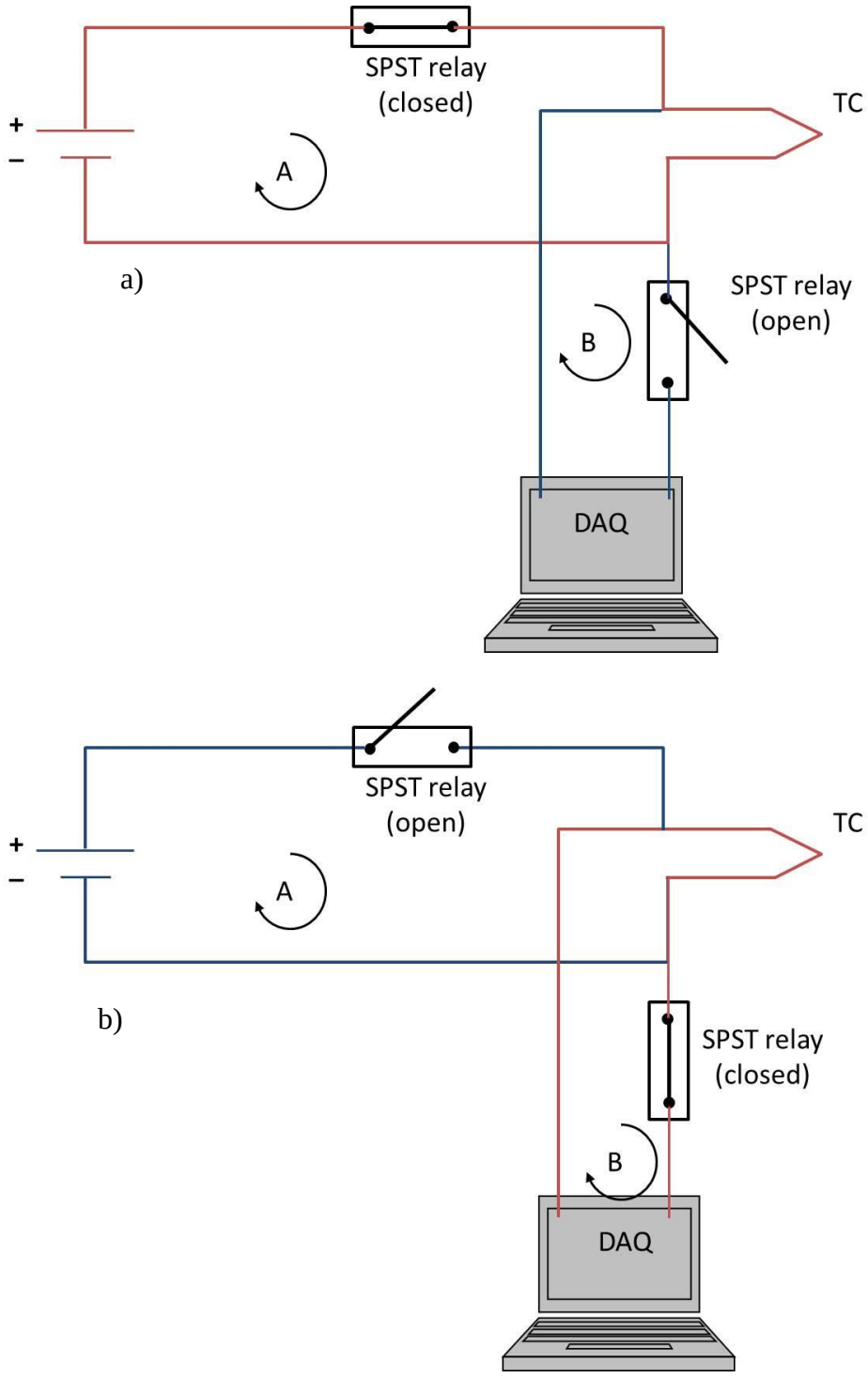

Figure 24 . a) Heating loop active b) Thermocouple signal acquisition loop active

temperature raise in the hot mainstream could not be achieved with low noise and thus the measurement was not reliable.

Due to the inability to measure time constants directly for the current work, the definition of the time constant given by equation 39 was used to estimate its values everywhere in the flow. All material and geometrical properties for the thermocouple are known, so only the convective heat transfer coefficient needs to be calculated. At any point in space, one can use bead temperature data along with PIV data to obtain the Reynolds number based on bead diameter, Re_D. Using the Whitaker correlation found in Incropera and DeWitt [71] given by

$$Nu_D = 2 + \left(0.4\,\mathrm{Re}_D^{1/2} + 0.06\,\mathrm{Re}_D^{2/3}\right)\mathrm{Pr}^{2/5}\left(\mu/\mu_s\right)^{1/4} \tag{45}$$

one can then obtain the average Nusselt number on the bead. The viscosity ratio term can be ignored based on the fact that for the range of temperatures in the study (300 K - 473 K) the entire viscosity correction factor $(\mu/\mu_s)^{1/4}$ is within $\pm$ 5% of unity, assuming the extreme situation where the bead is at the hottest possible temperature and the flow is at the coolest or viceversa.In reality, one can expect the bead and fluid to be at a temperature difference << 173 K, and thus the viscosity term should be even closer to unity. This reduces the correlation to

$$Nu_D = 2 + \left(0.4\,\mathrm{Re}_D^{1/2} + 0.06\,\mathrm{Re}_D^{2/3}\right)\mathrm{Pr}^{2/5} \tag{46}$$

Alternatively, one can also use the correlation by McAdams [72] given by

$$Nu_{D\_w} = 0.32 + 0.43\,\mathrm{Re}_{D\_w}^{0.52} \tag{47}$$

In this case, the correlation is based on the diameter of the wire, D_w, and not the bead. Regardless of the correlation of choice, invoking the definition of Nusselt number $Nu = hD/k$, where k is assumed to be the fluid thermal conductivity at the bead temperature, one can recover the convective heat transfer coefficient, h. If the

McAdams correlation is used, Carbon et al. [73] as well as Mishra [65] suggest that the time constant should instead be expressed as $\tau = (\rho_b C_p D)/(4h)$, which is based on the fact that this correlation treats the junction as a cylinder, rather than a sphere.

Both correlations were tried against the measured time constants in Carbon et al. [73]. As shown in where the measured time constant is plotted against the calculated values from both Wittaker and McAdams correlations, the McAdams correlation seemed to perform slightly better as shown by the slope of the linear fit being closer to unity, although it was consistently overestimating/underestimating the measured value by 5-20%. Based on this observation, the McAdams correlation was used for the current work, with the understanding that this error may be present in the estimation of the time constant. Looking at the temperature and velocity bounds on our flow for all cases (U_{min}= 0 m/s at the wall, U_{max} ~ 25 m/s, T_{min}= 293 K, T_{max} = 493 K) the resulting range of time constants is 2-5 ms in the fluid and approximately 20 ms at the wall.

Recalling the temperature relationship

$$T_g = T_b + \tau \frac{dT_b}{dt} \tag{48}$$

we now have a time signal $T_b(t)$ and a time constant for every measurement location. In order to minimize errors associated with finite difference schemes, spectral analysis is used to obtain the time derivative from the original signal. Instead of calculating it directly in time space, the bead temperature signal is taken to the frequency domain via FFT. In this transformation, equation 48 becomes a function of frequency ω, given by

$$T_g(\omega) = T_b(\omega) + j\tau\omega T_b(\omega) \tag{49}$$

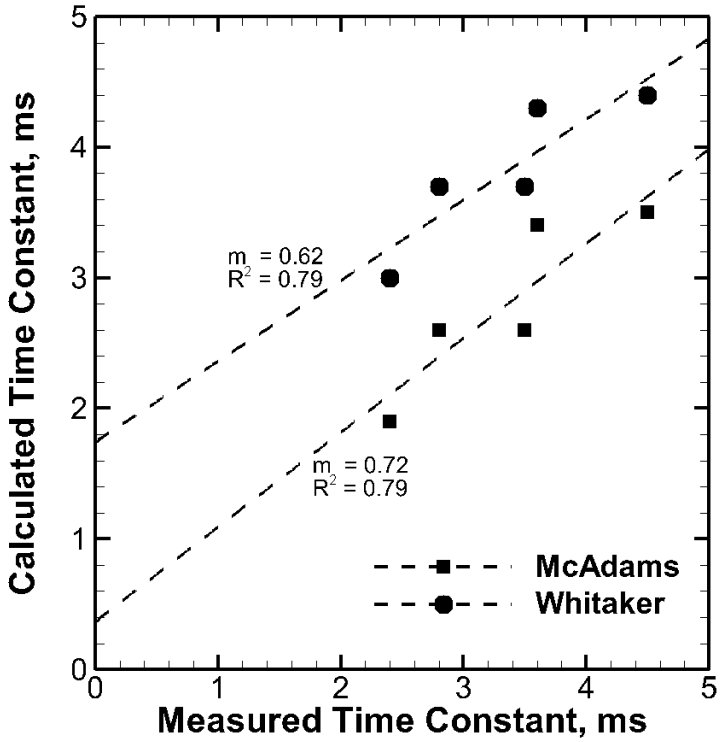

Figure 25. Time constants from correlations vs. measured time constants.

and thus $T_g(\omega)$ can be obtained. An inverse FFT returns the compensated signal to the time domain. An algorithm developed by Cruz and Marshall [16] was used to apply the digital compensation to obtain T_g, and modified to filter for electronic noise (60 Hz and harmonics which were observed in the raw data) and post process the data to obtain statistics such as mean temperature values, RMS, PDF, etc.

As observed in Figure 26, the fluctuations in the gas temperature are damped by the thermal inertia of the bead, and as a result, the RMS of the compensated signal is larger than that of the bead signal. This is the fundamental reason why compensation is important, particularly in turbulent flows, where uncompensated data may underpredict the magnitude of the temperature fluctuations. It should be noted

that the mean temperature is unaffected by compensation so the reported mean temperature values are not subjected to errors in the compensation methodology.

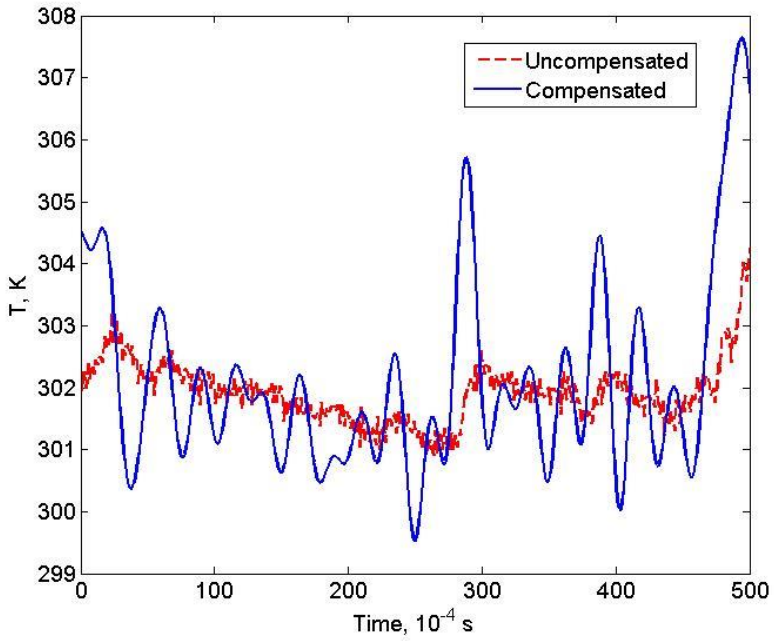

Figure 26. Characteristic compensated vs. uncompensated temperature signal (SNR =5)

This technique, however, is sensitive to the value of the time constant as well as the determination of the allowable signal to noise ratio (SNR). The compensation method relies on an FFT, which in turn requires a low pass filter (essentially defining the maximum frequency content which will be compensated). The net effect is that at higher SNRs, the cutoff frequency becomes lower, and the compensated T_{RMS} decreases. Physically, the governing temperatures of the system are the mainstream temperature and the coolant temperature (in the adiabatic cases), and these temperatures should not have a large RMS associated with them at the inlet. Thus, at any measurement location the instantaneous temperature should not exceed the mainstream temperature, nor should it fall below the coolant injection temperature

(within a narrow bound associated with the relatively small RMS in the inlet temperatures). Assuming a true RMS < 1% for both coolant and mainstream temperatures, a constraint of 2 K below T_c was imposed as the lowest possible instantaneous compensated temperature and a constraint of 2 K above T_∞ was imposed as the maximum possible instantaneous compensated temperature.

For each shear case, the compensated temperatures were iterated over by varying the SNR. For each compensated temperature profile, the range of instantaneous temperatures was analyzed to identify the maximum and minimum compensated instantaneous temperatures and compared against the allowable reference values. It was found that for SNR $\geq$ 50, this criteria was satisfactorily met for all cases. As such, a value of SNR = 50 was used for the compensation technique for all cases.

It is worth noticing that given the SNR constraint, the noise floor corresponds to high frequencies, including those associated with the residence time of eddies, as shown in Table 4. Thus, despite the original sampling time being able to capture several eddies, this information cannot be recovered due to compensation, as the signal and noise in this frequency range cannot be uncoupled. The technique was further checked against the statistical property of distributions where the variance of the distribution is equal to the integral of the power spectral density over all frequencies [74]. After compensation, this relationship held true within 2%, which is well within the limits of error of the numerical trapezoidal integration method used. Figure 27 shows the power spectral density (PSD) of a representative thermocouple measurement as a function of frequency. For a time constant τ = 5 ms, the effect of

varying the SNR is shown. As one can see, high SNRs result in cutoffs at higher power and lower frequencies, resulting in lower RMS of compensated temperature. Similarly, Figure 28 shows the effect of varying time constant for a constant SNR=50. Higher time constants result in higher recovered powers at the same frequency, which also lead to higher RMS. These effects highlight the impact of choosing adequate SNR and time constants for the final compensation. These figures also highlight the fact that both the SNR and the time constant choice result in a coupled effect which cannot currently be uncoupled due to experimental uncertainty. Furthermore, even with conservative estimates, data cutoff occurs during a constant power regime in the PSD. Because one expects the power to decay, and no decay is observed after compensation, it is likely that the compensation cutoff results in unrecoverable power contributions to the RMS. As such, compensation will tend to underpredict true RMS.

Because of the uncertainty associated with the choice of time constant and SNR, one should exercise caution when comparing results from turbulent fluctuating temperatures between experiments and CFD. However, qualitatively one can show that the overall shape of a turbulent fluctuation profile is relatively self-similar regardless of the time constant and SNR, as long as their corresponding values are reasonable. As an example, Figure 29 shows an uncompensated T_{RMS} profile along with profiles calculated with the SNR used in this work and 3 different time constant values (2.5, 5.0 and 7.5 ms). Plotted as $T_{RMS}/T_{RMS,max}$, one can see that the compensated profiles exhibit very little difference between each other, particularly between the peak location and the wall. Thus, a judicious compensation approach

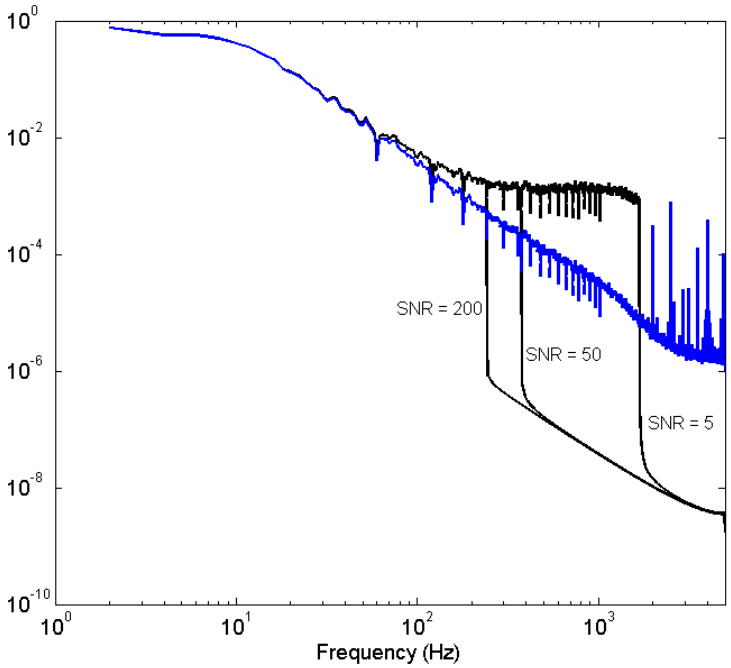

Figure 27. Effect of SNR on thermocouple compensation

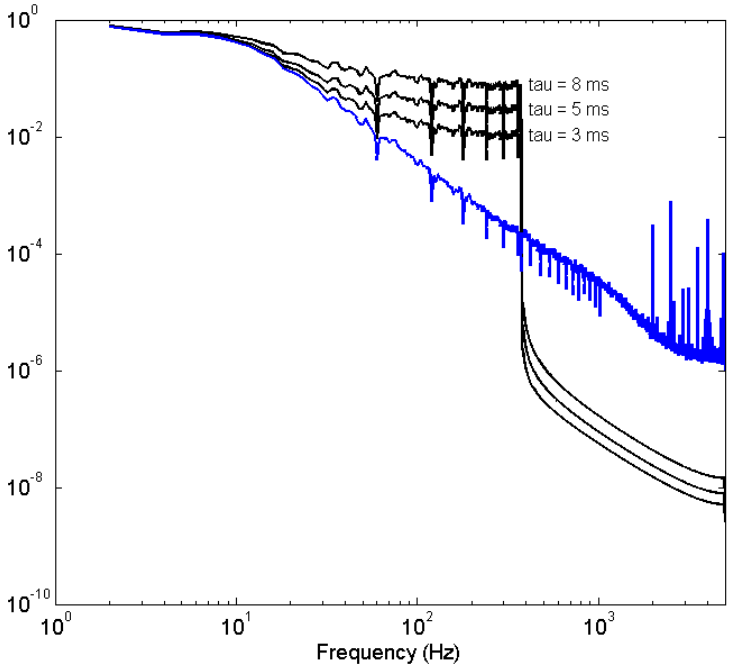

Figure 28. Effect of time constant value on thermocouple compensation.

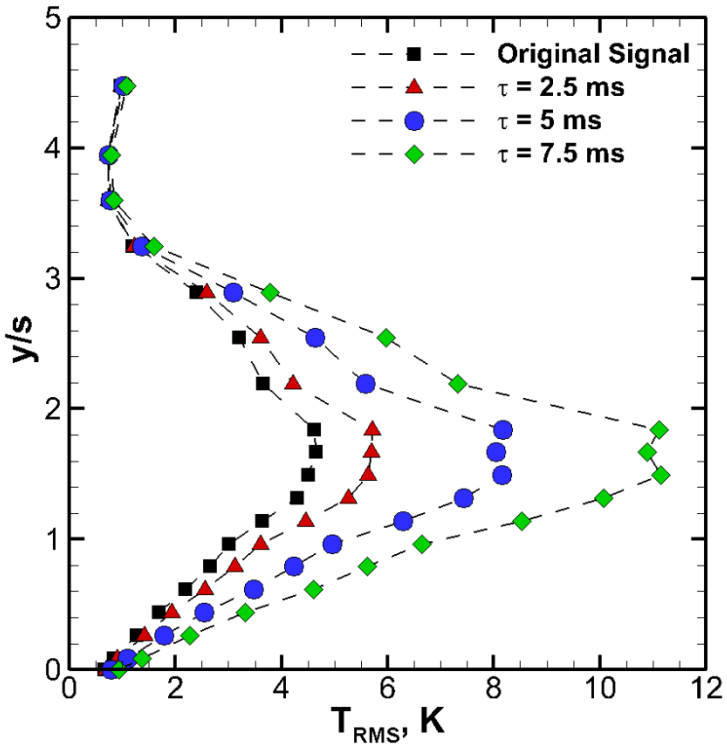

(a)

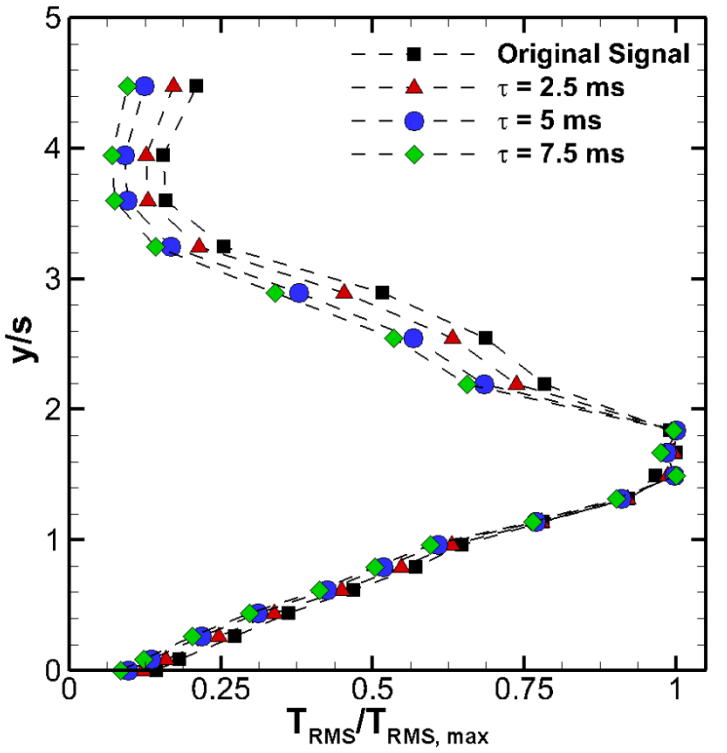

(b)

Figure 29. T_{RMS} profile (a) Raw data, (b) non-dimensionalized by $T_{RMS,max}$

may be used to compare experimental results to CFD qualitatively, even if the actual temperature values may not agree due to the inherent error in the compensation methodology.

2.2.7 Heat Transfer

Given that one of the main objectives of this research is to provide comprehensive experimental data for validation and development of CFD film cooling models, one of the most important aspects is the quality of the experimental data. Despite the great care under which this experimental campaign has been performed, it is inevitable to run into some situations where the quality of the data is not ideal. One such situation arises when evaluating the near-wall performance of the models. Film cooling is inherently a turbulent fluid mixing phenomena coupled with near wall transport. While the mixing aspect is well characterized by the experiments, the near wall resolution of the PIV measurements was good on a global scale (< 0.5 mm from the wall) but not nearly as well resolved as to allow a direct comparison of velocity gradients between experiments and simulations, particularly the very important wall gradient. While a first approach was attempted via the Clauser method, yet another approach to validate CFD near wall performance is to perform heat transfer measurements.

It is well established from classical boundary layer theory (Batchelor [74], White [75], Kays and Crawford [47]) that the heat transfer to a surface is governed by the boundary layer behavior. In particular, the Navier-Stokes equations can be reduced to slightly simpler forms inside the boundary layer. The boundary layer equations for conservation of mass, momentum, and energy are coupled such that the

kinematics of the flow affect the heat transfer (Incropera and DeWitt [71]). In dimensional form, these equations are (for an incompressible 2-D flow)

$$\frac{\partial u}{\partial x}+\frac{\partial v}{\partial y}=0 \tag{50}$$

$$u\frac{\partial u}{\partial x}+v\frac{\partial u}{\partial y}=-\frac{1}{\rho}\frac{\partial p}{\partial x}+\nu\frac{\partial^2 u}{\partial y^2} \tag{51}$$

$$0=-\frac{1}{\rho}\frac{\partial p}{\partial y} \tag{52}$$

$$u\frac{\partial T}{\partial x}+v\frac{\partial T}{\partial y}=\alpha\frac{\partial^2 u}{\partial y^2}+\frac{\nu}{c_p}\left(\frac{\partial u}{\partial y}\right)^2 \tag{53}$$

One can readily see that the momentum equations are coupled to the continuity equation. Furthermore, the energy equation is coupled to the momentum equations through the velocity terms. A solution of the momentum equation is required before the energy equation can be solved. Once all the solutions have been found, one can proceed to calculate the heat flux. In particular, it is the wall gradients (velocity and temperature) that determine the heat transfer at the surface. The advection terms in the boundary layer energy equation show that advection/convection is dominated by the coupling of the local velocity within the boundary layer and the temperature gradients. The local velocity is in turn related to the local boundary layer thickness and conservation of mass. As such, one can assert that if a model adequately captures the heat transfer behavior of a problem in addition to the mean kinematics and thermal behavior of the flow, then it must also capture the near wall behavior as it is this near wall behavior (within the boundary layer and at the wall itself) that determines the heat flux. Based on this assertion, one can then

provide heat transfer data to assess the capability of a model to capture near wall behavior in lieu of direct velocity gradient data.

Based on this reasoning of the importance of heat transfer data as a reflection of near-wall kinematic and thermal behavior, the adiabatic experiments were repeated under non-adiabatic conditions while trying to maintain commonality between them. As such, there are once again 3 distinct blowing ratios under non-adiabatic conditions and kinematic and thermal data was obtained in addition to heat transfer. While the adiabatic data set can be used for validation, the absolute validation should be obtained with the heat transfer data as this is the complete data set that adequately reflects the coupling between mixing and near wall behavior.

Experimentally, the non-adiabatic boundary condition was obtained by removing the insulation from the back of the test section and replacing it with a water jacket. Chilled water (280 K-283 K) from a reservoir was continuously circulated at high flowrates (30 GPM) in the same direction as the mainstream flow. The ideal objective was to obtain a nearly isothermal backside wall temperature profile as this condition would be easier to implement in a numerical simulation. However, it was observed that the backside wall exhibited a slightly non-linear monotonically increasing profile. Nevertheless, the backside temperatures were within 3 K and well below the hot side wall temperatures, clearly establishing a significant thermal gradient across the test plate as desired. Furthermore, these temperatures were continually monitored over time, exhibiting a very slight increase of < 2K during the entire experimental run (~ 4 hours), suggesting a nearly steady state behavior for the

purpose of this work. All of this data is available for model validation depending on the desired fidelity.

Despite the well characterized boundary condition along the backside wall, it is important to understand that on the hot side of the surface, all 3 modes of heat transfer are at work. The cold backside establishes a thermal gradient across the solid plate that drives a conduction heat flux. The mixing flows and near wall gradients on the hot side drive a convection flux, while the interaction between the solid wall and its surroundings drive a radiative flux. This latter flux can be quite complicated to measure directly, but it can be estimated under certain assumptions. The following discussion presents the energy balance on the plate as well as the methodology to estimate the radiative heat flux.

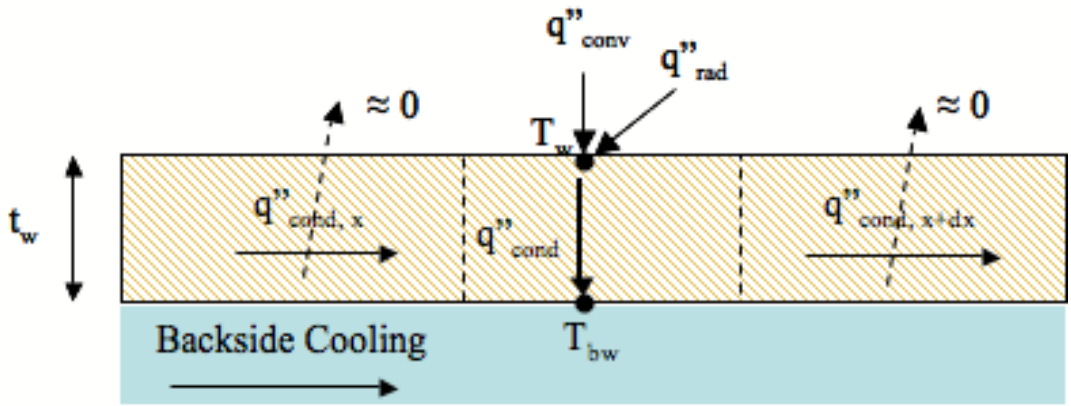

Figure 30. Energy balance on test plate

Assuming the flow over the plate to be 2-D (varying along the wall and in the wall normal but not in the spanwise direction, one can perform an energy balance at any particular location along the plate. Defining convection and radiation as positive into the wall and conduction through the plate to the backside water channel as negative, then the energy balance is

$$q''_{cond} = q''_{conv} + q''_{rad} \tag{54}$$

The conductive heat transfer is assumed to be 1-D (neglecting axial conduction). This was verified a priori with a small numerical simulation in Matlab using known hot side temperatures from measurements, assuming an isothermal backside wall with T = 283 K and adiabatic ends. The simulation showed that the large thermal gradients across the plate far dominated any axial gradients, and thus the assumption was valid. Using Fourier's law, the conductive heat transfer is given by

$$q''_{cond} = \frac{k_w}{t_w}(T_w - T_{bw}) \tag{55}$$

where k_w is the thermal conductivity of the plate, t_w is the thickness of the plate, T_w is the hot side wall temperature and T_{bw} is the backside wall temperature. For this work, k = 0.26 W/mK [76], t_w = 8.1 mm, and the temperatures are all known from measurements.

To estimate the radiative flux, it is assumed that at the thermocouple measurement location, the surface area of the plate can be approximated as a differential element given the small size of the bead. It is further assumed that radiation only occurs directly between surfaces (i.e. no re-radiation). While it is theoretically possible to attempt a radiosity approach to take re-radiation into account, the complexity of the calculation and the amount of unknowns increases such that further estimates are necessary. This would not only increase the uncertainty of the overall radiative transfer but the calculation time would also increase significantly with no apparent benefit. Trading a more physically accurate model with larger

uncertainties for a lower order model with less uncertainty and simpler execution, the direct approach was deemed suitable.

In this approach, the entire enclosure is divided under the following assumptions for simplicity:

- Radiation cannot be exchanged between coplanar surfaces (i.e. between different locations along the test plate)
- The louver is assumed to be flat and aligned with the rest of the test plate, ignoring the small step. As such, radiation cannot be exchanged between the louver and the rest of the test plate.
- Each measurement location on the plate is assumed to consist of a differential element.
- The enclosure is subdivided into main surfaces. A metal surface parallel to the test plate, two metal surfaces that intersect the test plate at perpendicular angles, a window parallel to the test plate, a window perpendicular to the test plate that does not intersect the test plate.
- The windows are thermally opaque (i.e. they will not transmit, only emit and reflect). Given the material (quartz) and the fact that the highest emitting surfaces in the problem have temperatures < 373 K it can be shown that the majority of the emission at these temperatures occurs at wavelengths for which quartz is not transmissive (Quartz (SiO_2) is not transmissive at wavelengths > 4 microns) [77]. For example, the test plate at the highest measurement temperature of 373 K emits radiation at a peak wavelength of 7

microns and 94% of the total radiation emitted occurs at a wavelength > 4 microns. Cooler surfaces emit at even longer peak wavelengths.

- The ends of the test section are ignored such that the entirety of the above mentioned surfaces form a perfect enclosure (sum of view factors = 1).
- The geometries of the surfaces listed above are all known and the corresponding material properties are known as well. Their temperatures have also been measured. As a result, there are N surfaces, all of known area, emissivity and temperature. The view factors between surface *i* and *j* can be calculated using Howell's reference manual [78].

The view factors between a differential element and the front casing window are calculated using the differential element to parallel rectangle calculation given by

$$F_{d1-2} = \frac{1}{2\pi}\left(\frac{A}{\left(1+A^2\right)^{1/2}} \tan^{-1}\left[\frac{B}{\left(1+A^2\right)^{1/2}} \right] + \frac{B}{\left(1+B^2\right)^{1/2}} \tan^{-1}\left[\frac{A}{\left(1+B^2\right)^{1/2}} \right] \right) \quad (56)$$

where A and B are defined as $A=a/c$, $B=b/c$ based on the geometry shown in Figure 31.

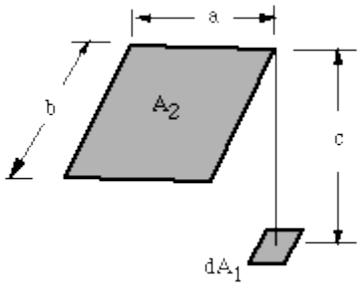

Figure 31. Geometry for view factor calculation

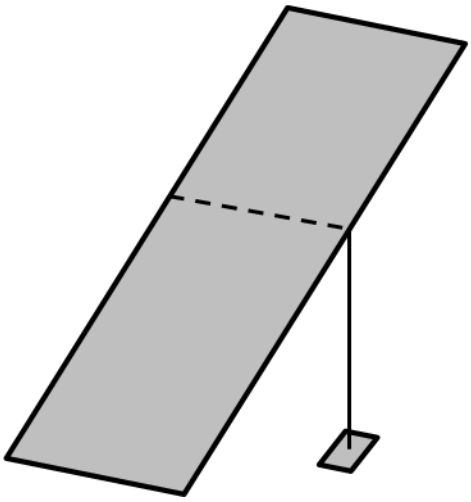

Figure 32. Diferential element to 2 parallel rectangles approach used to obtain the total view factor from plate element to front casing window.

Because the differential elements are never perfectly aligned with the corners of the window, a linear addition is implemented where the window is split into 2 parts, each of which has a corner aligned with the differential element. The view factor is calculated for each of the two resulting setups and added.

A similar approach is used to calculate the view factor between the plate element and the side window. In this case the view factor for a differential element to a rectangle perpendicular to the plane containing the differential element is used. This is given by

$$F_{d1-2} = \frac{1}{2\pi}\left(\tan^{-1}\left[\frac{1}{C}\right] - \frac{C}{Y}\tan^{-1}\left[\frac{1}{Y}\right]\right) \tag{57}$$

where C and Y are defined as $A=a/c$, $C=c/b$, $Y=(A^2+C^2)^{1/2}$ based on the geometry shown in Figure 33.

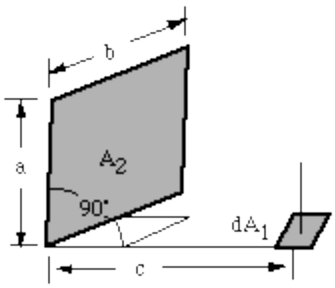

Figure 33. Differential element to perpendicular rectangle.

The linear addition of 2 view factors is used again to obtain the total view factor as the corners of the window are never aligned with the plate element.

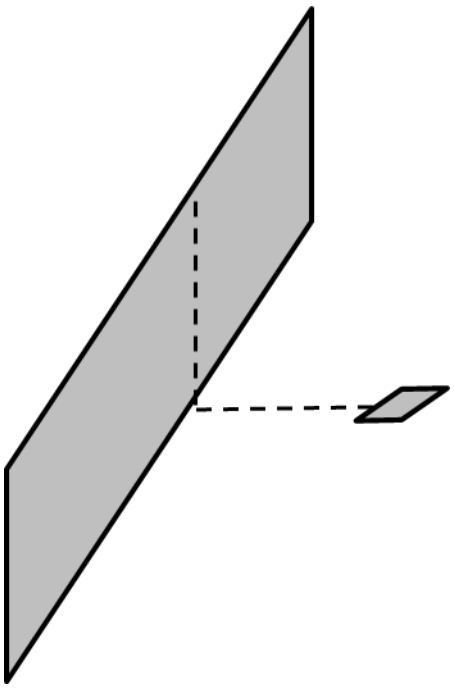

Figure 34. Differential plate element to side window. 2 view factors are added to obtain the total.

The view factor between each surface and the parallel metal surface is obtained by enforcing the summation rule instead of direct calculation in order to enforce the perfect enclosure assumption. With all the properties known, the net radiative heat

transfer between any surface i and any other surface j in the enclosure is given by Siegel and Howell [79] as

$$\dot{q}_{ij} = \varepsilon_i \varepsilon_j \sigma F_{ij} A_i \left(T_i^4 - T_j^4\right) \tag{58}$$

and in flux terms (per unit area) this becomes

$$\dot{q}''_{ij} = \varepsilon_i \varepsilon_j \sigma F_{ij} \left(T_i^4 - T_j^4\right) \tag{59}$$

The neat radiative heat transfer to surface *i* is the sum of all of its interactions with the different surfaces in the enclosure

$$\dot{q}''_i = \sum_j \dot{q}''_{ij} \tag{60}$$

In the case of this work, each wall measurement location is essentially a differential surface exchanging heat with the casing, the front window and the side window (j = 3). In this definition of the problem, a negative value corresponds to the surface being heated while a positive value corresponds to the surface being cooled by the net radiative exchange. Letting *i* = 1:5 correspond to the 5 wall surface measurement locations, then the heat flux at these locations is what we are ultimately after. Typical values showed that radiation corresponded to about 10-20% of the total heat transfer at the surface and radiation contributions were stronger near the inlet, where the wall surface temperatures were lower.

Once the radiative heat flux is estimated, one can proceed to derive the convective heat flux by rearranging equation 54 as

$$q''_{conv} = q''_{cond} - q''_{rad}\,. \tag{61}$$

While these values can provide tremendous value to CFD modelers to validate a simulation using the same boundary conditions and geometry of the test section, and

the experimental data can be used to compare the relative behavior of each velocity ratio, one can expect that a different boundary condition may lead to different results and observations, and so the data is useful for validation but is not definitive for interpretation (unlike in the adiabatic case). One approach to recast the data is to derive the convective heat transfer coefficient from adiabatic and non-adiabatic measurements. This approach relies on the assumption that both adiabatic and non-adiabatic data was obtained at the same location, under the same kinematic and thermal conditions. Not only is this not the case in this work, but the error associated with this derivation even under ideal conditions is relatively high (~60%) and offers very little additional value to modelers. Perhaps a better way to put the data into perspective and derive more conclusive observations is to compare the observed heat flux vs. a theoretical limit. Since film cooling is expected to reduce the temperature at the wall, thus reducing the heat load to the wall, a useful comparison is to relate the heat flux with film cooling to the heat flux without film cooling.

An important distinction must be made here. While heat flux without film cooling may refer to the heat flux observed by simply shutting the film flow off while keeping the slot geometry, this is not representative of an engineering approach. Not only will this create a complex flow (backward facing step), but it is also an incorrect reference. One must think that when determining the value of film cooling, it should be compared to a propulsion system where film cooling hardware has not been installed at all (no plenums, manifolds, louvers etc.). Thus, the merit of this exercise lies in determining what the final reduction in heat flux will be from a baseline

system with no film cooling hardware to a film cooled system including all geometric modifications to accommodate it.

To this effect, one can envision a channel with the same dimensions as the test section, where air at the same temperature and velocity is flowing as in the mainstream of the film cooled cases. Furthermore, the wall is still backside cooled, but in the absence of the film, the heat flux is governed only by this mainstream and the backside temperature. Radiation is assumed to be negligible in this scenario, such that

$$q''_{conv} = q''_{cond} \tag{62}$$

Under these conditions, both the reference case and the experimental film cooled case exhibit the same boundary conditions and the same mainstream conditions. The resulting heat flux in this exercise can be obtained by assuming a fully developed channel flow and invoking the appropriate Nusselt number correlation for this flow type. Kays and Crawford [47] report the Nusselt number for a turbulent channel

$$Nu_D = 0.023 \mathrm{Re}_D^{4/5} \mathrm{Pr}^{1/3} \tag{63}$$

Recalling that $Nu_D = hk/D$, then the convective heat flux coefficient becomes $h = Nu_D D/k$ and the energy balance becomes

$$\frac{Nu_D D}{k}(T_\infty - T_w) = \frac{k_w}{t_w}(T_w - T_{bw}) \tag{64}$$

where the mainstream temperature and backside wall temperatures are the same as in the film cooled case of interest, and the convective heat transfer coefficient has been replaced by the corresponding Nusselt number given by Equation 63.

Solving for T_w which is the only unknown, one can then calculate the reference heat flux $q''_{turbchan}$ given by

$$q''_{turbchan} = \frac{Nu_D D}{k}(T_\infty - T_w) \tag{65}$$

The relative performance of the film cooled system can now be compared to a canonical system with the same backside boundary condition, the same mainstream velocity and the same mainstream temperature, thus isolating the impact of the film injection alone. The percent reduction in heat flux can be expressed as

$$\%reduction = 1 - \frac{q''_{conv}}{q''_{turbchan}} \tag{66}$$

where higher values correspond to a strong heat flux reduction, while lower values correspond to very little reduction. This comparison approach can be easily implemented during the design phase of any propulsion system where film cooling is a viable option in order to determine the cost/benefit of such a system.

2.3 Test Matrix

Realistic applications of slot film cooling can be found in all types of propulsion systems, from rockets to air breathing engines. However, the initial shear configurations of the flow schemes vary greatly depending on the type of system. In rockets, the coolant is normally injected with a velocity that lags with respect to that of the freestream, while a gas turbine combustor typically sees the coolant being injected with velocities that exceed those of the freestream. These two extremes of shear configurations result in flowfields that, although they retain some similarities, also exhibit some important differences. Thus, it is critical that a robust model can

accurately resolve flowfields that lie at and in between these shear configurations. For this reason, the experimental database consists of 3 distinct cases covering both extreme shear configurations as well as a limiting case where the velocities are matched so as to minimize the shear between the flow streams at the inlet.

Realistic conditions are achieved by using hot and cold flows correspondingly. To preserve some commonality among cases, the temperature ratios were kept nearly identical for all cases, while varying the velocity ratio. 3 limiting cases are examined, a wall jet ($U_c > U_\infty$) a min-shear case ($U_c \sim U_\infty$)), and a wall-wake ($U_c < U_\infty$)). For each of the cases in question, there was an adiabatic and a non-adiabatic experiment. While an effort was made to achieve similar inlet conditions between adiabatic and non-adiabatic cases with the same velocity ratio, this was not perfectly achieved due to slight changes to the slot height. Nevertheless, the non-adiabatic cases still correspond to wall jet, min shear and wall-wake situations. Furthermore, each case is its own standalone set with full kinematic and thermal data, and thus provides complete information for CFD modelers. For example, a modeler may use the adiabatic data set to validate an adiabatic model, and then modify the simulation to accommodate heat transfer. For this second simulation, the relevant non-adiabatic data set is fully available.

The reference values reported in the table are those actually measured during each experiment. Because PIV profiles and temperature profiles are taken very close, but not exactly at the inlet, there are some effects that must be addressed carefully in order to ensure that these reported values correspond to the true inlet conditions as best as possible. For velocities, the mainstream velocity is the PIV value obtained at

y/s = 4.0. This is far from the wall and the profile exhibits minimal variation between neighboring locations at this distance (*du/dy*~0). Due to the nature of the film generation, the coolant exit flow does not exhibit a perfectly symmetrical, fully developed turbulent channel profile as one may expect. While it retains some of the features of a turbulent channel (top hat shape), the profile is skewed in one direction. This is consistent for all cases. This feature, combined with the lack of accurate data points near the wall and louver make it difficult to integrate the profile to obtain a bulk velocity value without making several assumptions. As such, and given the experimental nature of this work, the reference velocity for the coolant is defined as the peak velocity observed between *y/s* = 0 and *y/s* = 1.0. This provides a more accurate description of the observed flow. At the discretion of anybody who may want to build on this work or use it in a simulation, this reference peak value can be readily used for direct comparison and an equivalent fully developed turbulent channel profile can also be reconstructed using a 1/7 power law.

For temperatures, the mainstream temperature is obtained at *y/s* ~ 5.0. This is close to the same location as the PIV measurement for the mainstream velocity. It is well into the mainstream and neighboring points do not exhibit a significant thermal variation. For the coolant in the adiabatic case, the minimum temperature in the profile is used. Minor profile corrections were applied due to radiation heating up the wall slightly (~1 K) above the minimum observed gas temperature. Initial radiation correction estimates based on correlations provide results in the right direction (real wall temperature lower than measured), but they tend to overestimate the correction. It should be noted that these corrections were not necessary downstream where

radiation errors were noticed to be much smaller than at the inlet. For $y/s > 0.2$, the RMS of temperature starts exhibiting an increase, suggesting that temperatures further away from the wall may not accurately represent the true coolant temperature. It is assumed that any mixing has not significantly impacted this reference location so close to the inlet (an observation that flow visualization supports). In the case of non-adiabatic coolant, the wall temperature is clearly an erroneous reference, as it is below the coolant temperature due to backside cooling. Instead, it is assumed that an equivalent location of $y/s = 0.2$ represents the ideal location where neither wall effects nor mixing have significantly impacted the temperature. As seen, the test matrix covers a wide range of velocity and blowing ratios. The slot Reynolds number is always > 2000 which ensures turbulent flow at the slot exit for all cases. The test matrix is presented in Table 6 and has been color coded to aid the reader with respect to the color scheme used in the results section.

Table 6. Test matrix for the current study.

Inlet	Wall-Wake AD	Wall-Wake NA	Min Shear AD	Min Shear NA	Wall Jet AD	Wall Jet NA
VR	0.46	0.46	1.00	0.95	2.00	1.72
TR	1.57	1.46	1.59	1.50	1.58	1.53
m	0.72	0.67	1.59	1.42	3.16	2.63
Re_s	3700	2300	7000	4400	6500	4000
U_c, m/s	11.34	11.96	20.96	20.51	22.46	19.54
U_∞, m/s	24.73	26.00	20.93	21.63	11.22	11.36
U_{conv}, m/s	18.04	18.98	20.95	21.07	16.84	15.45
T_c, K	295.10	313.53	286.13	301.76	294.04	300.83
T_∞, K	463.24	457.93	455.15	451.27	464.47	460.46
s, mm	6.1	4.1	5.7	4.2	5.3	3.9

2.4 Uncertainty analysis

All of the measurement techniques discussed earlier are not without error. Several derived measurements will also undoubtedly be subject to error propagation as they depend on several measured quantities. This section addresses the expected errors associated with each technique using estimations and fundamental error propagation analysis.

2.4.1 PIV Errors

As mentioned before, PIV can be subject to several sources of error, arising from physical behavior of particles, optical system aberrations and inherent numerical algorithm errors. For this work, the sources of error were investigated in the literature, and special care was taken to minimize such sources. The most important sources of error and estimation of their impact on the final result are presented here.

Seeding particle size can introduce error due to inertial effects, where a very large particle will not be able to faithfully follow the flow. Earlier discussion showed that the criteria for a seeding particle to follow the flow down to the smallest turbulent timescale was achieved if the Stokes number was < 0.2. This criteria was met, and as such, one can expect the error associated with seeding particle size to be $<$ 2% as suggested by Samimi et al. [39] and is probably closer to 1% for this work.

Another source of error is associated with in-plane and out of plane motion of particles. While these sources of error have been quantified, their impact on the final result is slightly different. Instead of reducing the accuracy of the measurement, particle loss due to in-plane and out of plane motion will make it impossible for the algorithm to actually work, in which case the algorithm will not return a vector result.

Severe loss of particles then translates into fewer valid realizations for any given number of images (up to 50%). This, however, does not necessarily affect the actual accuracy of valid measurements. However, if statistics are applied to a set and the realizations are not sufficient, then the derived quantities may be unreliable. In this work, all the recommended criteria to minimize loss of particles was met and realizations were better than 90% throughout except very close to the wall. These regions of poor realization also coincided with noise dominated regions and were truncated from the final result as explained earlier.

Particle image size (not to be confused with particle physical size) is also an important source of error in PIV measurements. Raffel et al. used artificial PIV images with a prescribed displacement to show that, regardless of the interrogation window size, measurement accuracy was best if the particle image diameter $d_i < 2$ pixels. If this criteria is met, displacement accuracy was within 0.01 pixels. Given the FOV used and the gate time, this translates to absolute velocity accuracy within 0.0214 m/s. This accuracy is > 99% for most of the resolved mean velocities.

Another important source of error arises from calibration. During this procedure, the physical relationship between pixels and physical dimensions of the plane of interest is established. An erroneous calibration will improperly convert pixel displacement (which may be highly accurate) to physical displacement. To minimize calibration errors, a combination of steps can be used. First, the reference plate used for calibration is marked with a grid with millimeter spacing (an accurate measuring tape, for example). Then, calibration is performed using a zoom-in version of the image to improve the accurate location of the 2 reference points to measure length.

Finally, as much as possible of the grid is used during calibration. The accuracy using this procedure can be estimated to be on the order of 1 pixel. Non-use of the zoom-in feature can increase this to about 4-5 pixels. Given the settings used in this work, this translates to an error of < 0.05%. However, this error increases if one does not use as much of the grid as possible to define the endpoints of the calibration (error can be up to 3% if one uses 1/64 of the grid spacing, for example). Overall, calibration error is quite small compared to other sources of error, but it is still important to perform the procedure in an appropriate manner.

Because these errors are independent of each other, their combined effect on the final result should be a simple addition of the total. With proper care in the experiment design and optimizing the parameters with the guidelines provided in the literature, PIV measurements in this work have expected accuracies > than 99%

A secondary error related to PIV measurements but not to the velocities is the uncertainty in the vector location in space. As designed, the algorithm places each vector at the center of the interrogation region. While this is a fine approximation in most cases, it is not appropriate near boundaries or in regions where seeding concentration is biased. To illustrate this effect, one can imagine an interrogation window that includes both seeding particles and a wall. The top 50% of the window contains seeding particles, the wall cuts the window right through the center and everything below it is a stationary image of the wall. Assuming that the noise from the wall does not contribute to the result and that the particles are enough to provide a valid vector result, the algorithm will provide a valid vector and place it at the center of the window. This is clearly erroneous because the center of the window clearly

corresponds to the wall location (y = 0), yet a vector with U > 0 m/s is placed at this location, violating the no-slip condition. A more accurate approach would be to place the vector at the center of the signal contributing region of the window. In this case, since only the top half of the window contributes to the vector, the vector should be placed halfway between the top and center of the window. This results in a shift in the vector location of ¼ of an interrogation window. Given particle image sizes and interrogation window sizes used in this work, this ¼ interrogation displacement is the largest expected error in vector placement, corresponding to 4 pixels or 68 μm in actual space. Figure 35 shows an erroneous vector location along with the correct location when this bias is accounted for.

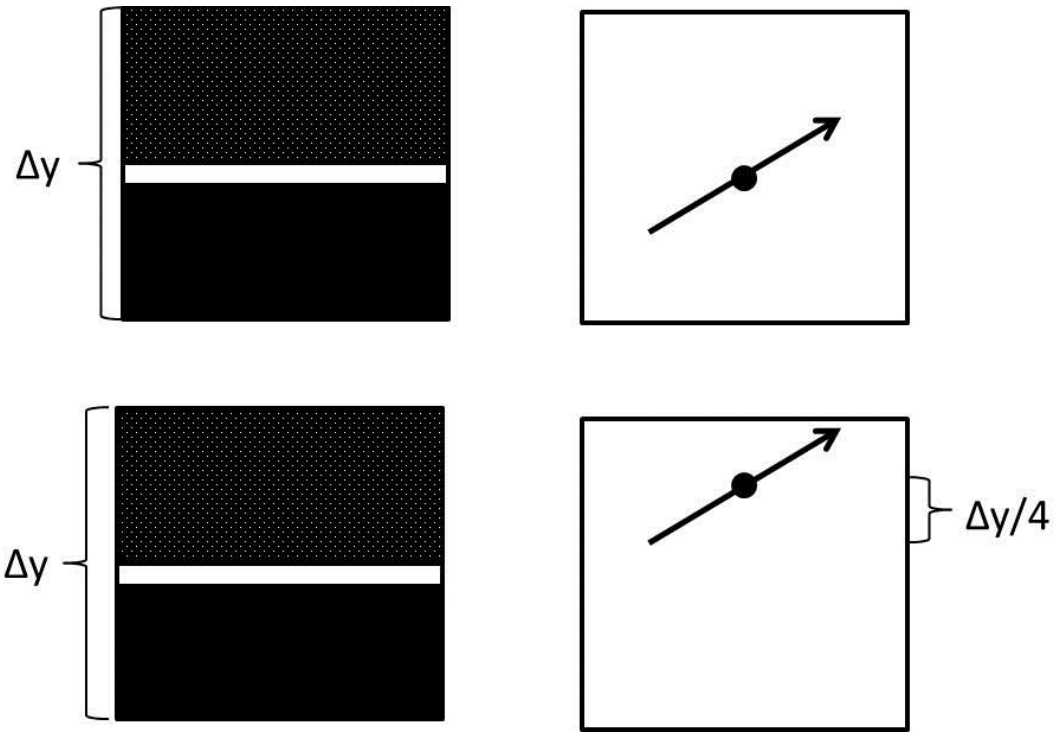

Figure 35. Uncertainty in PIV vector location due to seeding bias within interrogation window.

While this scenario can occur anywhere in the flow, the most likely situation when this arises is near the walls. It has been shown that near the walls, the noise dominates and the measurement is actually not valid, thus the impact of this uncertainty is not an issue since the data at that location is discarded. While it is expected that the flow is seeded homogeneously based on monitoring of images prior to data acquisition, local seeding bias may occur sporadically. Unfortunately, the algorithm cannot accurately detect these occurrences, and it is impossible to manually detect them as it would require inspection of every image in each data set. Fortunately, it would take a consistent behavior for this to actually impact the results (i.e local seeding bias would have to occur in most of the 500 images at the same spatial location). Inspection of the results does not suggest a strong impact of this uncertainty on the final results (for example mean velocity profiles would look somewhat skewed and jagged if this was a repeating issue). As such, this uncertainty is reported, although data inspection suggests that its impact is minor in the overall sense.

2.4.2 Temperature errors

Thermocouples and DAQ systems used to acquire their signals are undoubtedly prone to different sources of error. Measurements derived from temperature readings (such as heat transfer data) will then be subject to error propagation. This section addresses the sources of error and their impact on subsequently derived measurements.

The K-type thermocouples used in this work are rated by the manufacturer to have limits of error of 1.1 K. Sets of repeating measurements under well controlled conditions (ambient air, quiescent flow) showed that a single thermocouple was

repeatedly showing the same mean temperature with variations well below the 1.1 K limit. This suggests that for a single thermocouple, this error is actually systematic and not random. The much smaller variations, which were random, can be attributed to the resolution of the DAQ system. In this case, random error under well controlled conditions was shown to be on the order of 0.25 K.

It is important to take both errors into account, as their impact will be different based on whatever the derived measurement is. For example, adiabatic wall effectiveness is a function of 3 distinct temperature measurements, all of which are acquired with the same thermocouple. Thus, adiabatic wall effectiveness is not subject to the systematic error (as this error would cancel out during the normalization procedure). However, random error effects must be accounted for.

Error propagation can be estimated using the partial differentiation approach described in Bevington [80]. If a quantity P is a function of n measured quantities Z_n, such that $P(Z_1, Z_2, Z_3, \ldots Z_n)$, then the total error of the quantity P, ΔP is given by

$$\Delta P = \sqrt{\sum_{1}^{n}\left(\frac{\partial P}{\partial Z_n}\Delta Z_n\right)^2} \tag{67}$$

where ΔZ_n is the error associated with each quantity. This error is absolute and in general will be different any time the value of the quantity P changes. In that respect, expressing the relative error $\Delta P/P$ provides better insight as to the effect of error propagation on the final quantity.

In the case of adiabatic effectiveness, the relative error is given by

$$\frac{\Delta\eta_{aw}}{\eta_{aw}} = \sqrt{\left(\frac{\Delta T_c}{T_\infty - T_{aw}}\right)^2 + \left(\frac{\Delta T_{aw}}{T_\infty - T_c}\right)^2 + \left(\frac{T_\infty - T_c}{T_\infty - T_{aw}}\frac{\Delta T_\infty}{T_\infty - T_{aw}}\right)^2} \tag{68}$$

with $\Delta T_{aw} = \Delta T_c = \Delta T_\infty$ assumed to be the random error of the DAQ system = 0.25 K. For adiabatic effectiveness values in this study, the relative error was always < 0.3%. Furthermore, the same equation applies to the non-dimensional gas temperature η_g in which case T_{aw} is replaced by the local gas temperature T_g. In this case, relative errors vary significantly because the non-dimensional temperature goes to 0 at the mainstream, so the relative error tends to infinity as the mainstream is approached. However, for most of the temperature profile, the relative error is well within 1% and the absolute error in non-dimensional temperature is always < 0.3%.

Heat transfer relative error must be calculated separately for each mode of heat transfer. For conduction, the relative error is given by

$$\frac{\sigma q''_{cond}}{q''_{cond}} = \sqrt{\left(\frac{\Delta T_w}{(T_w - T_{bw})}\right)^2 + \left(\frac{\Delta T_{bw}}{(T_w - T_{bw})}\right)^2 + \left(\frac{\Delta t_w}{t_w}\right)^2 + \left(\frac{\Delta k}{k}\right)^2} \qquad (69)$$

In this case, the temperatures were not acquired with the same thermocouple. As such, the inherent systematic error cannot be cancelled out during the operation. Conservatively, the largest of the two errors between random and systematic is used for this calculation, and thus $\Delta T_w = \Delta T_{bw}$ = 1.1K. It is worth noting, however, that the thermocouples used for this calculation were at less than 0.5 K of each other before the experiment started. This suggests that the systematic error between them is actually < 1.1 K. Nevertheless, the more conservative estimate is provided here. As for errors in thermal conductivity of the plate, while no value was reported in the literature, the measurement techniques used to measure thermal conductivities of thermoplastics provide errors within 2% [81]. As such the error is assumed to be 2% of the reported literature value for the thermal conductivity of UDEL,

k = 0.26 W/mK. The plate thickness was measured with a caliper providing Δt_w = 0.1 mm. Overall, conductive heat transfer errors were on the order of 8% near the injection, and decreased to about 2% downstream.

In the case of radiative heat flux, there are several variables involved in the calculation. Absolute errors in emmisivities are assumed to be on the order of 0.01 based on the reported significant figures for these values in the literature and errors in view factors are assumed to be negligible. At each measurement location the total radiative exchange is composed of 3 contributions (plate to parallel window, plate to orthogonal window, plate to casing). Thus, the total error accounts for these contributions. For any of the three interactions between the plate and either window or the casing, the absolute error is given by (example shows plate to casing interaction)

$$\Delta q_{pc}'' = \sqrt{\left(\sigma\varepsilon_p F_{pc}(T_p^4 - T_c^4)\Delta\varepsilon_c\right)^2 + \left(\sigma\varepsilon_c F_{pc}(T_p^4 - T_c^4)\Delta\varepsilon p\right)^2 + \left(4\sigma\varepsilon_p F_{pc} T_p^3 \Delta T_p\right)^2 + \left(4\sigma\varepsilon_p F_{pc} T_c^3 \Delta T_c\right)^2} \quad (70)$$

Again, in this case the thermocouples used are all different and so the larger systematic error should be used. In this case, the reference condition before the experiment also showed that all the thermocouples involved in this calculation were within 0.5 K of each other.

The total error in the radiation estimate is given by equation 70. Modified as relative error it becomes

$$\frac{\Delta q''_{rad}}{q''_{rad}} = \sqrt{\left(\frac{\Delta q''_{pc}}{q''_{pc}+q''_{pw1}+q''_{pw2}}\right)^2 + \left(\frac{\Delta q''_{pw1}}{q''_{pc}+q''_{pw1}+q''_{pw2}}\right)^2 + \left(\frac{\Delta q''_{pw2}}{q''_{pc}+q''_{pw1}+q''_{pw2}}\right)^2} \quad (71)$$

Using the more conservative approach, radiative heat flux relative error is on the order of 4% and decreases with downstream location.

Finally, the error in convective heat flux is propagated as dictated by equation 67. Modifying equation 67 to express relative error, the error in convection becomes

$$\frac{\Delta q''_{conv}}{q''_{conv}} = \sqrt{\left(\frac{\Delta q''_{rad}}{q''_{rad}}\frac{q''_{rad}}{q''_{cond}-q''_{rad}}\right)^2 + \left(\frac{\Delta q''_{cond}}{q''_{cond}}\frac{q''_{cond}}{q''_{cond}-q''_{rad}}\right)^2} \qquad (72)$$

Thus, error in convective heat transfer is on the order of 7% and decreases with downstream distance.

With regards to location uncertainty, the gas temperatures are measured using a fine traverse rated to 0.01 mm. Downstream locations are dictated by machined holes in the test section, which have been manufactured with a tolerance of 0.0254 mm between consecutive holes.

2.5 Operating Procedure

Running a film cooling experiment is not trivial, and there are several challenges one may encounter during regular operation. Experience has also provided enough information about how measurements should be made in order to minimize errors and optimize run times. This section presents a summary of operating procedures for future reference, whether it be at the same facility, or a similar facility relying on similar principles and diagnostics.

2.5.1 Adiabatic tests

The standard operating procedure for a typical adiabatic case begins with preparing the experimental facility and diagnostics. The test section is cleaned and the wall surface paint is inspected and repainted as needed. Paint must dry overnight.

Seeding lines are inspected and unclogged as necessary to ensure a smooth operation during actual PIV measurements. On the day of the experiment, TiO_2 seeding is removed from the seeders, placed in a shallow baking pan and oven dried for at least an hour. This procedure removes moisture from the seeding and prevents caking and clogging of the lines during the experiment, as well as minimizing particle coalescence to guarantee a uniform particle size. The seeder is refilled just prior to the beginning of the experiment.

The PIV system is calibrated next. A calibration plate is placed at the location of interest. The camera is focused on the plate and adjusted until the required field of view is obtained. A calibration image is recorded and the system calculates the pixel/mm conversion factor. The camera is locked in place and the lens changed to autofocus to prevent accidental defocusing (the camera does not have autofocusing capabilities, so this adjustment disengages the manual focusing of the lens such that any disturbances will not have an impact on the mechanical workings on the lens). Next, the film flow is seeded and the laser sheet is adjusted in 3 axes until the particles are in focus. Once this occurs, the laser sheet is locked in place and the seeder is turned off. With this procedure, the camera plane and the laser sheet plane are parallel to each other and the laser plane is in focus with the same field of view as during calibrations. Further motion of the camera and laser sheet to cover the entire domain is achieved via a rail system such that the camera only translates in one plane parallel to the laser sheet without compromising focus or field of view (magnification) and so the original calibration image can be used throughout the entire experiment.

The microthermocouple is checked and adjusted as needed using an ice bath and a secondary thermocouple at room temperature as references. When the microthermocouple reads both reference temperatures to within 0.5 K, the calibration is satisfactory. A reference pitot tube to track the mainstream velocity is calibrated under quiescent flow conditions (zero velocity). The thermocouple array and DAQ are turned on to monitor all the temperatures which at this stage should read room temperature. The methane massflow controller is turned on while keeping the methane tanks closed. Once the massflow readout has stabilized at a value of zero, the wind tunnel is ready to start.

First, the film flow is established by opening the compressed air lines and setting a volumetric flowrate of 15-20 SCFM on the film flowmeter. The exhaust hood is turned on and the pitot tube is monitored until the freestream reaches steady conditions. The test section windows are carefully removed to prevent pressure buildup during ignition. Next, the fan is started at a low speed (~20 Hz). Finally, the methane tank is opened and the massflow adjusted in small increments. The spark plug igniter is switched on and the methane flow is slowly increased until ignition occurs, which is verified visually though the inspection ports as well as monitored by the array of thermocouples in the wind tunnel. The fan speed is increased to 40 Hz and the test section windows are secured in place with wing nuts to prevent leaks.

At this point one must iterate over the fan speed and methane flow rate to achieve the target mainstream temperature and velocity. These cannot be independently controlled although clearly the mainstream velocity is a strong function of the fan speed and the mainstream temperature a function of the methane flowrate.

Once the target values are achieved to within 10K and 1 m/s as reported by the mainstream thermocouple and pitot, the film flow is adjusted to the target velocity using flowrate-bulk velocity calculations. At this point, the system will be close to the target values but due to inherent errors in the pitot as well as in the bulk estimates, the targets must be refined. To do so, the flows are seeded and 10 PIV images are obtained and averaged. A velocity profile close to the inlet is extracted and checked against the expected target values of mainstream and coolant velocity. Adjustments are made as needed and the procedure is iterated until the target values are observed, usually to within 0.5 m/s. At this point, the wind tunnel is undisturbed for approximately 15 mins while monitored to achieve steady state.

Thermal measurements are performed first to prevent sebacate oil deposition from the film seeding on the wall to affect wall temperature measurements. The microthermocouple is carefully inserted into the test section, aligned and traversed towards the wall. Visual confirmation of the bead against the wall is obtained with the help of a strong light strategically aimed at the wall surface. Measurements are taken at 10 kHz and the thermocouple is traversed away from the wall to obtain the first profile. The procedure is repeated until all the profiles are completed while monitoring the global variables via pitot and thermocouples.

Once all thermal measurements are satisfactory, PIV measurements are taken. The film is seeded first while acquiring test images. Once seeding density is optimal, the mainstream seeder is slowly opened and adjusted. Upon confirmation of mainstream seeding observations, the seeding density is adjusted to match that of the film as best as possible. At this point, 500 PIV images are obtained at 5 Hz. A random

image near the last 30% of the samples is processed to verify that the algorithm provides a credible measurement with few dropouts. The windows are removed and replaced with plugs of the same size to prevent strong entrainment into the test section as this disturbs the mainstream flow, essentially slowing it down and raising its temperature significantly. The windows are wiped clean, replaced on the test section and sealed again. The camera is translated downstream such that an overlap of ~ 5 mm exists between the previous field of view and the new one. The seeding start up procedure is repeated and the laser sheet is adjusted as necessary to properly illuminate the new region. The image acquisition is repeated until the full domain of interest has been covered. A snapshot of the reference temperatures and pitot velocity is captured before each image set.

Once all relevant data has been acquired, the experiment is shut down by closing the methane flow and confirming flame extinction visually as well as by a drop in the reported thermocouple temperatures (burner and mainstream). The fan speed is increased to enhance convective cooling of the ceramic saddles. After about 15-20 mins or when the mainstream temperature is in the 300-310 K range, the fan is turned off and the remaining cool down is sustained by the exhaust hood fan. The film flow is shut off and the experimental station is cleaned up. PIV data post processing is started immediately.

2.5.2 Non-adiabatic tests

In the case of non-adiabatic experiments, the overall procedure is nearly identical with a few added elements. Approximately 2-3 hours before startup, the reservoir tank is filled with distilled water and the chiller is started and set at a target temperature of 283 K. A thermocouple is used to monitor the water temperature until

the desired target is reached. At this point, the sump pump is engaged and the water starts circulating from the tank to the backside wall water jacket and returned to the tank. The chiller remains on, working in parallel.

After the wind tunnel is started, an additional set of temperatures is monitored, namely the casing temperatures and the backside wall temperatures. Backside wall temperatures should be at least 10 K below room temperature before the experiment starts. A snapshot of all temperatures must be taken during each hot side wall temperature measurement in order to derive heat transfer values. During normal shut off procedures, the chiller and sump pump are shut off along with the main fan. If the wind tunnel will not be run for an extend period of time (> 1 week) it is advisable to completely flush the water in the system by circulating the water from tank to water jacket but dumping the return flow.

Chapter 3: Results and analysis

In this section, the experimental results of the work are presented and analyzed. the inlet characterization is presented first as one of the main contributions of this work is to provide this information in a complete and comprehensive manner not only to understand injection conditions in detail, but also for their importance to modelers. Wall measurements are then presented in order to understand film cooling performance in both adiabatic and non-adiabatic cases. Kinematics and thermal mixing are then discussed in detail in order to understand the flowfield behavior and its relation to the observed wall measurements. A special effort is made to not only understand the physical aspects governing the observations, but also to present data in a way that is amenable for direct comparison to numerical results either averaged (RANS) or time resolved (LES).

3.1 Inlet characterization

Special attention was placed on kinematic and thermal inlet characterization, not only because of the importance of this information to support computational modeling efforts, but also because it is the inlet configuration and inlet parameters what dictates the physics that govern film cooling decay in the near-injection region. It should be noted that while this information is of utmost importance to guarantee the accuracy of a numerical simulation (i.e., having poor quality or missing inlet data will undoubtedly lead to erroneous results), inlet experimental data cannot in general be fed directly into a simulation without considerable effort from the modelers.

Figure 36 shows the near-injection region for the three velocity ratios qualitatively through flow visualization and quantitatively as a single instantaneous

Reynolds decomposed velocity field. Inlet characteristics were extracted close to the slot ($x/s \leq 0.1$ for kinematic data, $x/s \leq 0.5$ for thermal data). The locations of the inlet measurements are shown with respect to the slot height and louver exit. Contours of the wall normal velocity fluctuation, v', are used in addition to the fluctuating velocity vector field in order to better identify roller structures since this fluctuating velocity component is ultimately responsible for the

Flow visualization of this near-injection region highlights the immediate establishment of roller structures in both the wall-wake (a) and wall-jet (c) cases, while the minimum shear case (b) does not exhibit any particular structure shape. Inspection of the observed structures reveals counter-clockwise rotation for the wall-jet and clockwise directionality for the wall-wake. Reynolds decomposition of a single instantaneous vector field reveals these structures quantitatively. Their rotation direction is confirmed by the observation of vector orientation, and their relative strength is shown by the magnitude of the v' component relative to the convective velocity. Structures seem to be stronger in both the wall-wake and wall-jet cases, and relatively weaker in the min-shear case. These structures are also observed to be well aligned with the location of the louver at $y/s = 1$ since this is where the initial shear between the streams is set up. Structures are also on the order of one slot height in diameter and separation, while it can also be observed that smaller structures of opposite rotation direction tend to set up between the main structures, suggesting that the presence of counter-rotating pairs begins very close to the injection region. These observations suggest that mixing is established immediately downstream of the louver

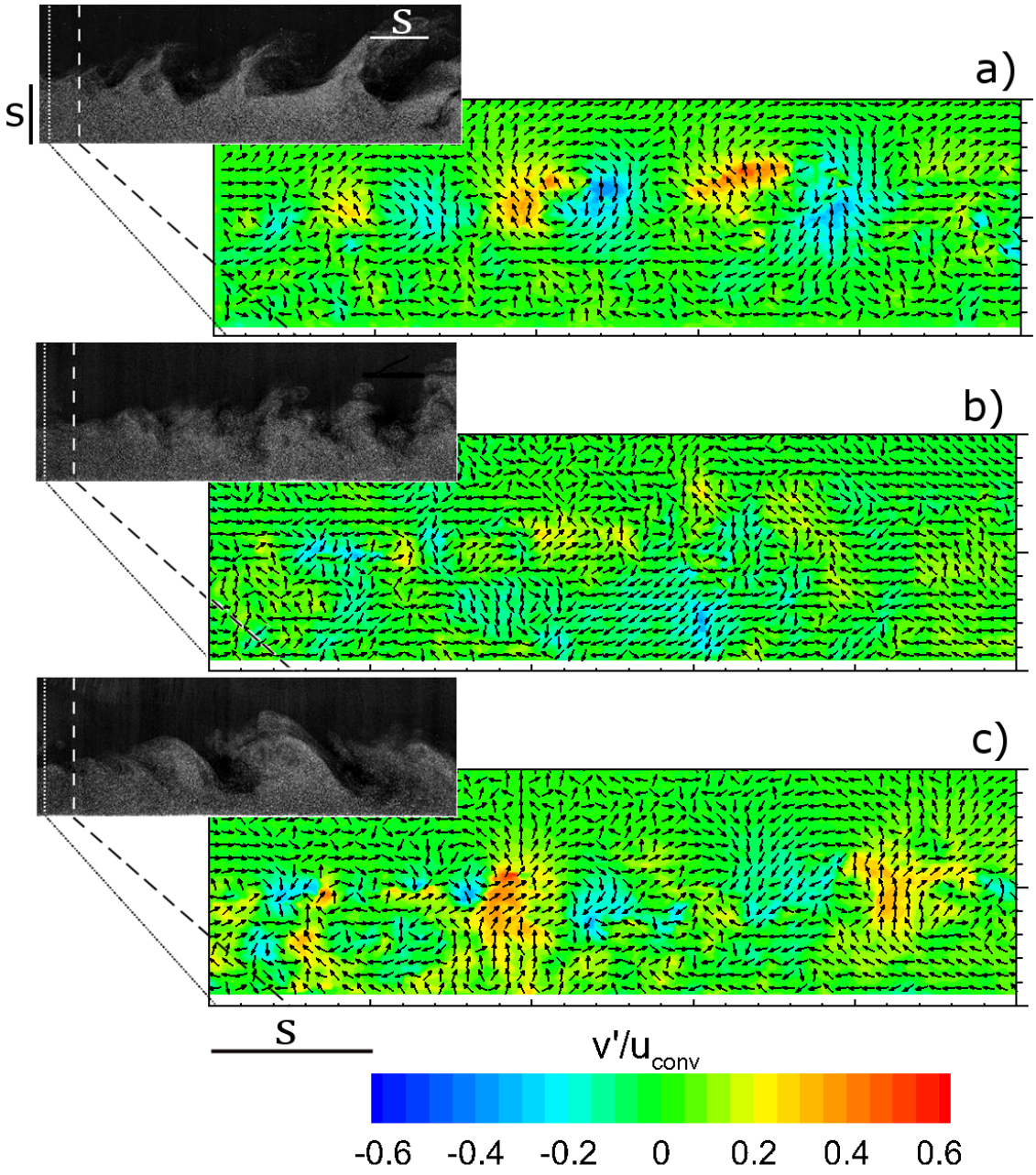

Figure 36. General overview of film cooling in the near injection region (x/s < 5) for a) wall-wake, b) min-shear, c) wall-jet. ••• shows location of kinematic inlet measurements, - - - shows location of thermal inlet measurements. Flow visualization highlights the general structure of the flow for the 3 distinct velocity ratios, while contours and vectors provide quantitative information about the initial mixing strength and transport of fluid between the two streams. Contours have been normalized by the convective velocity $u_{conv} = 0.5(u_c + u_\infty)$ in order to provide an additional layer of comparison among the three distinct velocity ratios.

exit, albeit with significant differences in strength and directionality depending on the blowing ratio.

Figure 37 shows the corresponding inlet profiles of (a) velocity, (b) temperature, (c) u_{rms}, and (d) v_{rms}. Only adiabatic inlets are shown for conciseness, but corresponding information has been obtained for the non-adiabatic inlets. Analysis of non-adiabatic data has shown that adiabatic kinematic profiles can be scaled to match non-adiabatic profiles to account for the slight discrepancy in blowing ratios.

For the kinematic inlets, velocities have been scaled by two distinct references while the wall-normal coordinate has been scaled by the slot height. The film flows are similar when scaled by the slot height, s, and the coolant velocity, u_c, and closely resemble fully developed turbulent channel flow. A slight asymmetry is noticed, which can be attributed to 3-D effects within the louver. The mainstream has been scaled by the mainstream velocity, u_∞, and once again mainstream inlets are very similar. The fact that both film and mainstream flows are similar after scaling, despite the distinct differences in velocity ratios suggests that these scaling parameters are appropriate choices for comparison between inlet experimental data and precursor simulations (which are typically run to generate inlet profiles for actual film cooling simulations). Furthermore, the fact that all profiles collapse despite the significantly different shear scenarios, suggests that a universal non-dimensional profile shape may be used to define kinematic inlets in a simulation, regardless of shear condition. This single treatment of the mean inlet profile can lead to great simplification in inlet

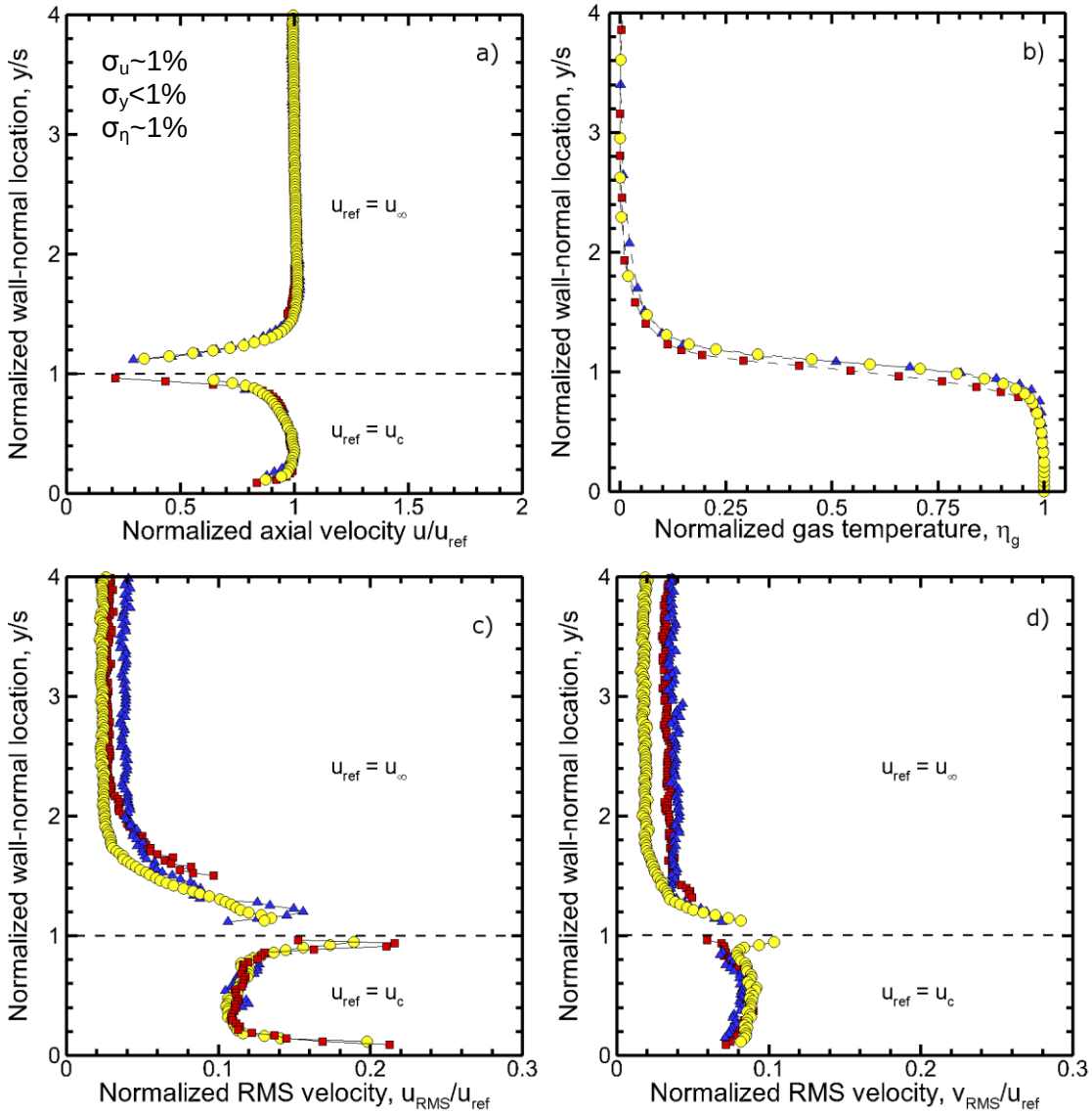

Figure 37. a) Mean axial velocity inlets, b) mean thermal inlets, c) turbulent u_{RMS} inlet, d) turbulent v_{RMS} inlet. wall-wake, min-shear, wall-jet. Reference velocities can be found in Table 6.

specification for a modeler, although special care must be taken in order to ensure that the non-dimensional inlet respects the original shear scenario. Turbulent inlet information has also been scaled with respect to the slot height and the corresponding velocities (u_c, u_∞). For the range of velocities observed, the relative turbulence intensity in both the coolant and the mainstream is seen to be nearly identical among

all cases (with film turbulent intensity being larger than that of the mainstream). This similarity in turbulence intensity suggests not only that all coolant inlets are indeed turbulent, despite the variation in Reynolds number, but it also suggests that (for this work) it is shear and not the initial turbulence of the streams what leads to different blowing ratio performance. This does not imply that turbulent intensity does not play a role in the subsequent mixing and decay of the film, but rather that, all things being equal, the initial shear will play a significant role in the observed film cooling performance. This is an important point, particularly when it comes to simulations where not capturing the initial turbulence intensity will typically result in correct predictions of the adiabatic effectiveness dependence on blowing ratio, but the actual adiabatic effectiveness *values* will not be accurately predicted.

With respect to the relative intensity of the two measured components, u_{rms} is slightly larger than v_{rms} suggesting a slight anisotropy at the inlet for both coolant and mainstream. This initial anisotropy may have an impact on the subsequent performance, highlighting the importance of having this information readily available. As a side note, non-adiabatic inlets behave in a similar fashion and have nearly identical non-dimensional values. Although non-adiabatic inlets are not shown for conciseness, the corresponding scaling parameters (s, u_c, u_∞) are reported in the test matrix.

Thermal inlets show nearly identical behavior for all cases, showing that the slot height, s, and the non-dimensional temperature, η_g, are valid scaling parameters for the gas temperatures. Furthermore, the thermal similarity at the inlet among such different shear cases suggests that observed differences downstream are solely due to

the differences in blowing ratios through the differences in velocity ratios. The striking similarity among all inlets when scaled by the appropriate parameters also suggests that, at least for the range of conditions in this study, there is a universal inlet shape for each of the kinematic and thermal quantities of interest. This inlet similarity can be of great help for modelers as it simplifies the approach to compare simulation to experimental inlet profiles since only a single reference non-dimensional profile is required even for widely distinct blowing ratios.

3.2 Wall measurements and heat flux

Wall temperature measurements can be interpreted in multiple ways, each one providing insight into different aspects of the problem. In the adiabatic cases, the adiabatic wall effectiveness is the de facto standard to characterize film cooling performance. The decay in adiabatic effectiveness with downstream distance for different blowing ratios highlights the relative performance of the different shear scenarios. In non-adiabatic cases, wall temperatures can be interpreted in two ways. A non-adiabatic effectiveness can be defined, which effectively emphasizes the benefit of backside cooling in addition to film cooling. This metric can also be used to observe the relative decay of the film under non-adiabatic conditions. Unlike the adiabatic cases, non-adiabatic performance can be expected to be strongly dependent on actual backside boundary conditions, such that these results are not universal for every system (i.e. the same flowfield with stronger backside cooling will lead to different values of non-adiabatic effectiveness). Despite this dependence of the non-adiabatic effectiveness on boundary conditions, having this non-adiabatic data is valuable to understand the relative performances of different blowing ratios under

more realistic conditions, and is also of relevance to modelers as they can readily implement the same experimental conditions..

The wall temperatures can also be used to obtain heat flux, a more relevant metric of what actually occurs in a realistic propulsion system. Expressed as a heat flux reduction fraction, one can observe what the film cooling system buys in addition to the backside cooling. Similarly to non-adiabatic effectiveness, these heat flux results are not independent of backside cooling conditions, but also provide enough insight and are relevant to modelers who can replicate the conditions in order to test a more complex and realistic simulation.

Figure 38 (a) shows the adiabatic and non-adiabatic effectiveness vs. downstream distance, while Figure 38 (b) shows the corresponding heat flux reduction. It is worth noting that while similar, corresponding shear cases do not have identical inlet conditions so it is best to analyze adiabatic and non-adiabatic results independently. In terms of adiabatic effectiveness, near the injection, all cases perform comparably with immediate effectiveness decay captured in all cases. The addition of backside cooling manifests itself in a non-adiabatic effectiveness value > 1.0 at the inlet where the backside coolant has cooled the wall below the temperature of the film. Further downstream, the cases diverge as the performance is impacted by the ongoing mixing. The minimum shear outperforms the other cases, followed by the wall-jet and finally the wall-wake. This last case shows a very rapid drop-off in effectiveness at $x/s > 10$ with a final value that falls below the accepted threshold of $\eta = 0.75$.

In terms of heat flux reduction, the trends are very similar to those seen in the adiabatic cases despite being obtained under non-adiabatic conditions, suggesting that the fluid dynamics aspect of the problem has a significant impact on the wall

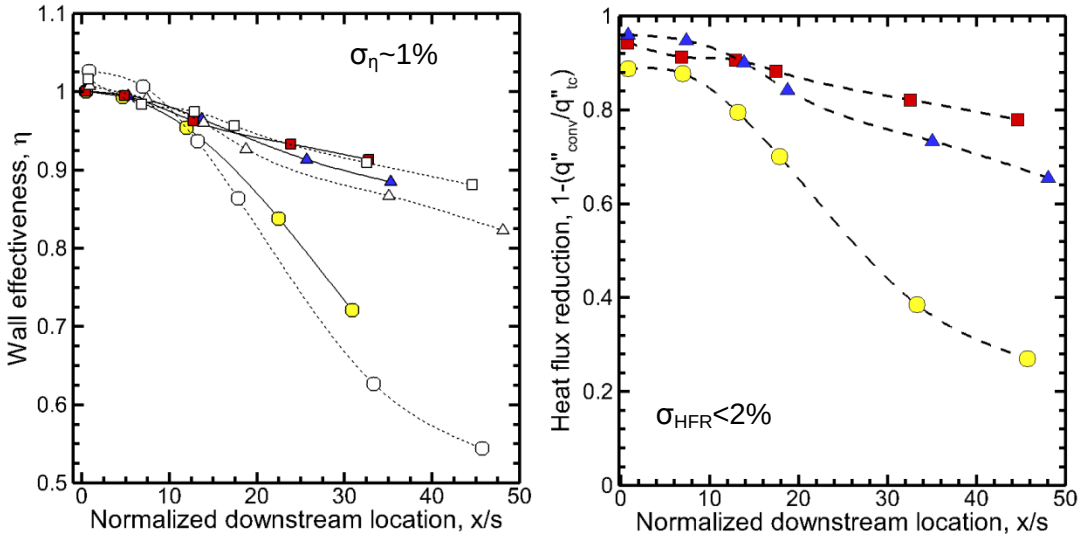

Figure 38. a) Adiabatic (filled) and non-adiabatic (open) wall effectiveness, b) heat flux reduction. ● wall-wake, ■ min-shear, ▲ wall-jet

temperature behavior regardless of the boundary condition (the actual values will be impacted by backside cooling, but for similar backside conditions, the relative non-adiabatic performance will reflect that of adiabatic conditions). Once again, the minimum shear shows a greater reduction in heat flux compared to the other cases, while the wall-wake case rapidly loses its performance again at $x/s > 10$. Despite having similar reference conditions T_∞ and U_∞, the wall-wake near the inlet already offers less of a heat flux reduction compared to the min-shear case. This initially lower reduction could be explained by the fact that the wall-wake film has the lowest velocity, U_c, of all cases. This lower injection velocity may allow the wall-wake to preheat due to conduction across the louver to a larger extent than the faster moving

min-shear and wall-jet films. This preheating hypothesis is also supported by the observed lower non-adiabatic effectiveness of the wall-wake. Contrastingly, despite having different reference conditions T_∞ and U_∞, the min-shear and wall-jet have similar heat flux reductions at the inlet (while having similar coolant conditions U_c and T_c). These observations suggest that in the near-injection region, the heat flux performance is clearly dominated by the film inlet conditions alone, while the resulting downstream performance is the result of the more complex film-mainstream interactions.

3.3 Flow kinematics

The complex nature of film cooling flows encompasses not only the thermal aspect of the flowfield, but also the kinematics, both of which are closely coupled. In order to capture film cooling performance adequately, one must take into account not only how the mean kinematic field behaves, but also the behavior of the turbulent fluctuation field. Furthermore, identifying coherent kinematic structures can reveal significant information about the location, size and strength of eddies. This information can provide insight into the mixing processes, as well as allowing for a more complete comparison to spatially and time resolved simulations such as LES.

3.3.1 Kinematic law of the wall scaling

In terms of near-wall accuracy, the Clauser method was applied to the kinematic data, revealing the existence of a log-linear region for all profiles. This data was then fit to follow the classic law of the wall with good agreement, as seen in Figure 39. The data shows that near-wall data points are valid as close as y^+ =30, and the linear layer is observed up to y^+ = 100. The existence of this log-linear layer not

only allows one to understand the near-wall resolution of the measurements, but also suggests that modelers may employ wall models based on classic law of the wall approaches in order to relax the strict near-wall grid spacing typically associated with this type of flows. This should allow for a significant improvement in computational time and resources, while maintaining fidelity to the actual flow physics.

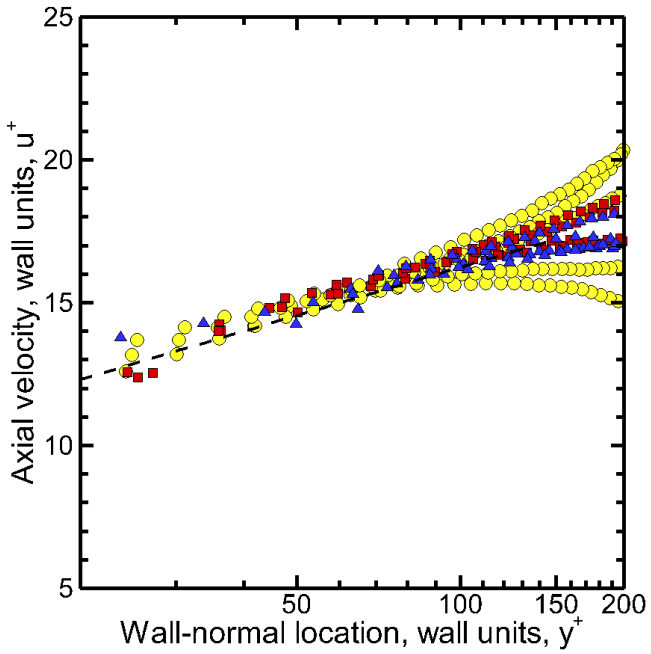

Figure 39. Clauser method applied to experimental PIV data. wall-wake, min-shear, wall-jet, - - - classic law of the wall

3.3.2 Kinematic flow development

Figure 40 (a) shows the mean velocity profiles for all adiabatic cases, while Figure 40 (b) shows the corresponding Reynolds shear stresses. Comparing the mean velocity profiles allows one to understand how momentum transport impacts the changes in profile shape as the flow moves downstream. The min-shear case undergoes very little change, while the wall-jet and wall-wake evolve in opposite directions. The wall-jet spreads away from the wall, the peak velocity location moves

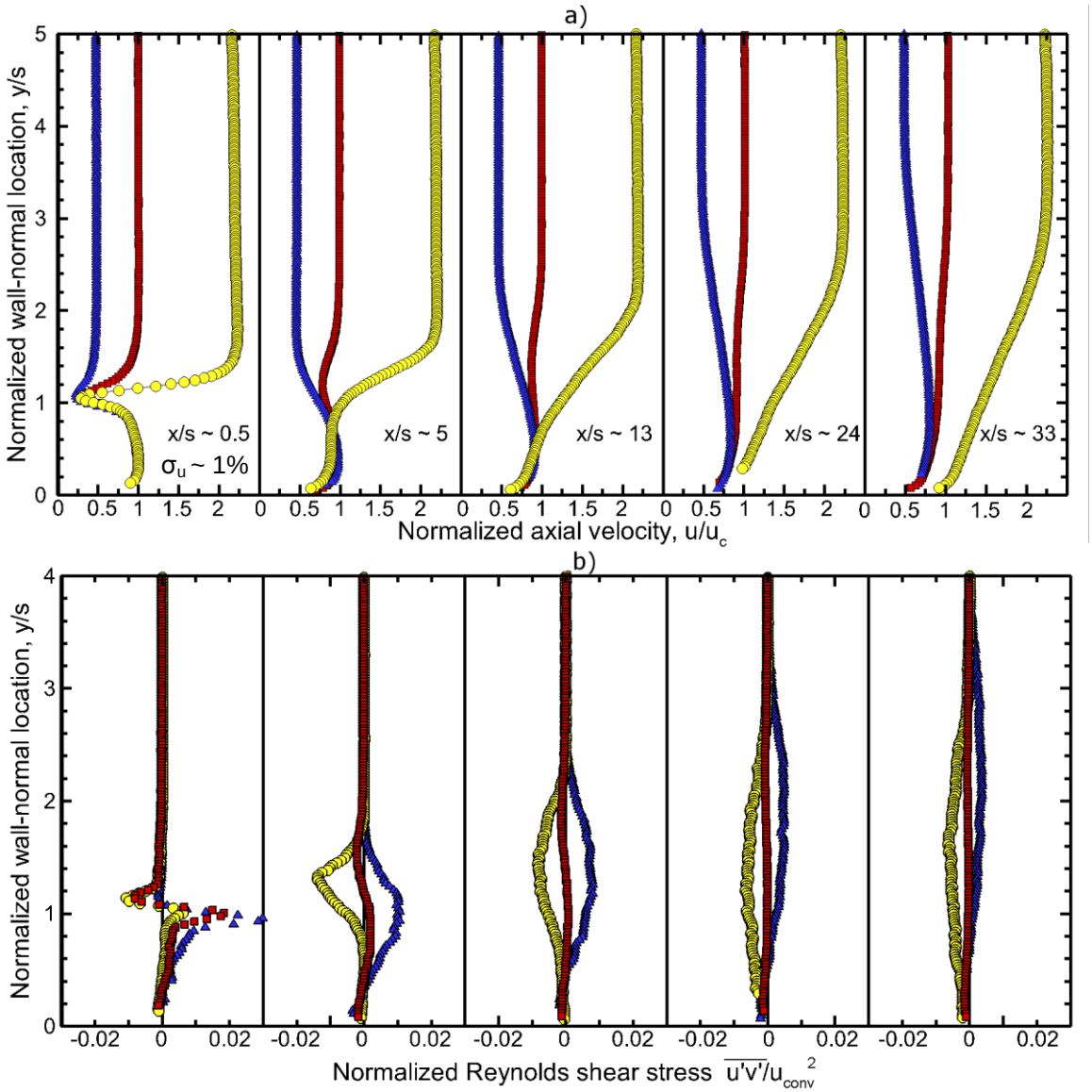

Figure 40. a) Mean axial velocity profile development, b) Reynolds shear stress profile development. wall-wake, min-shear, wall-jet (adiabatic cases).

away from the wall and the peak velocity decreases, which is consistent with wall-jet observations in the literature. Nevertheless, the wall-jet still retains a history of its original shape downstream. The wall-wake, on the other hand, undergoes very rapid transformations. The mainstream moves towards the wall, the velocity deficit is quickly compensated, and downstream the wall-wake retains very little history of its

original shape as it more closely starts to resemble a turbulent boundary layer profile. Because turbulent momentum transport is responsible for these changes and mixing effects seem to be stronger in the wall-wake case, it is important to investigate turbulent fluctuations closely.

Close to the wall ($y^+ < 100$), all the cases exhibit negative Reynolds shear stresses, as this is the expected behavior of any boundary layer. At some point away from the wall, these behaviors start to diverge depending on the shear case. The min-shear case exhibits very weak Reynolds stresses, and these quickly dampen to nearly zero downstream, suggesting that the active turbulent mechanisms responsible for mixing in this case are relatively weak. The mixing events simply attempt to balance the effects of the wake induced by the louver and they quickly restore equilibrium without strongly mixing the two streams. This evidence of weak mixing is consistent with the increased thermal performance of this case in terms of adiabatic effectiveness and heat flux reduction.

In the wall-jet case, Reynolds stresses transition from negative to positive values due to the mean velocity gradient, $\partial U/\partial y$, changing sign once the peak velocity has been reached. Downstream, the peak in Reynolds stress moves away from the wall, the profile widens (covering a larger wall normal direction) while the peak stress is reduced. These profile features reiterate that the wall-jet spreads away from the wall while mixing, and that structures are growing while the local mixing strength is reduced. This general motion away from the wall counteracts the influx of hot mainstream flow towards the wall despite the ongoing mixing.

The wall-wake exhibits the opposite trends. Reynolds stresses are always negative or zero since $\partial U/\partial y$ is always ≥ 0 for this case. The peak Reynolds stress moves towards the wall, while the general trend of peak reduction and wall normal spread are maintained due to dissipation. However, one can see that having much larger Reynolds stress magnitudes near the wall means not only that the mainstream flow is rushing towards the wall, but also that a significant portion of the active mixing occurs near the wall which further contributes to the rapid decay of the film in this case. Thus, kinematic information shows that film decay is highly governed by the preferred flow spread direction as well as the relative mixing strength near the wall.

3.3.3 Coherent structure detection

As explained in Chapter 2, the global 2-D nature of PIV data allows for the detection of flow features such as coherent structures/rollers. The detection scheme was applied to the very near-field region ($x/s < 5$) as this is the region where rollers are initially set up and are therefore more likely to be detected by the algorithm. Each shear case was run through the algorithm and detected structures for each shear case were separated into counter-clockwise motion and clockwise motion. As one can recall from section 3.1, coherent structures were observed with flow visualization as well as from Reynolds decomposition, and the extreme shear cases had preferred rotational directionality while the min-shear case did not exhibit a preference.

As part of the coherent structure detection procedure, the (x, y) coordinates for the centroid of each detected structure are obtained. The spatial domain is then divided into 64 x 64 cells and a 2-D PDF is generated by counting the number of structures whose centroid is located within each cell.

Figure 41 shows the 2-D PDF heatmaps centroid location for each shear case. The shading corresponds to the probability between 0 and 1 that a structure centroid has been detected within the 2-D grid cell. These heatmaps confirm the qualitative observation that wall-wake structures exhibit clockwise rotation (as exhibited by the number of detected clockwise-rotating structures vs. counter-clockwise-rotating), while the wall-jet exhibits the opposite behavior. Interestingly, the min-shear exhibits almost an equal split between rotation directions, with a slight bias towards clockwise rotation. The 2-D heatmaps also quantitatively show how most coherent structures are set up at the louver height and within the first 2 slot heights. Further downstream, coherent structure centroid locations spread above and below the louver, consistent with the spread of the mixing layer. Wall-wake structures seem to be more constrained in their spread and more concentrated, while wall-jet structures are seen to be more distributed in space. Min-shear structures exhibit interesting behavior. Conter-clockwise structures tend to lie below the louver and in the coolant stream, while clockwise structures lie above the louver. This is consistent with the lack of preferred directionality and is most likely an effect of the louver wake and the slight deviation from the ideal velocity ratio of unity. Comparatively, roughly the same amount of structures were detected for all cases (including the total of clockwise and counter-clockwise rotating structures, about 2000 structures over the entire dataset of 500 vector fields, or roughly 4 structures/velocity field).

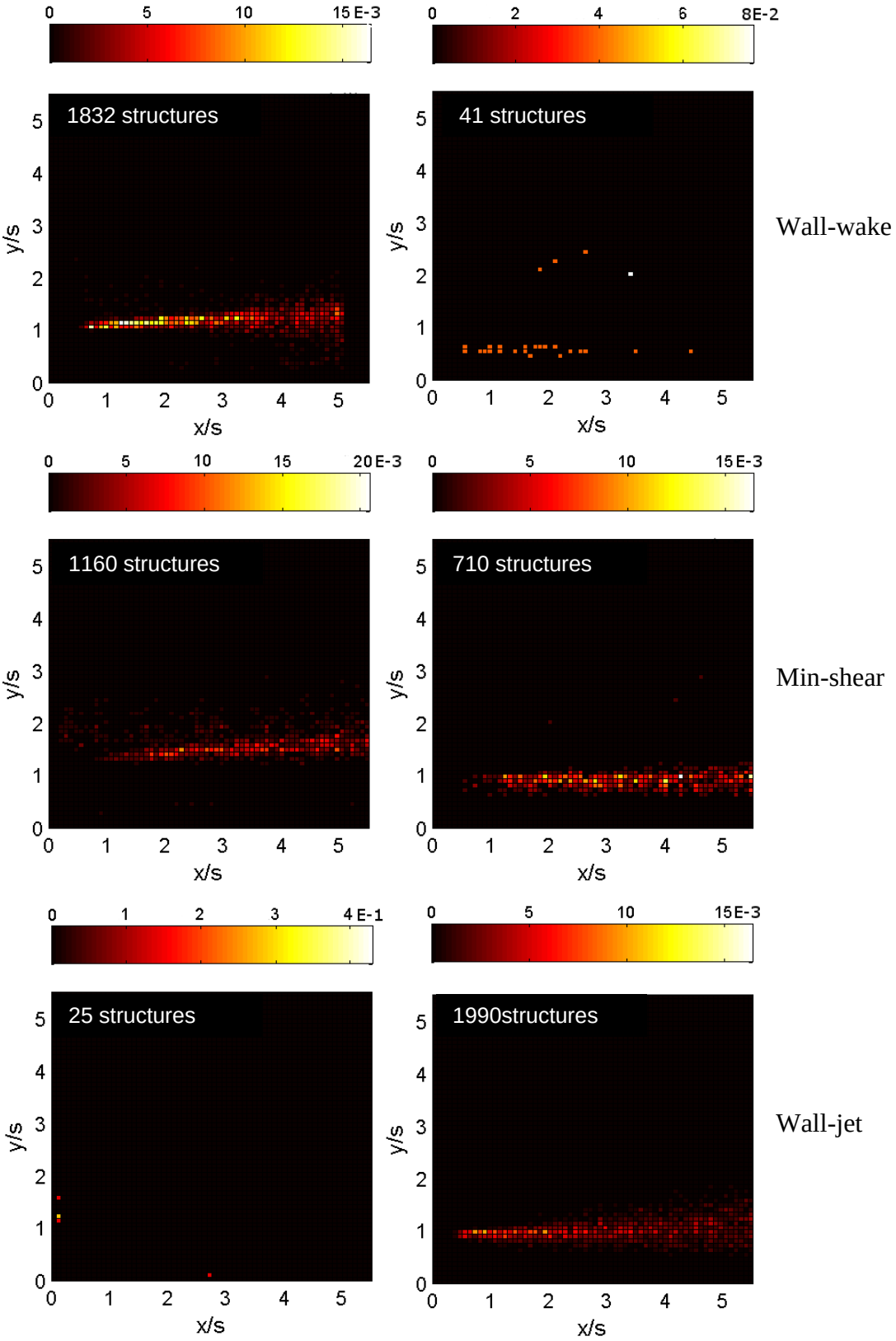

Figure 41. Heatmaps of centroid locations. Left column is for clockwise structures, right column for counterclockwise structures.

This first step of the algorithm provides relevant qualitative and quantitative data, and comparison to LES simulations should provide very relevant insight as to the model's ability to detect structures in the same locations and with the same frequency of occurrence (i.e. matching PDFs).

Another important parameter obtained from the structure detection algorithm is the size of the structure. While the detected structures are not perfectly circular, an equivalent diameter is obtained from the detected area of the structure (that is, the diameter that a circular structure would have if its area matched the area of the structure). The diameter distribution can then be analyzed for the 3 shear cases. Due to the dominant directionality in the wall-wake and wall-jet cases, only their dominant scenarios will be analyzed from here on, while both directions will be analyzed for the min-shear case.

Figure 42 shows the comparison of the diameter distributions (in slot heights) for the wall-wake and wall-jet cases. Although the spatial filter for the detection algorithm was on the order of 1 slot height as indicated by observation of Reynolds decomposed fields as well as from inspection of integral length scales, the resulting structures are seen to be smaller than 1 slot height. This could be explained by the fact that the algorithm defines vortex cores in a very specific way, and, while a structure may seem larger, only the smaller vortex core fits the definition used for its detection. This was observed during algorithm testing, where the prescribed core was accurately detected, yet the flowfield itself retained vortex features well outside the core. It is worth noting that both distributions are similar, with both exhibiting similar mean diameters (D_{mean} = 0.34 and 0.35 respectively). This is consistent with the fact

that the structures are strongly dependent on the slot height and the initial shear magnitude, both of which are comparable between the cases.

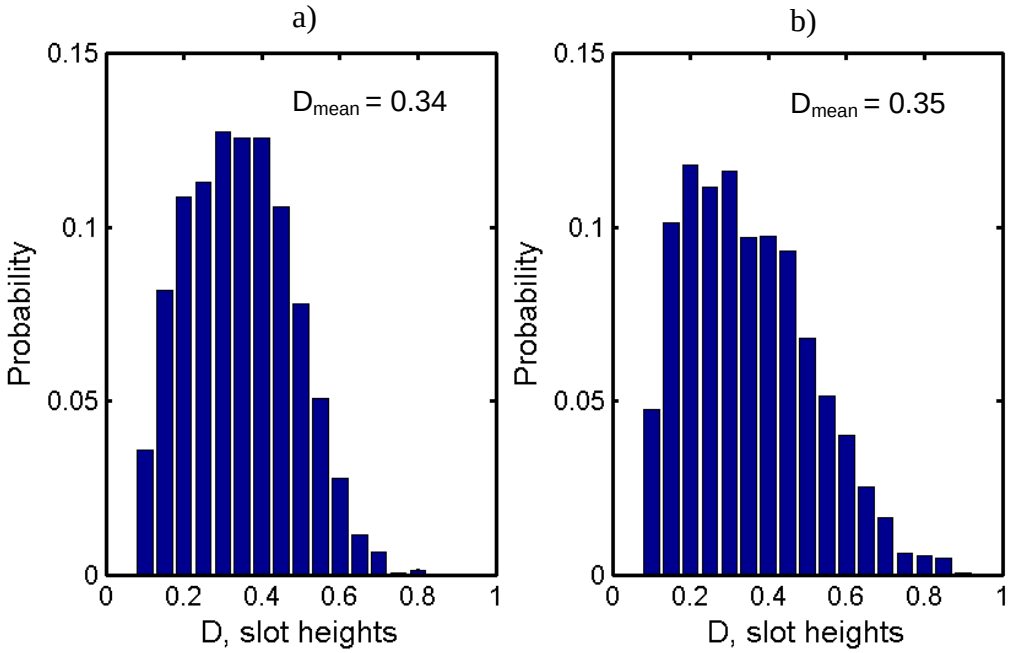

Figure 42. Diameter distribution for detected coherent structures. a) Wall-wake, b) wall-jet.

Figure 43 shows the diameter distributions for the min-shear case. In this case, one can see that the structures are smaller than the other shear cases (D_{mean} = 0.23 and 0.27), and the size distribution does not vary greatly between positive and negative rotating structures. The smaller structures are consistent with the weaker mixing observed in the min-shear case.

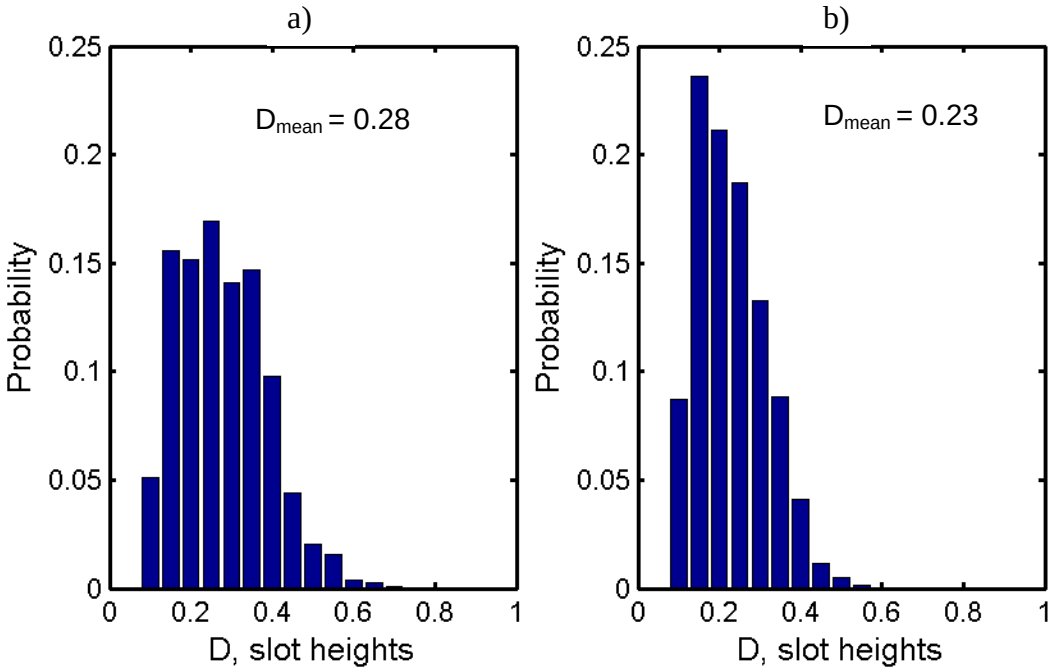

Figure 43. Diameter distribution for detected coherent structures. a) Min-shear clockwise, b) Min-shear counter-clockwise.

The third important parameter regarding coherent structure characterization is the strength of the structure. As explained in Chapter 2, the strength of the structure is defined in this work as the average 2-D turbulent kinetic energy enclosed by a structure (with the kinetic energy defined from spatial decomposition of velocity, not Reynolds decomposition). The resulting distributions for the wall-wake and the wall-jet are shown in Figure 44.

In this case, the strength distributions show some interesting differences. While the mean strengths are of the same order, the wall-wake exhibits relatively stronger structures. This is consistent with the observation that the wall-wake is the worst performing case due to rapid mixing near the wall. the distribution also shows that, while the wall-wake exhibits a few occasionally strong structures, most of the

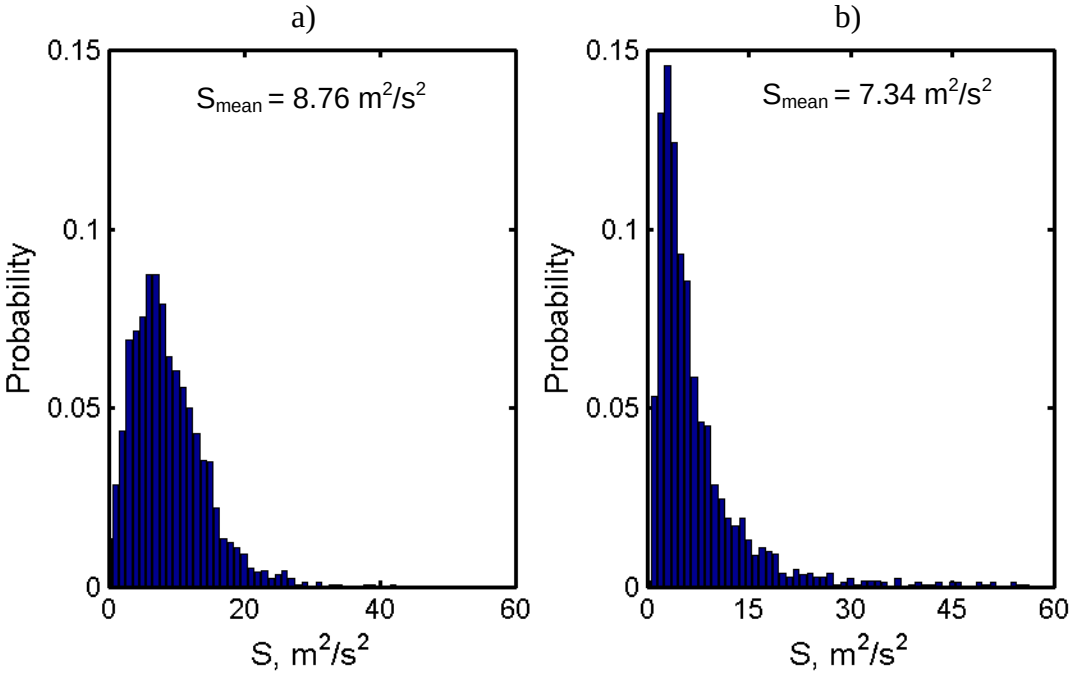

Figure 44. Strength distribution of detected coherent structures. a) Wall-wake, b) Wall-jet.

distribution is narrow and a considerable amount of structures are consistently within the mean value, whereas the wall-jet exhibits a wider distribution, suggesting that coherent structures in this case tend to occur over a wider range of strengths.

Figure 45 shows the corresponding strengths for the min-shear (using identical bin widths as the distributions for the other cases). Consistently with other observations, min-shear structures are considerably weaker (by about a factor of 3) than the extreme shear counterparts. The distributions are even narrower and the mode concentrates about 30% of all structures, showing that the structures tend to be very similar in strength as compared to the other shear cases. No strong outliers were detected at all. Mixing in the min-shear case is characterized by smaller, weaker structures and this leads to its overall better performance.

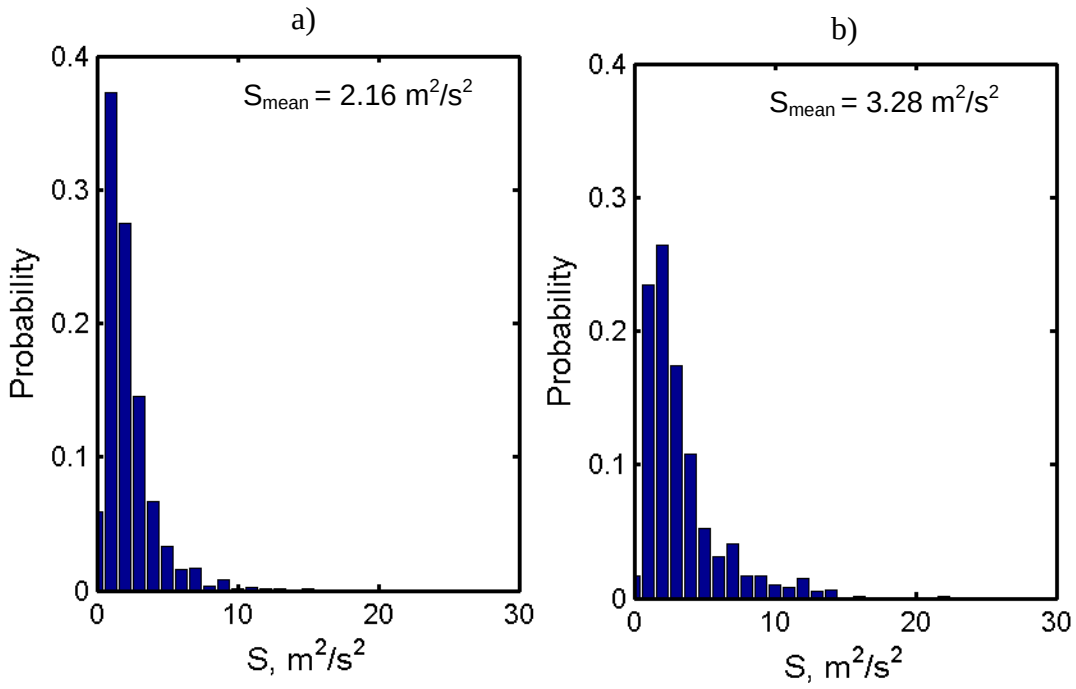

Figure 45. Strength distribution of detected coherent structures. a) Min-shear clockwise, b) Min-shear sounter-clockwise.

A final parameter of interest for the coherent structures is quantifying the convective velocities of the structures. By obtaining the velocity of the centroid of the structure, one can identify how fast these structures move relative to the injection velocities of the mainstream and coolant streams. Figure 46 shows the convective axial velocities for the wall-wake and wall-wake while Figure 47 shows the convective wall-normal velocity.

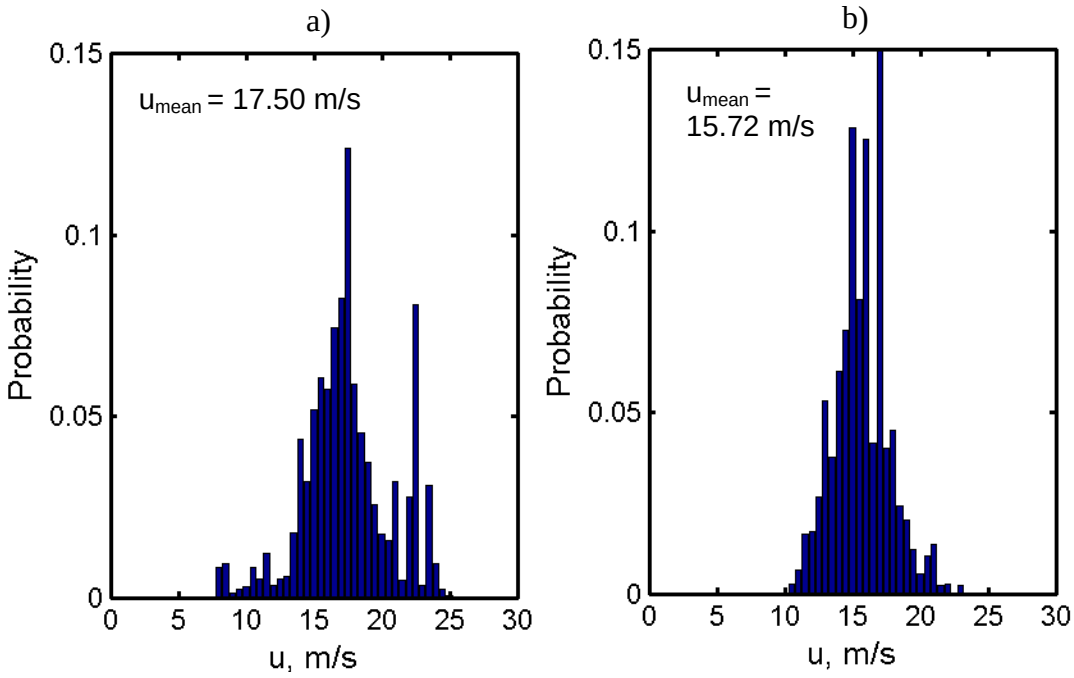

Figure 46. Axial velocity distribution of detected coherent structures. a) Wall-wake. b) Wall-jet.

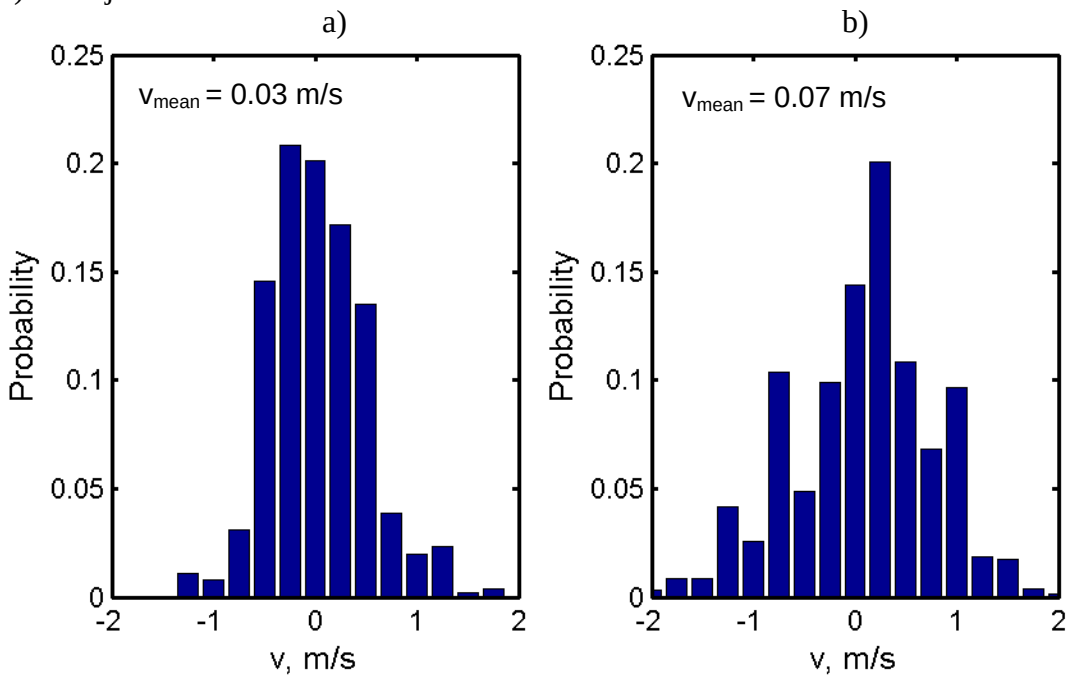

Figure 47. Wall-normal velocity distribution of detected coherent structures. a) Wall-wake. b) Wall-jet.

The axial velocity distributions show some slight differences. For the wall-wake, the behavior is slightly bimodal, with a secondary peak corresponding to velocities above the mean. However, the distribution is slightly wider than the wall-wake. Overall, the mean axial velocities correlate favorably with the convective velocities defined in the test matrix, not only being very close in value, but also preserving the trend where the wall-wake convective velocity is slightly higher than that of the wall-jet. This suggests that the convective velocity of the system has an impact on the mean convective behavior of the coherent structures. The wall-normal behavior of both cases is quite similar, with the range of velocities being constrained, but exhibiting both positive and negative velocities. This shows that structures are continuously moving towards and away from the wall, contributing to the mixing of the streams and the film decay. However, the net motion is very close to zero, such that there is no preferred wall-normal motion of the coherent structures, at least within the inspected region.

Figure 48 shows the axial velocity distributions for the min-shear while Figure 49 shows the wall-normal velocity distributions. The axial velocity distributions are very similar with respect to each other, but are noticeably narrower than the extreme shear counterparts. Additionally, the mean values are higher, which is also reflected in the convective velocity of the min-shear being the highest of all 3 cases as seen in the test matrix. The fact that this trend holds for all cases shows that the detection algorithm tracks well with respect to global inlet parameters. The wall-normal velocity distributions are also very similar with respect to each other, but the mean values are slightly higher than the other cases. While still small in value, they are

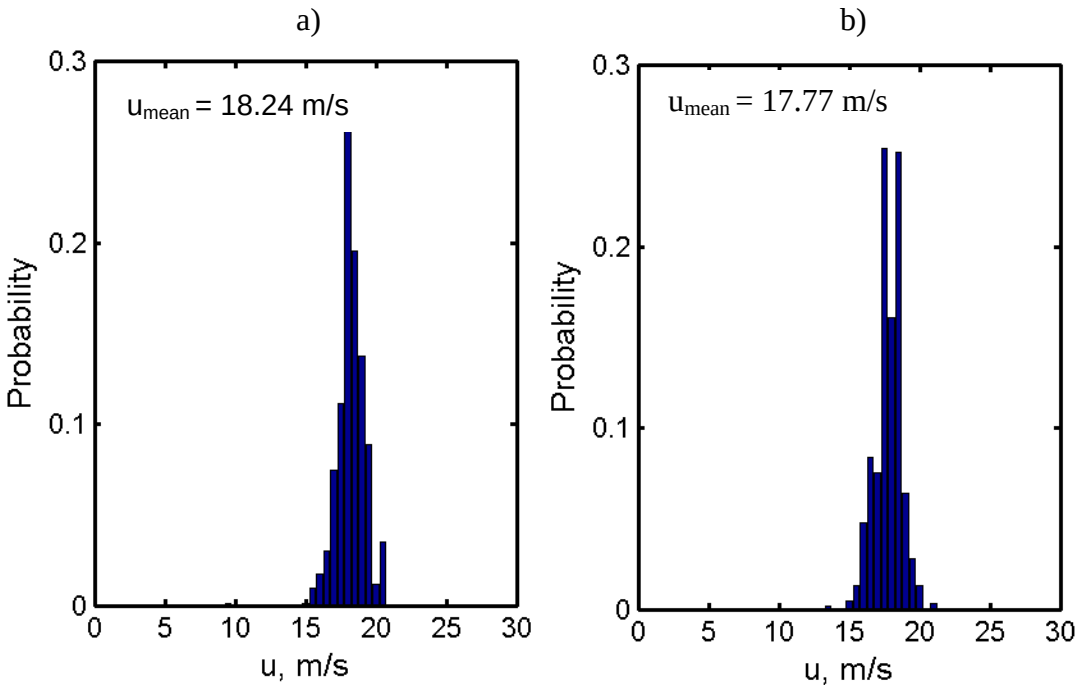

Figure 48. Axial velocity distribution of detected coherent structures. a) Min-shear clockwise. b) Min-shear counter-clockwise.

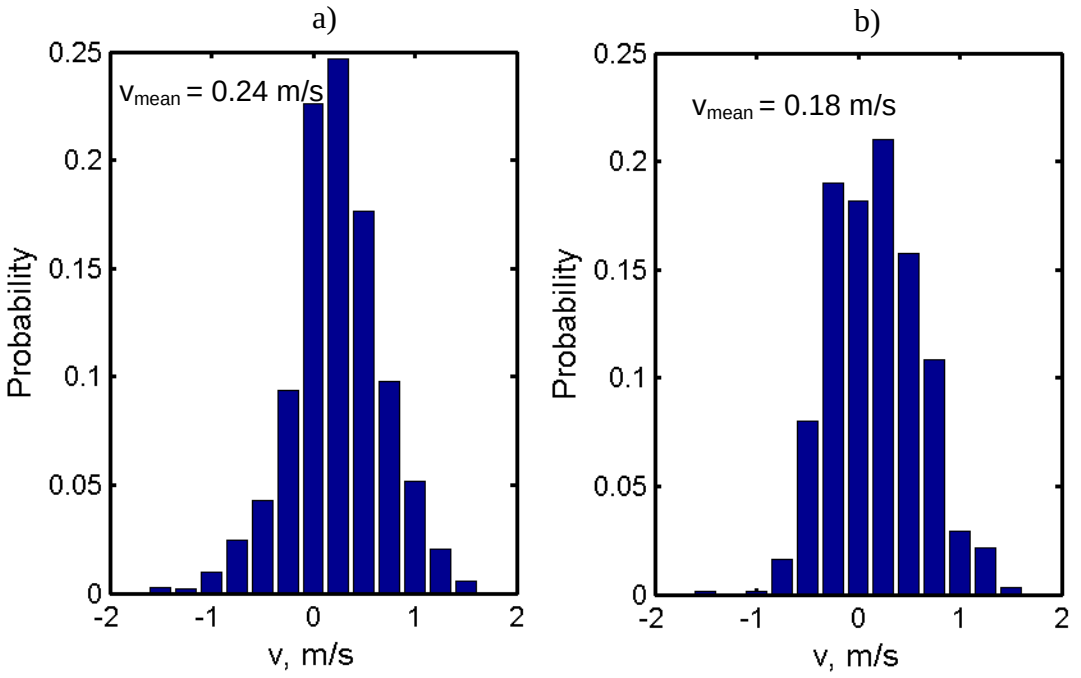

Figure 49. Wall-normal velocity distribution of detected coherent structures. a) Min-shear clockwise. b) Min-shear counter-clockwise.

more noticeably biased in the positive direction. While there are still structures moving away from the wall, the net motion is slightly positive, which may also help explain why this case performs best.

The qualitative and quantitative information gathered by the detection algorithm provides very useful insight into the nature of the coherent structures and can also be very powerful if applied identically to LES model results. By comparing these parameters, a modeler can more easily identify discrepancies between model and experimental results, or can conversely confirm agreement beyond first order statistics and show that the model is adequately capturing the behavior of the structures in every sense (location, size, strength, motion). Other features of the algorithm (which currently go beyond the scope of this work, but which have been implemented for future users) include the ability to filter the structure database by any desired input (size range, strength range, etc.) and recalculating the remaining parameters in virtue of the prescribed filter. this can help isolate the location of the strongest structures, or the strength of the largest structures, and gain deeper insight into the behavior of these structures. Exploring trends in this manner is suggested for future work

3.4 Flow thermal behavior

Observations of the temperature field beyond the wall provide insight into the energy transport from the hot mainstream towards the wall and complement the kinematic information to provide a fuller understanding of the overall mixing process. As discussed in Chapter 1, Wieghardt was one of the first researchers to propose that there is a universal scaling for the thermal flow profiles of a film cooling type flow.

Applying Wieghardt's method to the experimental data as seen in Figure 50, one can see that the method works well for most of the data, but fails very close to the injection, for $x/s < 15$. The fact that Wieghardt's correlation works reasonably well is quite reassuring, but, at the same time, it highlights the fact that many correlations in the open literature do not apply to the entire flowfield and the injection and near field must be treated carefully with respect to the open literature, particularly if one is to rely on available correlations for CFD inlet prescription or validation of near field results.

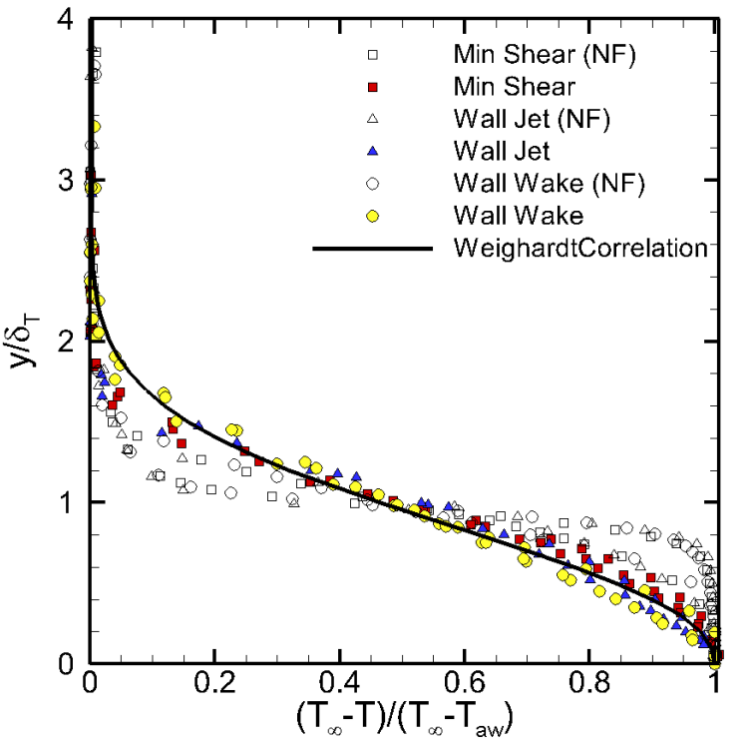

Figure 50. Wieghardt correlation for the thermal data in the current work. NF data (x/s < 15) is shown to deviate substantially from Wieghardt's correlation.

Figure 51 shows the temperature profiles for both adiabatic and non-adiabatic cases. Both show that the thermal transport closely follows the kinematic observations. The min-shear mixing layer is relatively thin and has no preferred

spreading direction. This keeps cool fluid near the wall and the film is able to persist for a considerable length. The wall-jet shows spread away from the wall, as observed by the initial bulging of the temperature profiles downstream of the inlet. This spread in turn induces hot fluid to be entrained at a larger rate than the min-shear, affecting the near-wall region which is seen to heat up faster than the min-shear.

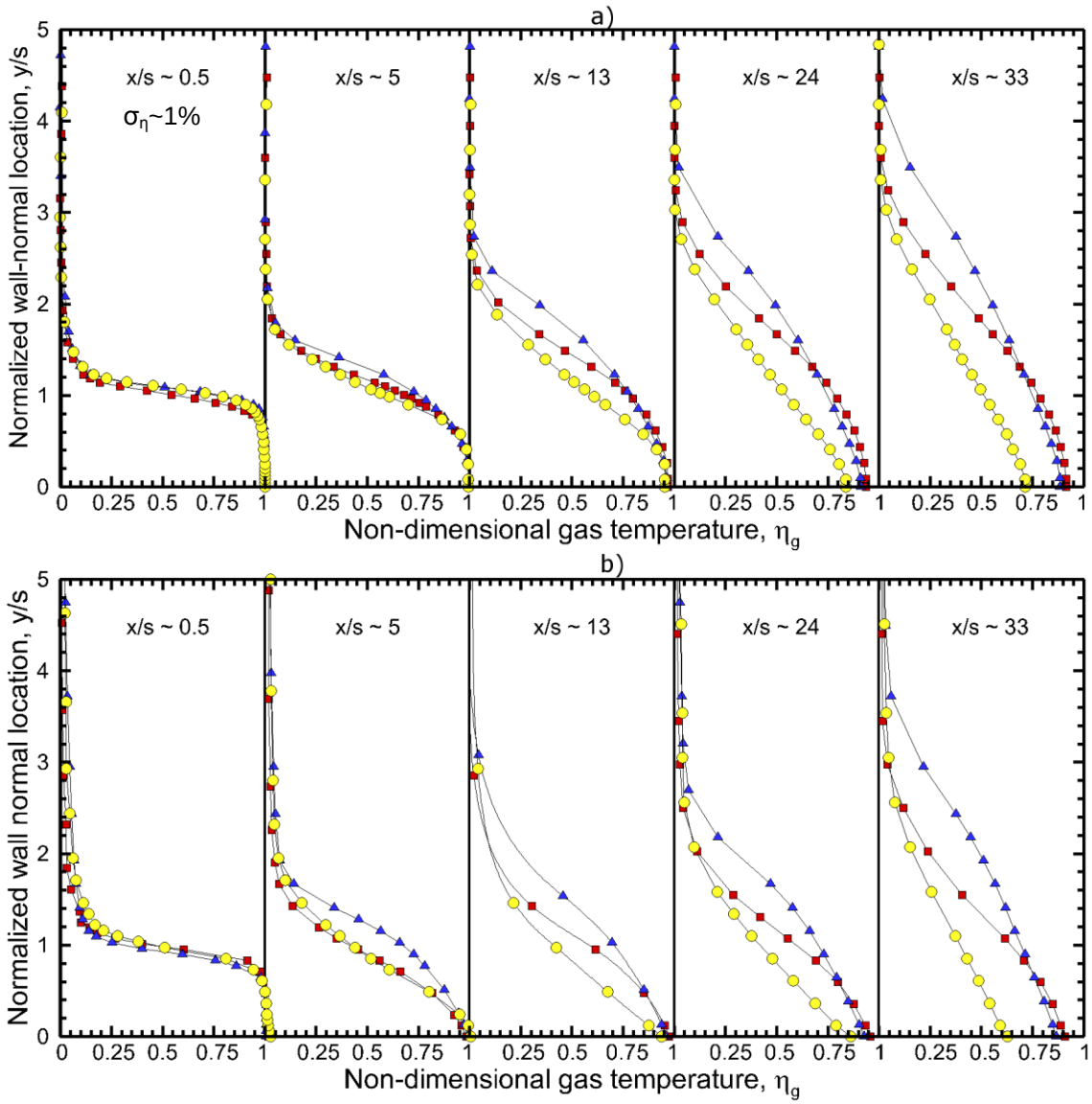

Figure 51. Non dimensional gas temperature profile evolution. a) adiabatic case, b) non-adiabatic case. wall-wake, min-shear, wall-jet

The wall-wake shows the opposite behavior. The mixing layer spreads towards the wall, as evidenced by the fact that at any y-location, the wall-wake exhibits the lowest value of η_g. Due to this spread direction, hot fluid is rapidly entrained, the film heats up faster than in any other case, decaying quickly and heating the wall up considerably. Non-adiabatic profiles show the same trends, but the near-wall gradients reflect the non-adiabatic condition such that at the wall $\partial\eta_g / \partial y < 0$. Observing the behavior of the fluid near the wall, it is evident that the boundary condition affects not only the wall temperature but also the fluid temperature. The profile shapes show that the fluid near the wall cools down in addition to the wall. This cooling effect on the gas in addition to the wall suggests that if the backside cooling is strong enough, it can remove heat from both the wall and fluid, effectively enhancing the film cooling performance. Figure 52 shows contours of the gas temperature, reconstructed from the adiabatic profiles in Figure 51. These 2-D contours allow one to more easily visualize the relative spread of the thermal mixing regions for each case. Lines corresponding to η_g = 0.1, 0.5, and 0.9 are included to aid in the visualization. The min-shear layer spreads relatively symmetric with respect to the louver height, as shown by the narrow spread and the slight upward motion of the mid-value line η_g = 0.5. The wall-jet is seen to spread away from the wall (and the mixing layer is thicker as shown by the distance between the 0.1 and 0.9 lines) while the wall-wake clearly spreads towards the wall (and its low performance is clearly seen as the η_g = 0.9 line impinges the wall much sooner than either of the other two shear scenarios .

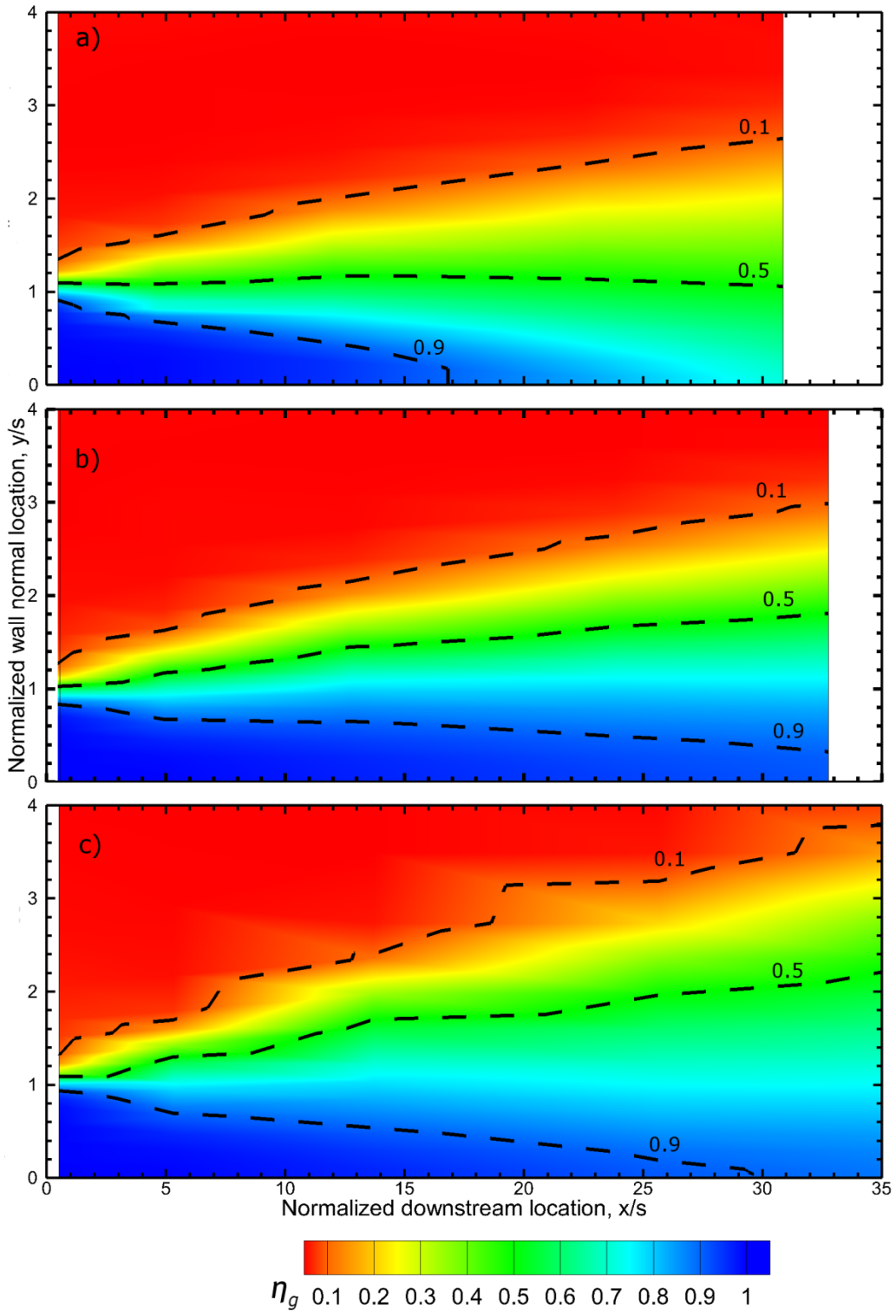

Figure 52. Contours of non-dimensional flow temperature (reconstructed from 2-D triangulation of profile data from Figure 51. a)Wall-wake, b) Min-shear, c)Wall-jet.

As it was explained in Chapter 2, while special care was taken to ensure that the relevant parameters influencing the compensation of the temperature signal corresponded to physical measurements, the relatively large uncertainty in the compensation technique (manifested by the calculation of the time constant and the somewhat arbitrary SNR choice) does not lend itself for a direct quantitative comparison to CFD results. Instead, qualitatively normalizing the RMS profiles of temperature by the maximum value for each profile provides a more useful interpretation on the results. This normalization allows one to readily identify the y-location of peak T_{RMS} for any given profile, and it has been shown in Chapter 2 that this normalization is less sensitive to the choice of time constant or SNR, as long as the choices are made with reasonable assumptions, as was the case in this work. Alternatively, modern CFD practices now rely on virtual thermocouples that can be inserted anywhere into the CFD domain. If the virtual probe is specified with parameters that are identical to those used to obtain the time constant for compensation, then CFD and experimental RMS results should be directly comparable.

Figure 53 shows the normalized T_{RMS} profiles for the adiabatic cases. At the inlet, one can readily see the similarities in all cases, particularly in the slot. This contrasts well with the kinematic turbulence intensities which were also shown to behave similarly for all cases. Further downstream, the differences among cases become evident. The y-location of peak RMS location for the min shear stays reasonably constant, hovering slightly above y/s=1.0, as expected. This suggests that the min-shear case does not exhibit a strong spread direction preference, and the

mixing is confined to a relatively small region at the louver height. However, the RMS distribution does widen with downstream location, consistent with the growth of the thermal mixing layer. The wall-jet and wall-wake cases exhibit opposing behaviors and are noticeably different from the min-shear case. The wall-jet RMS distribution widens as one moves downstream, and the y-location of peak RMS moves away from the wall. For the wall-wake, the opposite behavior is observed. while the distribution widens with downstream distance, the y-location of peak RMS moves towards the wall. As a result, the widening of the distribution is not as large as the wall-jet case. This behavior for all 3 cases qualitatively reflects that observed in the contours of Figure 52. More importantly, it also correlates well with the observation made from kinematic measurements, particularly those of the Reynold's shear stresses in Figure 40. Kinematic and thermal mixing, as determined by the general trends of peak *u'v'* and peak T_{RMS} follow very similar behavior.

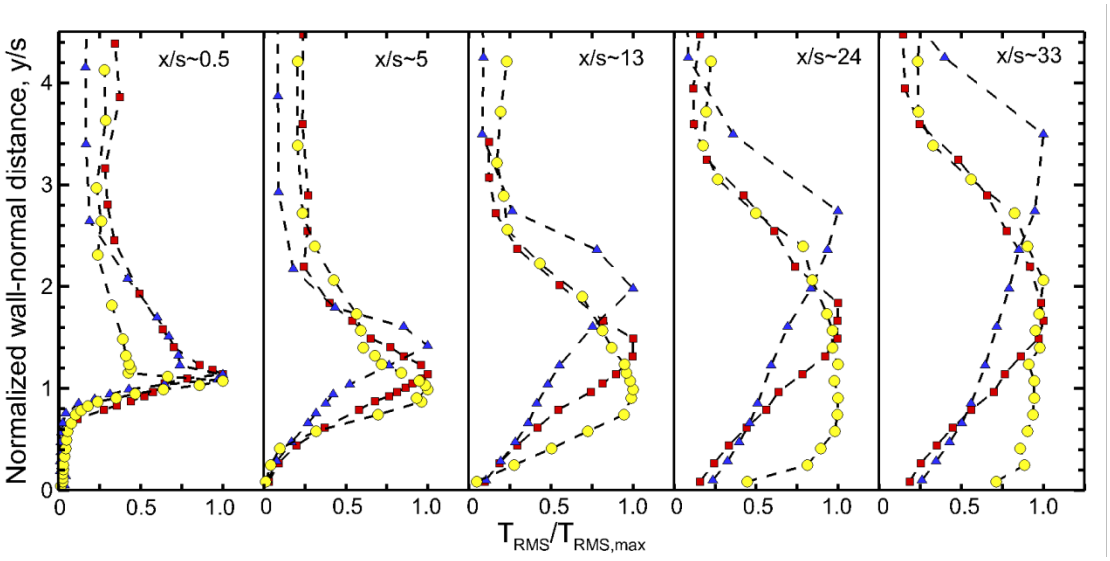

Figure 53. Normalized T_{RMS} profiles for the non-adiabatic flowfield (NA profiles exhibit similar behavior). wall-wake, min-shear, wall-jet

Overall, the minimum shear shows distinct behavior in all aspects of the flow and wall behavior. Defining bounds on what constitutes a true min-shear case may be useful in an engineering sense, but it remains challenging. Based on observations, the wall-jet case has a significantly different velocity ratio, yet its performance based on wall temperatures is not as strongly different from the min-shear case as the wall-wake. However, the remaining kinematic and thermal mixing data exhibit much more noticeable and stronger differences. Based on extrapolation of general behavior, it can be estimated that min-shear type behavior may be expected in the range $0.9<VR<1.1$. Outside of this range, both flowfield and wall effects should become more pronounced.

Chapter 4: Conclusions and Future Work

4.1 Summary of results

The detailed and comprehensive approach used in this work provides numerous insights about the film cooling flowfield. Inlet characterization revealed that scaling each stream by its reference velocity results in a universal profile shape regardless of shear scenario. This information is very useful for modelers as they can use this shape along with the relevant reference velocities in order to prescribe kinematic inlets. In terms of wall temperatures in both adiabatic and non-adiabatic cases, minimum shear cases perform better, as they undergo relatively weak mixing compared to other shear scenarios. This weak mixing was observed kinematically and thermally. Thermal mixing data reveals the preferred spread direction of the thermal mixing layer. Subsequently, this direction has a strong impact on observed wall temperatures. Kinematic data supports these observations and suggests that while convective velocities and shear strength in the shear cases are similar, the directionality of the initial mixing structures along with the preferred spread direction of the mixing layer has a significant impact on film cooling performance

Relatively little mixing occurs in the min-shear case as shown by the turbulent Reynolds shear stresses and T_{RMS}. In the other two cases, the wall jet spreads away from the wall, aiding the performance, while the wall-wake spreads towards the wall (as shown by the relatively larger magnitude Reynolds shear stresses near the wall) severely impacting the performance

For the remaining cases, the wall-wake exhibited stronger mixing near the wall compared to the wall jet (as seen in the behavior of Reynolds shear stresses and T_{RMS}), which helps explain why this case has the worst performance.

Coherent structures were successfully identified and characterized in all cases, and their overall behavior was shown to be consistent with other observations. In terms of near-wall behavior, kinematic data was shown to follow a log-linear behavior and the law of the wall seems to be valid for all scenarios under certain assumptions. This near-wall behavior should allow modelers to improve wall models specific to film cooling flows.

Compensation of micro-thermocouple data reveals that, despite a judicious approach to determine the time constant of the thermocouple, the nature of the signal coupled with an arbitrary choice of SNR may result in an incorrect value of TRMS. However, if the data is normalized by the peak value of TRMS, original thermocouple and compensated data seem to collapse, suggesting that quantitatively, this normalization resembles the true qualitative behavior of the RMS profiles, even if the actual values are incorrect.

4.2 Summary of contributions to the research community

This dissertation presents, to the best of our knowledge, the most comprehensive experimental dataset for slot film cooling in the open literature. The specific contributions of this work to the research community are:

- Established a unique experimental database for slot film cooling flows with the following characteristics:

- Canonical, realistic configuration (2-D slot injection, hot mainstream, cold film).
- Wide range of initial shear configurations, covering wall-wake, wall-jet and minimum shear type injection.
- Emphasis on the near injection region $x/s < 50$ where the initial mixing is established and ultimately determines the performance of the film.

- Developed a comprehensive approach for characterizing important film cooling transport processes
  - Kinematic measurements
  - Thermal mixing measurements
  - Surface temperature measurements and derived heat transfer
- Developed and implemented high fidelity measurement + analysis methods to characterize film cooling transport processes
  - Measurement Diagnostics
    - PIV
    - Microthermocouples
  - Characterization of Inlets
    - Kinematic scaling
    - Thermal scaling
  - Analysis of film cooling features
    - Adiabatic effectiveness
    - Scaling (kinematic and thermal flowfield)

- Coherent structure detection
- Mean and RMS fields
- Heat transfer

As a result of the current work, the research community can benefit in a number of ways. Experimentalists can apply the same diagnostics and analytical tools presented here to expand into alternative cooling scenarios (3-D, non-canonical). Modelers can use the database for development and validation, and several of the data analysis methods can also be implemented on numerical data to gain insight into the results (coherent structure detection, for example).

4.3 Future Work

The knowledge gained from this work and the proof-of-concept of the application of the experimental techniques developed and applied by this work allow for future film cooling research to benefit in several ways. There are several film cooling configurations that deviate from the canonical configuration studied in this work that can greatly benefit from a similar data set. One of the first configurations that comes to mind is a variable pressure gradient configuration. While keeping the 2-D slot configuration, a variable pressure gradient can be established, essentially accelerating or decelerating the freestream with downstream distance. This will impose different kinematics, which in turn will impact the mixing behavior. It is also expected that different shear conditions will respond differently to adverse and favorable pressure gradients. The relevance of exploring this behavior can provide special insight into film cooling in rocket nozzles as well as in turbine blade cascades.

Another interesting avenue worth exploring is modifying the canonical 2-D configuration to 3-D. This can be done in several ways. By inserting ribs in the 2-D slot, one can investigate the 3-D effects that closely resemble the behavior of a turbine blade's trailing edge. Alternatively, one could entirely change the slot injection setup for that of rows of holes. Hole film cooling is a very active area of research, with applications focused on turbine blade surfaces. In either case, the 3-D nature of the flow may require the augmentation of the diagnostics to stereoscopic or tomographic PIV, and transversal thermocouple measurement locations (thermocouple rakes).

While the current body of research covers shear injection scenarios applicable to both air breathing and rocket engines, the subsonic nature of the experiments imposes a limitation on direct comparison to rocket engine scenarios. While a validated compressible subsonic CFD model can be relatively easily extended to supersonic, it would be useful to validate the results of such a model with supersonic experiments. As such, a similar approach to that of the current work can be applied to supersonic experiments. The direct extension of the experimental techniques to supersonic flows is challenging, but there are several techniques that allow for global velocity measurements, including PIV. Thermal mixing could be simulated by passive scalar mixing, which is easier to measure with non-intrusive techniques. Wall temperatures can also be measured by embedded thermocouples or IR thermography.

With respect to the diagnostics and data reduction techniques presented in this work, it would be very interesting to apply the coherent structure detection algorithm to LES model results and compare to the results from this work. The coherent

structure detection algorithm should be another comparison tool, as it provides specific insight into how well the model is capturing the turbulent eddies in the flowfield and can serve as a diagnostic/debugging tool if the mean and RMS results do not match well.

Finally, newer diagnostic tools have recently evolved from the same tools used in this work. Their application to film cooling flows can be done with relative ease while providing extra data. Time-resolved PIV can be applied to temporally resolve the flowfield, allowing for an easier visualization of coherent structures as they evolve in time. Time-resolved data can also open the door for power spectral density measurements of the global kinematic field, as these systems operate in the kHz range. If 3-D flows are to be measured, then dual-plane PIV (not to be confused with stereoscopic PIV) can be used to measure the 3 velocity components as well as the 9 components of the velocity gradient tensor. Simultaneous PIV-thermometry using temperature sensitive phosphorescent particles is yet another diagnostic tool that can be applied to similar flows to obtain data of great use for modelers which is currently unavailable. By simultaneously obtaining velocity and temperature data, the fluctuating term from the energy equation (v'T') can be obtained. Knowledge of this term experimentally can be of great value to modelers.

Bibliography

1. Cruz, Carlos. “Experimental and Numerical Characterization of Turbulent Slot Film Cooling,” Ph.D. Dissertation, University of Maryland, College Park, 2008
2. Wieghardt, K. “Hot Air Discharge for De-Icing,” Air Material Command, AAF Trans. No. F-TS-919 RE, Dec. 1946
3. Tribus, M., Klein, J., “Forced Convection from Non-Isothermal Surfaces,” Heat Transfer, a Symposium, University of Michigan, Ann Arbor, 1953.
4. Papell, S., Trout, A. “Experimental Investigation of Air Film Cooling Applied to an Adiabatic Wall by Means of an Axially Discharged Slot,” NASA Technical Note D-9, August 1959
5. Hatch, J.E., Papell, S., “Use of a Theoretical Flow Model to Correlate Data for Film Cooling or Heating an Adiabatic Wall by Tangential Injection of Gases of Different Fluid Properties,” NASA Technical Note D-130, November 1959
6. Papell, S., “Effect on Gaseous Film Cooling of Coolant Injection Through Angled Slots and Non-trivial Holes,” NASA Technical Note D-299, September 1960
7. Hartnett, J.P., Birkebak, R.C., Eckert, E.R.G, “Velocity Distributions, Temperature Distributions, Effectiveness and Heat Transfer for Air Injected Through a Tangential Slot Into a Turbulent Boundary Layer,” Journal of Heat Transfer, pp. 293-306, August 1961
8. Seban, R.A., Back, L.H., “Velocity and Temperature Profiles in a Wall Jet,” Int. J. Heat Mass Transfer, Vol. 3, pp. 255-265, 1961
9. Stollery, J.L, El-Ehwany, A.A.M, “A Note on the Use of a Boundary-Layer Model for Correlating Film-Cooling Data,” Int. J. Heat Mass Transfer, Vol. 8, pp. 55-65, 1965
10. Stollery, J. L., El-Ehwany, A. A. M., "Shorter Communication on the Use of a Boundary-Layer Model for Correlating Film Cooling Data," I Int. J. Heat Mass Transfer,Vol. 10, No. 1, pp. 101-105, 1967
11. Goldstein, R.J., “Fim Cooling,” Advances in Heat Transfer, Vol. 7, Academic Press, New York, pp. 321-378, 1971
12. Ballal, D.R., Lefebvre, A.H., “Film-Cooling Effectiveness in the Near-Slot Region,” Journal of Heat Transfer, pp. 265-266, May 1973
13. Simon, F.F, “Jet Model for Film Cooling With Effect of Free-Stream and Coolant Turbulence,” NASA Technical Paper 2655, October 1986
14. Marek, C.J., Tacina, R.R., “Effect of Free Stream Turbulence on Film Cooling,” NASA Technical Note D-7958, 1975
15. Abramovich, G.N., “The Theory of Turbulent Jets,” MIT Press, 1963
16. Cruz,C.A., Marshall, A.W., “Surface and Gas Measurements Along a Film-Cooled Wall,” Journal of Thermophysics and Heat Transfer, Vol. 21, No. 1, January-March 2007
17. Bons, J.P, MacArthur, C.D., Rivir, R.B., “The Effect of High Freestream Turbulence on Film Cooling Effectiveness,” Int. Gas Turbine and Aeroengine Technology Report, 1994
18. Kacker, S.C., Whitelaw, J.H., “Some Properties of the Two-dimensional

Turbulent Wall Jet in a Moving Stream," Journal of Applied Mechanics, pp .641, December 1968
19. Kacker, S.C., Whitelaw, J.H., "The Effect of Slot Height and Slot-Turbulence Intensity on the Effectiveness of the Uniform Density, Two-Dimensional Wall Jet," Journal of Heat Transfer, pp .469, November 1968
20. Kacker, S.C., Whitelaw, J.H., "Prediction of Wall-Jet and Wall-Wake Flows," Journal of Mechanical Engineering Science, Vol. 12, No. 6, 1970
21. Kacker, S.C., Whitelaw, J.H., "The Turbulence Characteristics of Two-dimensional Wall-Jet and Wall-Wake Flows," Journal of Applied Mechanics, pp. 239, March 1971
22. Raffel, M., Willert, C., and Kompenhans, J., "Particle Image Velocimetry," 1st edition, Springer-Verlag, 1998
23. Gogineni, S.P., Pestian, D.J., Rivir, R.B., Goss, L.P., "PIV Measurements of Flat Plate Film Cooling Flows With High Free Stream Turbulence," AIAA 34th Aerospace Sciences Meeting and Exhibit, AIAA Paper 96-0617, January 1996
24. Sousa, J.M.M, Freek, C., Pereira, J.C.F., Merzkirch, W., "Visualization Study of Near-Wall Flow Using a DIC-PIV System," 8th International Symposium on Flow Visualization, 1998
25. Spalart, P.R., "Direct Simulation of a Turbulent Boundary Layer up to Re_θ = 1410," Journal of Fluid Mechanics, Vol. 187, pp. 61-98, 1988
26. Fukushima, C., Aane, L., Westerweel, J., "Investigation of the Mixing Process in an Axisymmetric Turbulent Jet Using PIV and LIF, 10th International Symposium on Application of Laser Techniques to Fluid Mechanics, July 1999
27. Peterson, S., "Structural Features of Jets-In-Crossflow for Film-Cooling Applications," 41st Aerospace Sciences Meeting and Exhibit, AIAA Paper 2003-303, January 2003
28. Polanka, M.C., Cutbirth, J.M., Bogard, J.D., "Three Component Velocity Field Measurements in the Stagnation Region of a Film Cooled Turbine Vane," Journal of Turbomachinery, Vol. 124, pp.445-452, July 2002
29. Chen,Y.,Eaton,J, "High Resolution PIV Measurements Around a Model Turbine Blade Trailing Edge Film-cooling Breakout," Experiments in Fluids, pp. 199, 2008
30. Kaehler, C.J., "The Significance of Coherent Flow Structures for the Turbulent Mixing in Wall-Bounded Flows," Dissertation zur Erlangung des Doktorgrades der Mathematisch-Naturwissenschaftlichen Fakultaten der Georg-August-Universitat zu Gottingen, 2004
31. Marshall, A., "Effects of Jet Momentum Distribution on Combustion Characteristics in Co-swirling Flames," Ph.D. Dissertation, University of Maryland, College Park, 1996
32. Kunnugi, M. and Jinno, H., "Measurements of Fluctuating Temperature," Seventh Symposium (International) on Combustion, Butterworths, pp.942-47, 1959.
33. Jansson, L.S., Davidson,L., Olsson, E., "Calculation of Steady and Unsteady Flows in a Film-Cooling Arrangement Using a Two-Layer Algebraic Stress

Model," Numerical Heat Transfer, pp. 237-258, 1994
34. Dellimore, K., "Modeling and Simulation of Mixing Layer Flows for Rocket Engine Film Cooling," Ph.D. dissertation, University of Maryland, College Park, 2010
35. Voegele, A., "Numerical Characterization and Modeling of Adiabatic Slot Film Cooling," M.S. Thesis, University of Maryland College Park, 2011
36. Raffan,F., Marshall, A.W., "Characterization of Slot Film Cooling Performance Using Minimally Intrusive Diagnostics," in preparation for submission to Experiments in Fluids
37. Raffan, F., "Experimental Characterization of Slot Film Cooling Flows With Minimally Intrusive Diagnostics," M.S Thesis, University of Maryland, College Park, 2008
38. Hill, P., Peterson, C., "Mechanics and Thermodynamics of Propulsion," 2nd edition, Prentice Hall, 1991
39. Samimy, M., Lele, S. K., "Motion of Particles with Inertia in a Compressible Free-shear Layer," Physics of Fluids A, Vol. 3, August 1991
40. Scarano, F., "Overview of PIV in Supersonic Flows," in Particle Image Velocimetry, Schröder, A., and Willert, C. Eds., Springer, 2008.
41. Pope, S., "Turbulent Flows," Cambridge University Press, 1st edition, 2000
42. Westerweel, J., "Fundamentals of Digital Particle Velocimetry," Measurement Science Technology, Vol. 8, 1997
43. Westerweel, J., Dabiri, D., Gharib,M., "The Effect of a Discrete Window Offset on the Accuracy of Cross-correlation Analysis of Digital PIV Recordings," Experiments in Fluids **23** , 1997
44. FlowMaster Software Product Manual for Davis 7.2, LaVision Gmbh, Göttingen, Germany, 2006.
45. Adrian, R.J., "Particle Imaging Techniques for Experimental Fluid Mechanics,"Annual Review in Fluid Mechanics, 1991
46. Adrian, R.J., Christensen, K.T., Liu, Z., "Analysis and Interpretation of Instantaneous Turbulent Fields," Experiments in Fluids 29, September 2000
47. Kays, W., Crawford, M., "Convective Heat and Mass Transfer," McGraw Hill, 4th edition, 2004
48. Wallace, J., Bernard, P., "Turbulent Flow: Analysis, Measurement and Prediction," Wiley, 1st edition, 2002
49. Bradshaw, P., "Introduction to Turbulence and its Measurement," Pergamon Press, 1st edition, 1971
50. Chong, M.S., Perry, A.E. and Cantwell,B.J., "A General Classification of Three-dimensional Flow Fields," Physics of Fluids A 2, 1990.
51. Jeong, J. and Hussain, F., "On the Identification of a Vortex," Journal of Fluid Mechanics 285, 1995.
52. Chakraborty, P., Balachandar, S., Adrian, R.J., "On the Relationships Between Local Vortex Identification Schemes," Journal of Fluid Mechanics 535, 2005.
53. Hunt, J. C. R.,Wray, A. A., and Moin, P., "Eddies, Stream, and Convergence Zones in Turbulent Flows," Center for Turbulent Research Report CTR-S88, 1998

54. Burgers, J. M., "A Mathematical Model Illustrating the Theory of Turbulence," Advances in Applied Mechanics 1, 1958.
55. Acheson, D. J., "Elementary Fluid Dynamics," Oxford University Press, 1990.
56. Graftieaux, L., Michard, M., and Grosjean, N., "Combining PIV, POD and Vortex Identification Algorithms for the Study of Unsteady Turbulent Swirling Flows," Measurement Science and Technology 12, 2001.
57. Lind, A. H., and Jones, A. R., "Vortex Shedding From Airfoils In Reverse Flow," AIAA Journal, Vol. 53, No. 9, 2015.
58. von Kármán, T., "Mechanische Ähnlichkeit und Turbulenz," Nachrichten von der Gesellschaft der Wissenschaften zu Göttingen, Fachgruppe 1 (Mathematik) 5: 58–76 (also as: "Mechanical Similitude and Turbulence", Tech. Mem. NACA, no. 611, 1931).).
59. Clauser, F.H., "The Turbulent Boundary Layer," Adv. Appl. Mech. 4:1–51, 1956
60. Le, H., Moin, P., Kim, J., "Direct Numerical Simulation of Turbulent Flow over a Backward Facing Step," Journal of Fluid Mechanics, 1997
61. Kim, J., Kline, S. J., Johnston, J. P., "Investigation of a Reattaching Turbulent Shear Layer: Flow Over a Backward Facing Step," Journal of Fluids Engineering, 1980.
62. Armaly, B.F., et.al.,"Experimental and Theoretical Investigation of Backward-facing step Flow," Journal of Fluid Mechanics, Vol. 187, 1983
63. Blevins, L. Pitts, W. "Modeling of Bare and Aspirated Thermocouples in Compartment Fires" NISTIR 6310 Report. NIST. United States Department of Commerce Technology Administration. 1999.
64. Shaddix, C. "Practical Aspects of Correcting Thermocouple Measurements for Radiation Loss" Western State Section/The Combustion Institute. WSS/CI 98F-14. 1998.
65. Mishra, D.P., "Experimental Combustion: An Introduction," CRC Press, 2014.
66. Lipták, B.G., "Instrument Engineers' Handbook: Process control and optimization," 4th ed., CRC Press. p. 100, 2003.
67. Terzis, A., et al., "Thermocouple Thermal Inertia Effects on Impigement Heat Transfer Using the Transient Liquid Crystal Technique," Meas. Sci. and Tech., Vol. 23, No.11, 2012
68. http://www.matweb.com
69. Ghodoussi, R., "An Investigation on Thermal Characteristics of Premixed Counterflow Flames Using Micro-thermocouples," M.S. Thesis, Department of Fire Protection Engineering, University of Maryland, College Park, 2005
70. Marshall, A., "Effects of Jet Momentum Distribution on Combustion Characteristics in Co-swirling Flames," Ph.D. Dissertation, Department of Mechanical Engineering, University of Maryland, College Park, 1996
71. Incropera, F., DeWitt, D., "Fundamentals of Heat and Mass Transfer," 5th ed., Wiley, 2001
72. McAdams, W. H., "Heat Transmission," McGraw-Hill, 1942.
73. Carbon, M.W., Kutsch, H. J., and Hawkins, G.A., "The Response of Thermocouples to Rapid Gas-temperature Changes," Annual meeting of the

ASME Heat Transfer Division, New York, November 1949.
74. Kay, S.' "Intuitive Probability and Random Processes using MATLAB," Springer, 2005
75. Batchelor, G.K., "An Introduction to Fluid Dynamics," Cambridge University Press, 1967
76. White, F., "Viscous Fluid Flow," 3rd. ed., McGraw-Hill, 2005
77. http://www.solvayplastics.com/sites/solvayplastics/EN/Solvay%20Plastics%20Literature/DPG_Udel_Design_Guide_EN.pdf
78. http://www.technicalglass.com/enlarged_technical/lg_transmittance_graph.html
79. Howell, J.R., "A Catalog of Radiation Heat Transfer Configuration Factors," 3rd ed., http://www.engr.uky.edu/rtl/Catalog/
80. Siegel, R., Howell, J.R., "Thermal Radiation Heat Transfer," 4th ed., Taylor and Francis, 2002
81. Bevington, P.R., "Data Reduction and Error Analysis for the Physical Sciences," New York: McGraw-Hill, pp. 58-64, 1969.
82. Czichos, H., Saiato, T., Smith, L., "Springer Handbook of Materials and Measurement Methods," 6th ed., Springer, 2006
83. Launder, B.E., Rodi, W., "The Turbulent Wall Jet, Measurements and Modelling," Ann. Review Fluid Mechanics, 1983
84. Campbell, J.F., "Turbulent Wall Jet in a Coflowing Stream," NASA TN D-8025, 1975
85. Ahlman, D., et al., "Direct Numerical Simulation of Nonisothermal Turbulent Wall Jets," Physics of Fluids, Vol. 21, 2009